Master's Thesis

High-energy density supercapacitors with three-dimensional (3D) current collectors

Kyeong Nam Kang

School of Chemical Engineering

Graduate School of UNIST

2017

High-energy density supercapacitors with three-dimensional (3D) current collectors

Kyeong Nam Kang

School of Chemical Engineering

Graduate School of UNIST

High-energy density supercapacitors with three-dimensional (3D) current collectors

A thesis/dissertation

Submitted to the Graduate School of UNIST

In partial fulfillment of the

Requirements for the degree of

Master of Engineering

Kyeong Nam Kang

12. 15. 2017

Approved by

_____

Advisor

Ji-Hyun Jang

High-energy density supercapacitors with three-dimensional (3D) current collectors

Kyeong Nam Kang

This certifies that the thesis/dissertation of Kyeong Nam Kang is approved.

12. 15. 2017

Signature

_____

Advisor: Ji-Hyun Jang

Signature

_____

SungHoon Park

Signature

_____

Ji wook Jang

Contents

Publication list

List of Figures

and Cu, and an amorphous region of the carbon layer. The image shows the configuration of the Cu, C, and $Ni(OH)_2$ layer from inward to outward.

Figure 2. 6. Comparison of SEM images of the 3D-Cu electrode (a-c) and 3D-C/Cu electrode (d-f) at various magnifications.

Figure 2. 7. SEM cross section image of the as-synthesized 3D-$Ni(OH)_2$/C/Cu.

Figure 2. 8. The BET data of the 3D-C/Cu and 3D-$Ni(OH)_2$/C/Cu electrode. In the table, comparisons of specific surface area, pore volume and mean pore size are shown in detail.

Figure 2. 9. Comparison of XRD patterns of 3D-Cu, 3D-C/Cu, and 3D-$Ni(OH)_2$/C/Cu to determine whether the 3D-Cu structure is oxidized or not (left). Enlarged XRD patterns of the 3D-$Ni(OH)_2$/C/Cu to confirm Ni(OH)2 exactly.

Figure 2. 10. Total EDS elemental mapping images of the as-prepared 3D-$Ni(OH)_2$/C/Cu electrode. And the detail peaks for (a) C, (b) O, (c) Ni and (d) Cu. The table of ratios of all elements, respectively.

Figure 2. 11. XPS spectra of (a)C 1s, (b) Cu 2p, (c) Ni 2p, and (d) O 1s for the 3D-$Ni(OH)_2$/C/Cu electrode.

Figure 2. 12. A schematic of the electron transfer mechanism of the $Ni(OH)_2$ active materials deposited (a) on a typical Ni plate current collector and (b) on the 3D-C/Cu/Ni plate.

Figure 2. 13. Electrochemical characterization of the 3D-$Ni(OH)_2$/C/Cu electrode in a three-electrode system. (a) CV curves at various scan rates in 1 M KOH. (b) Discharge curves during galvanostatic charge/discharge measurement. (c) Specific capacitance of 3D-$Ni(OH)_2$/C and 3D-$Ni(OH)_2$/C/Cu as a function of the current density based on the galvanostatic charge/discharge measurement (d) Cycle performance of the 3D-Ni(OH)2/Cu and 3D-$Ni(OH)_2$/C/Cu electrode at a current density (specific capacitance) of 200 A/g.

Figure 2. 14. Three-electrode electrochemical measurements of the 3D-$Ni(OH)_2$/C/Cu composite in a 1M KOH aqueous solution with various amounts of $Ni(OH)_2$. (a) CV curves for different amounts of $Ni(OH)_2$ deposited at 20mV/s. (b) Galvanostatic charge/discharge curves at 1A/g, (c) Specific capacitance as a function of the current density. (d) Cycling performance at 200A/g.

Figure 2. 15. Comparison of CV curves between 3D-C/Cu (Current collector) and 3D-$Ni(OH)_2$/C/Cu electrode.

Figure 2. 16. Three-electrode electrochemical measurements of the 3D-$Ni(OH)_2$/Cu composite in a 1 M KOH aqueous solution. (a) CV curves at various scan rates, (b) discharge curves during galvanostatic

charge/discharge measurement.

Figure 2. 17. Electrochemical characterization of the 3D-$Ni(OH)_2$/C/Cu electrode in a three-electrode system. (e) SEM image of the 3D-$Ni(OH)_2$/C/Cu before and after 10,000 cycles. (f) Electrochemical Impedance Spectroscopy (EIS) of the 3D-$Ni(OH)_2$/Cu and 3D-$Ni(OH)_2$/C/Cu electrodes.

Figure 2. 18. SEM images of (a-c) show the 3D-$Ni(OH)_2$/C/Cu structure after 10000 cycles.

Figure 2. 19. Three-electrode electrochemical performance of the 3D-$Ni(OH)_2$/C/Cu composite in 1M KOH aqueous solution, for measuring areal capacitance. (a) CV curves of the electrode at different scan rates. (b) Discharge curves of the electrode at different current densities per area. (c) Gravimetric areal capacitance as a function of the current densities, and (d) cycling performance at 20A/g for 10000cycles.

Figure 2. 20. Comparison of XRD patterns of the 3D-$Ni(OH)_2$/C/Cu before and after 10,000 cycles.

Figure. 2. 21. XPS spectra of (a)C 1s, (b) Cu 2p, (c) Ni 2p, and (d) O 1s for the 3D-$Ni(OH)_2$/C/Cu electrode after 10,000 cycles.

Figure 2. 22. Zoom-up range (a) and gauge span (b) of EIS of the as-prepared electrode (blue) and other references : $Ni(OH)_2$ on nickel film, and $Ni(OH)_2$ on nickel foam.

Figure 2. 23. Model and values of Electrochemical Impedance Spectroscopy (EIS) of the 3D-$Ni(OH)_2$/Cu and 3D-$Ni(OH)_2$/C/Cu electrodes.

Figure 2. 24. (a) Comparative CV curves of the 3D-Mn_3O_4/C/Cu and 3D-$Ni(OH)_2$/C/Cu at 50 mV/s. (b) CV curves of the 3D-$Ni(OH)_2$/C/Cu//3D-Mn_3O_4/C/Cu asymmetric supercapacitor measured at different potential windows, at 100 mV/s. (c) CV curves of the 3D-$Ni(OH)_2$/C/Cu//3D-Mn_3O_4/C/Cu asymmetric supercapacitor measured at different scan rates of 10, 20, 50, 100 mV/s between 0 and 1.6V in 1 M KOH aqueous electrolyte. (d) Galvanostatic charge/discharge curves of the 3D-$Ni(OH)_2$/C/Cu//3D-Mn_3O_4/C/Cu asymmetric supercapacitor as a function of different current densities. (e) Ragone plot of 3D-$Ni(OH)_2$/C/Cu with other references and (f) Specific capacitance retention of 3D-$Ni(OH)_2$/C/Cu//3D-Mn_3O_4/C/Cu asymmetric supercapacitor as a function of cycle.

Figure 2. 25. XRD patterns of 3D-Mn_3O_4/C/Cu. The inset shows enlarged XRD patterns of 3D-Mn_3O_4/C/Cu.

Figure 2. 26. Schematic illustration of the assembled 3D-$Ni(OH)_2$/C/Cu//3D-Mn_3O_4/C/Cu devices.

Figure 2. 27. (a) CV curves of the 3D-$Ni(OH)_2$/C/Cu//Activated carbon asymmetric supercapacitor measured at different scan rates of 10, 20, 30, 40, and 50 mV/s between 0 and 1.6V in 1M KOH aqueous electrolyte, (b) Galvanostatic charge/discharge curves of the 3D-$Ni(OH)_2$/C/Cu //Activated carbon

asymmetric supercapacitor as a function of different current densities, (c) Ragone plot of the 3D-$Ni(OH)_2$/C/Cu with other references and (d) specific capacitance retention of the 3D-$Ni(OH)_2$/C/Cu //Activated carbon asymmetric supercapacitor as a function of cycle.

Figure 3. 1. (a) Schematic representation of the fabrication of the 3D-NiCo LDH/Ni electrode and (b-g) FE-SEM images of 3D-NiCo LDH/Ni nanostructures at different magnifications.

Figure 3. 2. (a-d) Cross-sectional images of 3D-NiCo LDH/Ni nanostructures. EDS spectrum (e) and elemental mappings (f-h) of 3D-NiCo LDH/Ni nanostructures.

Figure 3. 3. (a) XRD patterns and (b) Raman spectra of 3D-NiCo LDH/Ni nanostructures. XPS spectra of 3D-NiCo LDH/Ni nanostructures (c) survey, (d) Ni 2p, (e) Co 2p and (f) O 1s.

Figure 3. 4. (a and b) Cyclic voltammetry and charge/discharge profiles of Ni, 3D-Ni, and 3D-NiCo LDH/Ni nanostructures.

Figure 3. 5. (a) Cyclic voltammetry profiles and (b and c) specific capacitance of 3D-NiCo LDH/Ni nanostructures at various scan rates. (d) Galvanostatic charge/discharge profiles and (e and f) specific capacitance of 3D-NiCo LDH/Ni nanostructures at different currents.

Figure 3. 6. Cyclic stability of 3D-NiCo LDH/Ni nanostructures obtained at a current of 15mA; the inset shows the charge/discharge curves.

Figure 3. 7. Nyquist plots of 3D-NiCo LDH/Ni nanostructures electrode before and after the 10,000 cycle test.

Figure 3. 8. (a-b) FE-SEM images of 3D-NiCo LDH/Ni electrode after the 10,000 cycles test.

Figure 3. 9. Schematic representation of the fabrication of 3D-NiCo LDH/Ni//3D-Mn_3O_4/Ni asymmetric supercapacitor.

Figure 3. 10. XRD patterns of 3D-Mn_3O_4/Ni. The inset shows enlarged XRD patterns of 3D-Mn_3O_4/Ni.

Figure 3. 11. Cyclic voltammetry profiles, galvanostatic charge/discharge profiles and specific capacitance of 3D-Mn_3O_4/Ni nanostructures.

Figure 3. 12. (a) CV curves of the asymmetric supercapacitor at different scan rates. (b) Galvanostatic charge-discharge curves and (c) specific capacitance of the asymmetric supercapacitor at different current densities.

Figure 3. 13. Ragone plots of our supercapacitor based on a full cell, compared with other electrodes using NiCo-LDH.

Figure 3. 14. Table of energy density and power density as a function of current density.

Figure 3. 15. (a) Cycling performance of the asymmetric supercapacitor for 10,000 cycles, and (b)

Abstract

Supercapacitors have attracted tremendous attention over past decades due to their high power density, long cycle life, and fast charging/discharging rate within seconds. In this device, metal oxides/hydroxides are commonly used as the active materials. Although metal oxides/hydroxides provide their high theoretical capacitances and the capability of relatively good reversible redox reactions, they have several fatal drawbacks caused by the poor conductivity of metal oxide materials impeding their practical use: long delay in the charge transportation rate and thus long charge time, poor capacitance at high scan rates, and poor long-term stability. Furthermore, high energy and power densities are importantly needed for supercapacitors to apply practical usages. Taking these into account, I introduce several approaches with the two concepts roughly to improve electrochemical properties of the supercapacitors; 1) fabrication of the three dimensional structure of active materials and current collector with forming the 3D-conducting network and 2) fabrications of the asymmetric supercapacitor devices with metal oxide which have 3~5 times higher capacitance than carbon-based electric double layer capacitance (EDLC) in the negative electrodes.

First, I improved the capacitor properties of the active materials by forming the carbon coated three-dimensional porous copper structure (3D-C/Cu) onto the current collector. It is suggested as an additive and binder-free conductive electrode with short electron path distances, large electrochemical active sites, and improved structure stability. The 3D-porous copper structure (3D-Cu) provides high electrical conductivity and facilitates electron transport between the $Ni(OH)_2$ active materials and the current collector of the Ni-film. A carbon coating was applied to the 3D-Cu to prevent the oxidation of Cu, without degrading the electron transport behavior of the 3D-Cu. The 3D-$Ni(OH)_2$/C/Cu exhibited a high specific capacitance of 1860 F/g at 1A/g, and good cycling performance, with an 86.5 % capacitance retention after 10,000 cycles. Furthermore, the 3D-Mn_3O_4/C/Cu electrode as a negative electrode displayed excellent electric double-layer capacitance and pseudocapacitance property. When tested in a two-electrode system, an asymmetric supercapacitor exhibited an energy density of 147.9 Wh/kg and a power density of 37.0 kW/kg.

Second, I demonstrate a fabrication of flexible wire-type hybrid supercapacitor (with a smart “wire band-type” function for the smart watch & smart google glass) using three dimensional (3D)-NiCo LDH/Ni nanostructures as the positive electrode, 3D-Mn_3O_4@Ni wire as the negative electrode, and PVA-KOH gel electrolyte as the separator. The 3D-Ni wire is free to bend, and act as a binder and conductive additive-free current collector as well as provides an additional faradaic energy storage. The as-prepared 3D-Ni wire electrode holds abundant porous dendritic walls structure formed by several nanoparticles for easy access of electrolyte ions and highly conductive networks for fast electron

transfer, and provides numerous electroactive sites for improved charge storage. Thus, as-fabricated hybrid supercapacitors based on 3D-NiCo-LDH@Ni//3D-Mn_3O_4@Ni wire delivered excellent electrochemical capacitive properties, maintained the inherent characteristics of flexibility with outstanding electrochemical performance reliability while bending. The maximum energy density of the asymmetric supercapacitor can be further calculated to be 153.3 Wh/kg at the power density of 2238 W/kg based on total mass of active materials. Further, the feasibility of as-fabricated hybrid device was tested in real time conditions by driving the green LED and wearable watch. These results create such wire band-like hybrid supercapacitors a great potential for smart wearable devices including smart watches, google glasses, and implantable devices having energy delivering capacity and flexibility

Chapter 1. Introduction of Supercapacitors with 3D-current collector

1.1 Overview

With growing demand on energy sources, diminishing natural resources, increasing environment issues, the development of safe, no-pollution, low-cost and renewable energy systems where combustion no longer dominates has become a grand challenge nowadays. Although renewable and sustainable electricity generation sources such as solar, wind, and wave could be candidates for conventional energy fuels, it is still important to find desirable electrical energy conversion and storage systems possessing high efficiency to save extra energy hence to meet the increased energy demands as shown in **Figure 1.1**. Consequently, the search for the next generation of energy-storage materials and devices such as supercapacitors and rechargeable batteries with pollution free operation, high efficiency, and a long cycling life is extremely important.

Supercapacitors can be classified into two types based on their charge-storage mechanism, ion adsorption (electrical double-layer capacitors) governed by electrostatic charge diffusion and accumulation at the interface of the electrode/electrolyte and fast surface redox reactions (pseudocapacitors) affected by Faradaic reactions at the electrode materials. Early studies of supercapacitors mainly focus on electrical double-layer capacitors (EDLCs) based on carbonaceous materials, which suffer from relatively low specific capacitance (<300F/g) and instability at high charge-discharge rates. In order to improve specific capacitance, lots of research has been dedicated to investigating pseudocapacitive materials such as transition metal oxides such as RuO2 and Co3O4, transition metal hydroxides, especially Ni(OH)2 and Co(OH)2, and conducting redox polymers.

Lithium ion battery has been mainly used in the world because it has high energy density. However, the battery suffers problems as lower power density, which limits the application of battery in electric vehicles and hybrid vehicles requiring high power and long cycle properties. Another spotlighted energy storage system is supercapacitor due to high power density and permanent usages, long cycle life (> 100,000 cycles). Supercapacitors obtain thousands of times higher power density than lithium ion batteries and much larger energy density than conventional capacitors. As illustrated in **Figure 1.2**, various energy storage devices are compared and presented in Ragone plot. With the high power capability than battery and the relatively large energy density as compared to the conventional capacitors, supercapacitors offer a promising devices to meet the increasing power demands of energy storage sytems.

Different research groups have done comprehensive study in the field of energy storage mechanisms and in the fabrication of supercapacitors. Many lucrative efforts have resultsed in the establishment of different synthesizing routes to construct competent frameworks for supercapacitor electrode. Various types of supercapacitors and their respective synthesizing materials are shown in **Figure 1.3**.

Supercapacitor can be applied to various kinds of applications such as power support, power start-up, memory back up, and energy storage. With these facts, supercapacitor is the promising energy devices in these days.

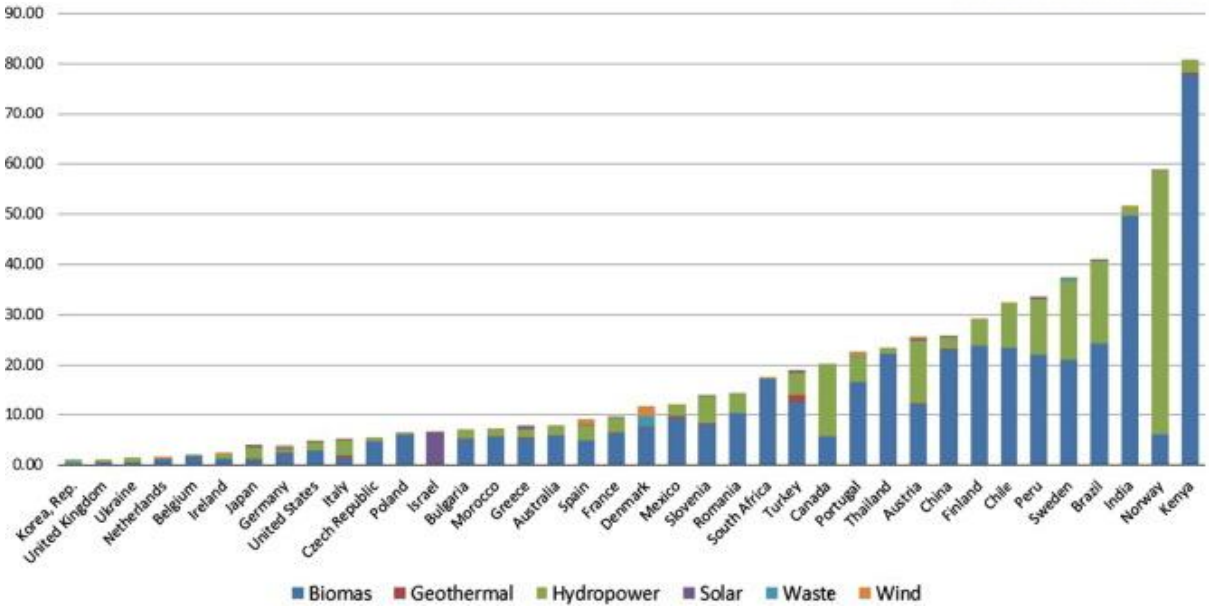

Figure 1.1. The percentage of renewable energy sources in total final energy consumption: 1990-2010.

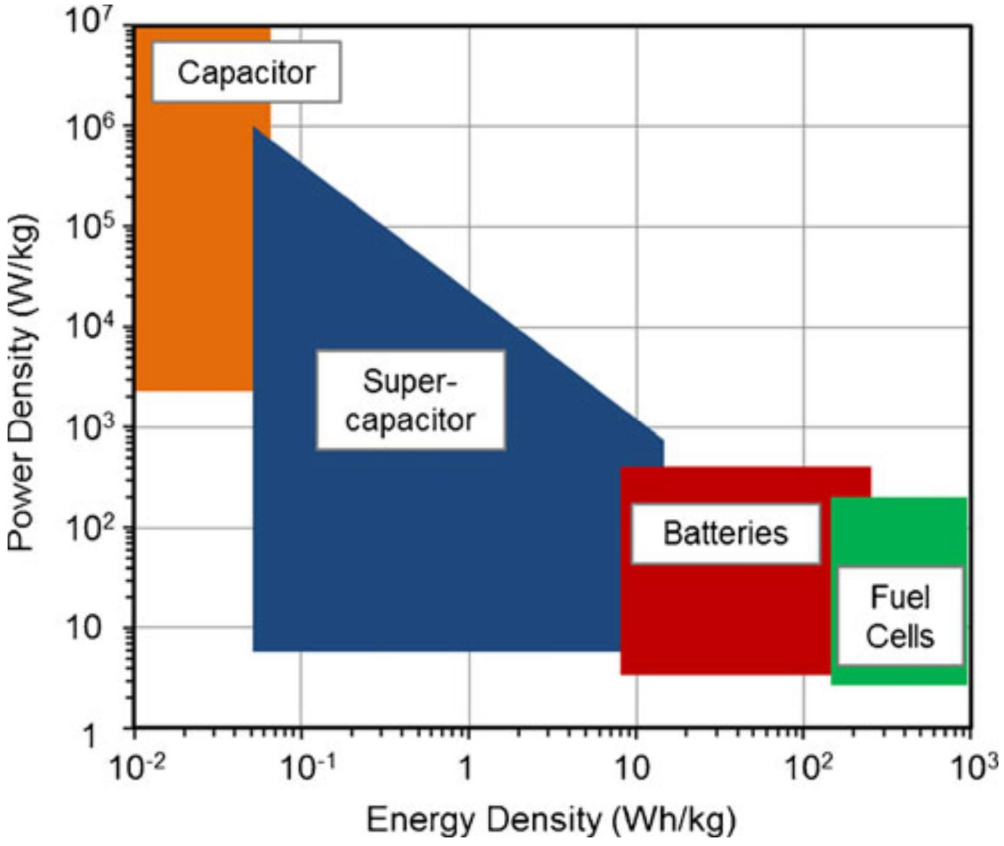

Figure 1. 2. Power density against energy density, also called a Ragone plot, for various energy storage and conversion devices.

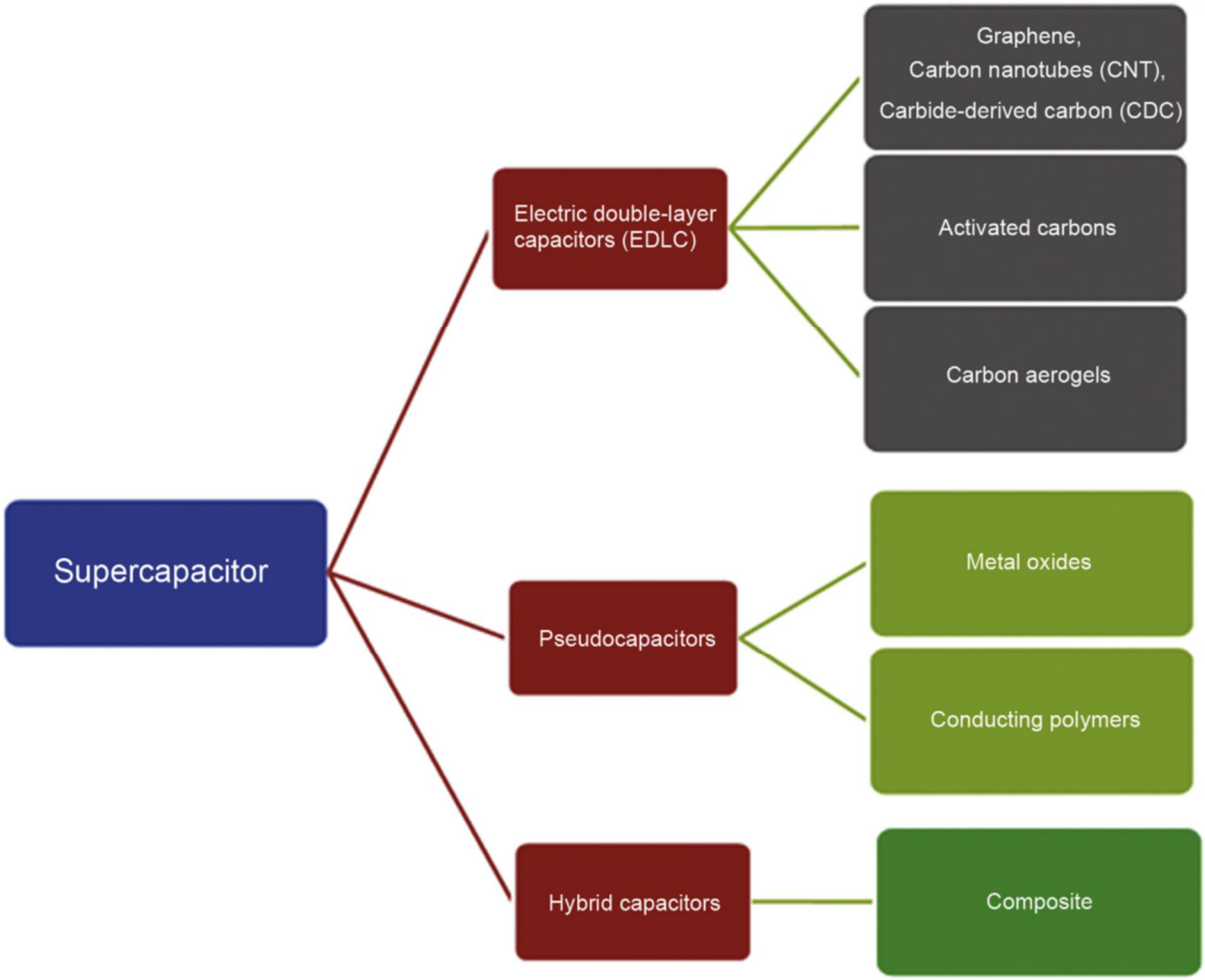

Figure 1.3. Types of supercapacitors and the commonly used electrode materials for their synthesis.

1.2 Working principles of supercapacitor

Working principles of the supercapacitors (EDLC and pseudocapacitor) are showed in the **Figure 1.4**. EDLCs provide the desired power density, fast charge/discharge rates and excellent cyclic stability. Activated carbon, carbon nanofibers, mesoporous carbon, carbon nanotubes (CNTs) and graphene have been widely used in the development of EDLCs. In EDLCs, the electrical energy is stored via a purely electrostatic charge process. It is occurred by adsorption of ions at the interface between the active material electrode and the electrolyte. Due to this fact, there is limitation to improve the capacitance because they only store the charges on the surface of the materials by electrostatic forces. Also, it delivers unsatisfactory energy density due to its limited interface area with the electrolyte. To address and overcome the limitation of the EDLCs, pseudocapacitors are newly designed. Pseudocapacitors feature fast and reversible redox reactions at the surface of active materials. The protons in electrolyte and the charges in the electrodes are combined on the surface of the electrode and then the active materials are reduced. With this mechanism, pseudocapacitors can store many charges on the surface of the electrode. Conductive polymers (e.g. PANi, polypyrrole, and poly [3,4-ethylenedioxythiophene]), and transition metal oxides (e.g., MnO2, NiO, and RuO2) are widely used in pseudocapacitors as active materials.

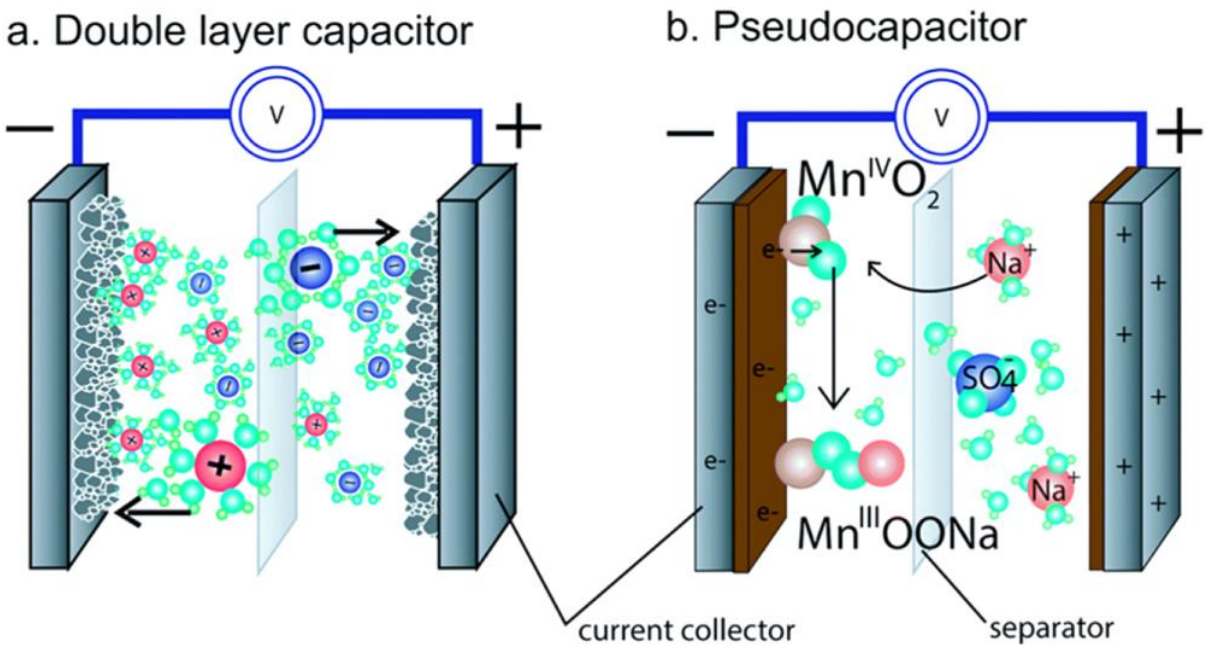

Figure 1. 4. Schematics of (a) an all-carbon EDLC and (b) a pseudocapacitor. Both devices have active materials (e.g. carbon and MnO2), a current collector, a separating membrane and electrolyte.

1.3 Morphology and size control of metal oxides/hydroxides

To operate supercapacitor, it is important to have a larger number of electrochemically accessible active sites. The specific capacitance of a metal oxide/hydroxide increases notably with an increase in its surface area because a large surface area is associated with more faradic active sites and in turn higher pseudocapacitance. To enhance active sites in the active material, the researches were investigated synthesizing various methods to control morphology and size. The first method is changing pH condition (**Figure 1.5**), Seconds, hollow shaped active materials with carbon sources (**Figure 1.6-7**), and then, with different temperature and pressure condition, it can successfully synthesized various morphology such as flower shaped, tube-shaped, particle-shaped, and so on (**Figure 1.8**). With SiO2 powder or polymer template, Inver-opal structure can be synthesized easily. In addition, there are various methods to make larger active sites.

However, many of the extensively studied active materials which have high theoretical capacitance values have poor electrical conductivity with long delay in the charge transportation rate and thus long charge time, poor capacitance at high scan rates, and long-term stability, including transition metal (Mn, Co, Ni, Ru, etc) oxides and hydroxides. One easy way to address the low conductivity problem of the active materials has been to mix them with conductive additives and binders before pasting them on the current collector. However, the incorporation of ancillary materials often results in inadequate contact at the interfaces of those materials, giving rise to detrimental grain boundaries, and limiting the performance of the supercapacitors. Therefore, to enhance the Faradaic redox ability of high-efficiency electrochemical energy-storage devices, it is desirable to have binder-free electrode materials with large surface area and intrinsically high conductivity. To overcome these problems, directly growing active materials on a 3D-metal current collector or compositing with other materials. 3D-metal current collector provides high surface area and good conductivity to help electronic transport in the active materials as well as control morphology and size conditions of active materials.

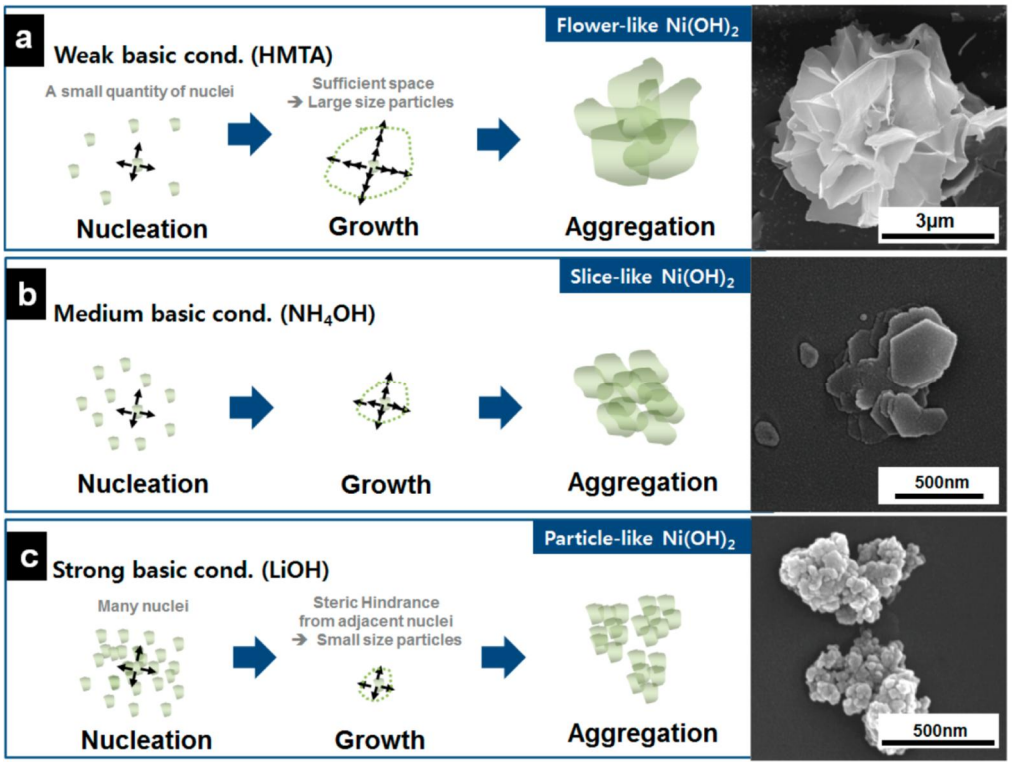

Figure 1. 5. Schematic diagram showing the formation process of (a) flower-, (b) slice-, (c) particle-like Ni(OH)2 under different pH conditions and the corresponding SEM images of as-prepared samples

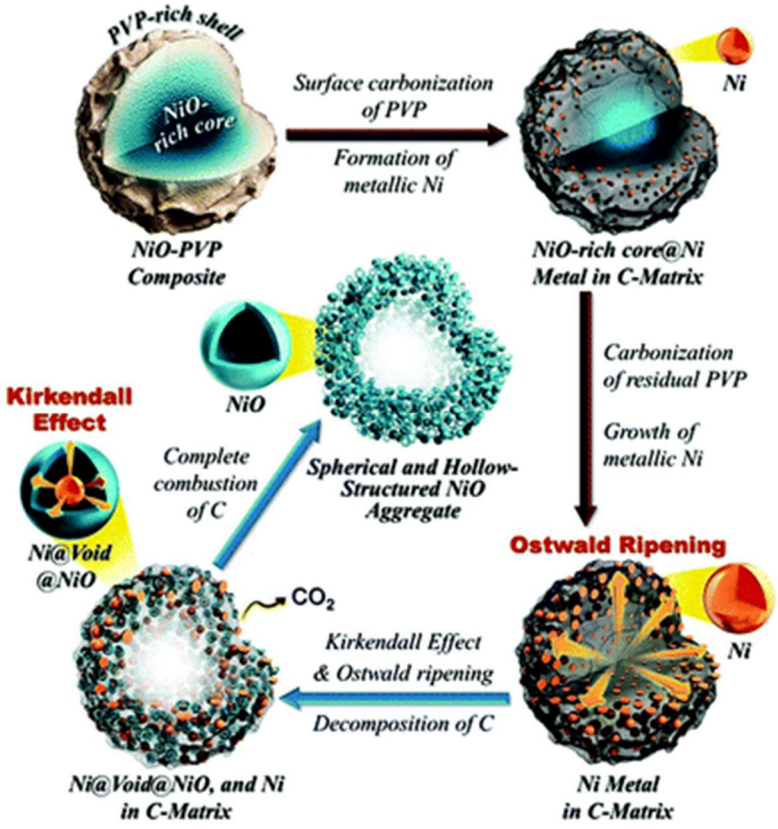

Figure 1.6. Schematic diagram for the detailed mechanism of formation for the spherical and hollow-structured NiO aggregate.

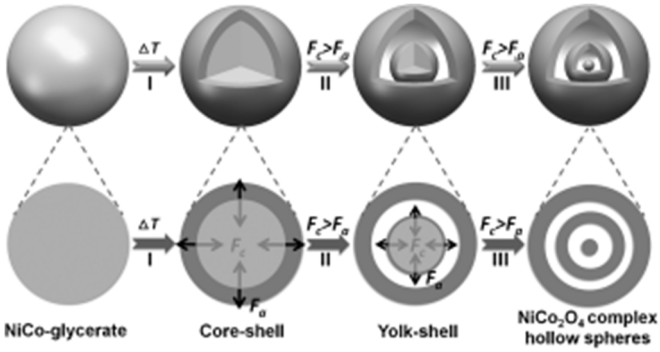

Figure 1. 7. Schematic illustration of the formation process of NiCo2O4 core-in-double-shell hollow spheres

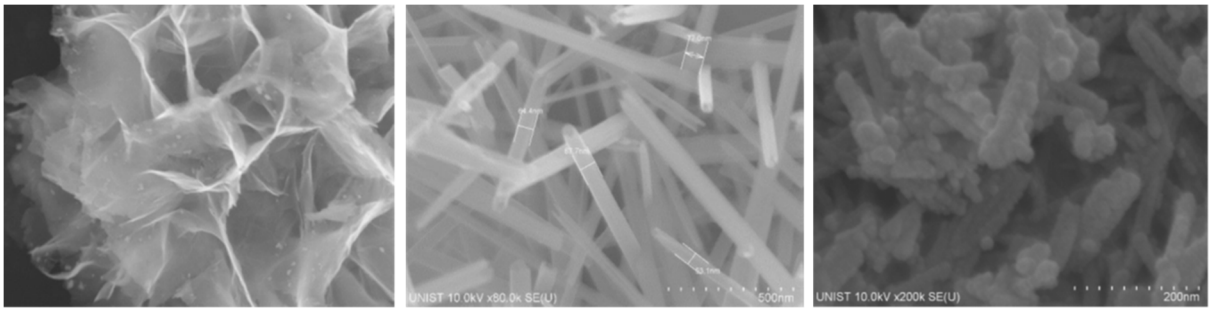

Figure 1. 8. SEM images of various morphology of metal oxides (Flower-NiO, Tube-MnO2, and Particle-Co3O4)

1.4 References

1. M. Bhattacharya, S. R. Paramati, I. Ozturk, and S. Bhattacharya, The effect of renewable energy consumption on economic growth: Evidence from top 38 countries, *Applied Energy*, 2016, **162**, 733-741.

2. C. Meng, O. Z. Gall, P. P. Irazoqui, A flexible super-capacitive solid-state power supply for miniature implantable medical devices, *Biomedical Microdevices*, 2013.

3. A. W. Anwar, A. Majeed, N. Iqbal, W. Ullah, A. Shuaib, U. Ilyas, F. Bibi, and H. M. Rafique, Specific Capacitance and Cyclic Stability of Graphene Based Metal/Metal Oxide Nanocomposites: A Review, *Journal of Materials Science & Technology*, 2015, **31**, 699-707.

4. K. Jost, G. Dion, and Y. Gogotsi, Textile energy storage in perspective, *Journal of Materials Chemistry A*, 2014.

5. S. I. Kim, J. S. Lee, H. J. Ahn, H. K. Song and J. H. Jang, Facile route to an efficient NiO supercapacitor with a three-dimensional nanonetwork morphology, *ACS Appl. Mater. Interfaces*, 2013, **5**(5), 1596-1603.

6. J. S. Cho, J. M. Won, J. –H. Lee, and Y. C. Kang, Synthesis and electrochemical properties of spherical and hollow-structured NiO aggregates created by combining the kirkendall effect and Ostwald ripening, *Nanoscale*, 2015, **7**, 19620.

7. L. Shen, L. Yu, X. –Y. Yu, X. Zhang, and X. W. Lou, Self-Templated Formation of Uniform NiCo2O4 Hollow Spheres with Complex Interior Structures for Lithium-Ion Batteries and Supercapacitors, *Angew. Chem. Int. Ed.*, **2015**, 54, 1868-1872.

Chapter 2. Ultrathin nickel hydroxide on carbon coated 3D-porous copper structures for high performance supercapacitors

2. 1. Introduction

In the view of the recent developments of various energy storage devices, supercapacitors have attracted tremendous attention over the past many years due to their high power density, long cycle life, fast charging/discharging rate within seconds, and low maintenance cost. Lots of research have been dedicated to investigating and designing proper active materials, current collectors, and electrolytes to improve specific capacitance of the supercapacitors.[1-5]

One of the most important parameters affecting the electrochemical activity and kinetic performance of supercapacitors is the good electrical conductivity of the electrodes, which permits fast electron transport. However, many of the extensively studied active materials which have high theoretical capacitance values are wide band gap semiconductors with poor electrical conductivity, including transition metal (Mn[6-7], Co[8], Ni[9-11], Ru[12], etc[13]) oxides and hydroxides.[14-15]

One easy way to address the low conductivity problem of the active materials has been to mix them with conductive additives and binders before pasting them on the current collector. However, the incorporation of ancillary materials often results in inadequate contact at the interfaces of those materials, giving rise to detrimental grain boundaries, and limiting the performance of the supercapacitors. Therefore, to enhance the Faradaic redox ability of high-efficiency electrochemical energy-storage devices, it is desirable to have binder-free electrode materials with large surface area and intrinsically high conductivity.[16]

In addition, it is important to have a large number of electrochemically accessible active sites, since not all of the surface of the electrode is electrochemically accessible when the materials are in contact with an electrolyte. The pore size of the electrode material also plays an important role, by increasing the number of electrochemically accessible surface sites.[17]

In light of these objectives, a three-dimensional nanostructure is one of the most desirable electrodes, since it can facilitate i) easy electron transport between the active materials and the current collector, ii) efficient contact between the electrolyte ions and active materials for Faradaic reactions, and iii) effective accessibility to the active materials on the 3D-current collector for enhanced electrochemical activity.[18]

α-type $Ni(OH)_2$ has been widely studied as one of most efficient active materials for supercapacitors,

due to its flexibility in forming complex three-dimensional (3D) structures, and its high theoretical capacitance value (3750 F/g).[19] However, the actual specific capacitance values of supercapacitors that have been reported for a wide variety of $Ni(OH)_2$ nanostructures are still far below the theoretical value. This is because the low conductivity problem has not been fully addressed, and the electrochemically active sites are limited only to the regions near the surface of the active materials in many cases.

Here, we report an ultrathin nickel hydroxide layer electrodeposited on a carbon-coated 3D-Cu (3D-C/Cu) structure as an efficient electrode for high performance supercapacitors. The 3D-porous C/Cu structure allows for both large electrochemically accessible active sties and high conductivity, due to direct contact between the 3D-C/Cu and the active materials. A thin layer of nickel hydroxide directly deposited onto 3D-C/Cu structure provides shortened pathways for electron transport and efficient electrode/electrolyte interfaces. The 3D-$Ni(OH)_2$/C/Cu electrode exhibited a specific capacitance of 1860 F/g at 1 A/g in a 1.0 M KOH aqueous solution, and 86.3 % and 86.5 % of the original capacitance value were maintained at a high current density of 50 A/g and after 10,000 cycles, respectively.

2. 2. Experimental details

2. 2. 1. Preparation of 3D-$Ni(OH)_2$/C/Cu electrodes and 3D-Mn_3O_4/C/Cu electrodes

Ultrathin dendritic $Ni(OH)_2$ was deposited on a carbon coated porous copper structure, producing 3D-$Ni(OH)_2$/C/Cu on a nickel film, as follows. All of the chemicals were of analytical grade and used without further purification. The nickel film was cleaned in ethanol for 10 min. The copper solution was prepared using 0.4 M of $CuSO_4$-$5H_2O$ and 1.5 M of H_2SO_4 dispersed in H_2O. On 1.1 cm^2 of the Ni, porous copper was formed at 3 A/cm^2 for 30 s. The prepared samples was cleaned in D.I. water and dried in a vacuum oven at 60 ^oC for 1 h. Then, 5 mM of glucose solution was prepared for the carbon coating. The as-prepared 3D-Cu substrate was dipped and dried in a vacuum oven at 60 ^oC for 2 h. The dried sample was heated in an inert condition at 500 ^oC for 30 min and then cooled to room temperature. An ultrathin film of $Ni(OH)_2$ was electrodeposited and 0.1 M of the $Ni(NO_3)_2$ was dissolved in H_2O. We optimized the amount of active material at 0.35 mg, which was very carefully measured by microbalance several times, such that there was no experimental error caused by measuring a small amount of active material. Pt was used as a counter electrode, and Ag/AgCl (sat. KCl) was used as a reference electrode. The ultrathin film of $Ni(OH)_2$ was deposited at a current of -10 mA/cm^2 vs. Ag/AgCl(sat. KCl) for from 20 s to 90 s. The mass of electrodes were measured using an ultra-microbalance.

2. 2. 2. Characterization

The morphologies of synthesized ultrathin $Ni(OH)_2$ electrochemically deposited on the carbon coated dendritic porous copper structure were characterized using FE-SEM (SEM, FEI/USA Nanonova 230), high-resolution TEM (FETEM, JEOL TEM 2100) at an accelerating voltage of 200kV, XPS, EDX, and BET.

2. 2. 3. Electrochemical characterization of the as-prepared electrode for supercapacitors

Cyclic voltammetry (CV) and galvanostatic charge-discharge tests were carried out using a classical three-electrode configuration. 3D- $Ni(OH)_2$/C/Cu was used as the working electrode. A platinum foil (1.0 cm^2) and Hg/HgO were used as the counter and the reference electrodes, respectively. The cyclic voltammograms were acquired at a potential range between 0.1 and 0.8V at different scan rates, and the charge/discharge processes were performed by cycling the potential from 0.1 to 0.8 V at different

current densities in a 1 M KOH aqueous electrolyte. The cyclic stability was evaluated by galvanostatic charge-discharge measurements at a current density of 200 A/g for over 10,000 cycles. All the electrochemical measurements were conducted using a computer controlled electrochemical interface (VMP3 biologic).

The specific capacitance of the three-electrode cell was obtained from the galvanostatic charge/discharge curves as: $C_s = I \cdot t/m_s \cdot (V\text{-}IR)$, where m_s (g) is the mass of the electrode, I (A) is the current density, t (s) is the discharge time and V (V) is the discharge voltage range. The specific capacitance of the asymmetric two-electrode, It, can be calculated from : $Cs = I \cdot t/m_t \cdot (V\text{-}IR)$, where mt (g) is the total mass of the working and counter electrode, I (A) is the current density, t (s) is the discharge time (and V (V) is the discharge voltage range. The energy density, E_{cell} (Wh/Kg), was estimated using the formula $E_{cell} = C_s V^2/2$ and the power density, P_{cell} (kW/kg), was estimated using the formula $p_{cell} = V^2/(4mR)$.

2. 3. Results and discussion

The synthetic strategy for the 3D-$Ni(OH)_2$/C/Cu electrode is illustrated in **Figure 2.1**. First, a 3D-porous dendritic Cu structure with continuous networks is fabricated on the Ni-film by the electrodeposition of Cu, using hydrogen bubbles as a template.[20-23] It can be seen that the 3D-Cu is composed of numerous small-branched Cu deposits with dendritic shapes forming a large 3D-porous structure. The pore size and thickness of the 3D-Cu depends on the deposition time, as shown in **Figure 2. 2**. Then, a thin layer of carbon is deposited on the 3D-Cu by pyrolyzing glucose, which has been dip-coated on the surface of the 3D-Cu, at 500 ºC. The carbon coating on the 3D-Cu was applied to protect the 3D-Cu, which has a relatively high reduction potential, from oxidation, without degrading the conductivity of the Cu, as checked in **Figure 2. 3**. At the same time, the carbon coating helps keep the Cu from dissolving into the electrolyte during the electrochemical test, and maintains its original dendritic morphology. Finally, a thin layer of $Ni(OH)_2$ active materials was grown on the 3D-C/Cu by electrodeposition. The amount of $Ni(OH)_2$ grown on the 3D-C/Cu was controlled by varying the electrodeposition time, as shown in **Figure 2. 4**.

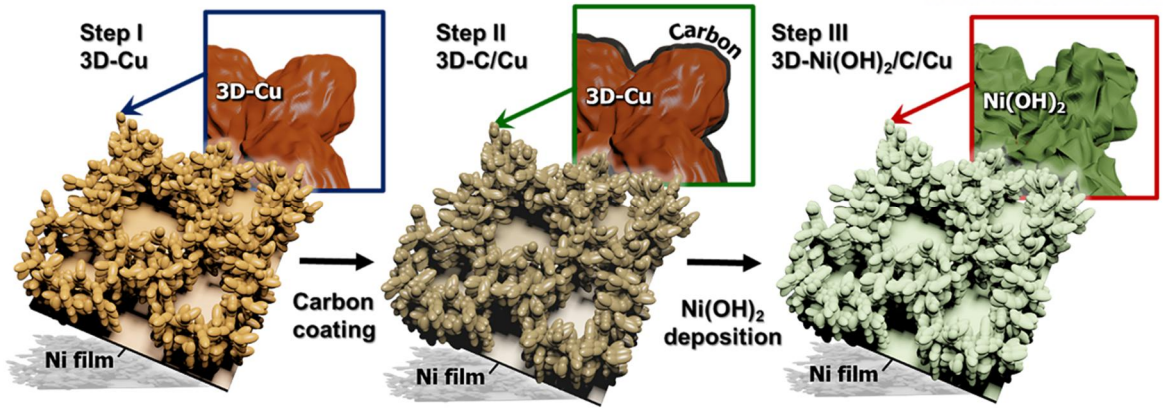

Figure 2. 1. A schematic of the growth process of 3D-$Ni(OH)_2$/C/Cu: I. Formation of dendritic porous Cu nanostructure (3D-Cu) on the Ni film. II. Carbon coating on the 3D-Cu. III. Ultrathin $Ni(OH)_2$ layer coating on the 3D-C/Cu.

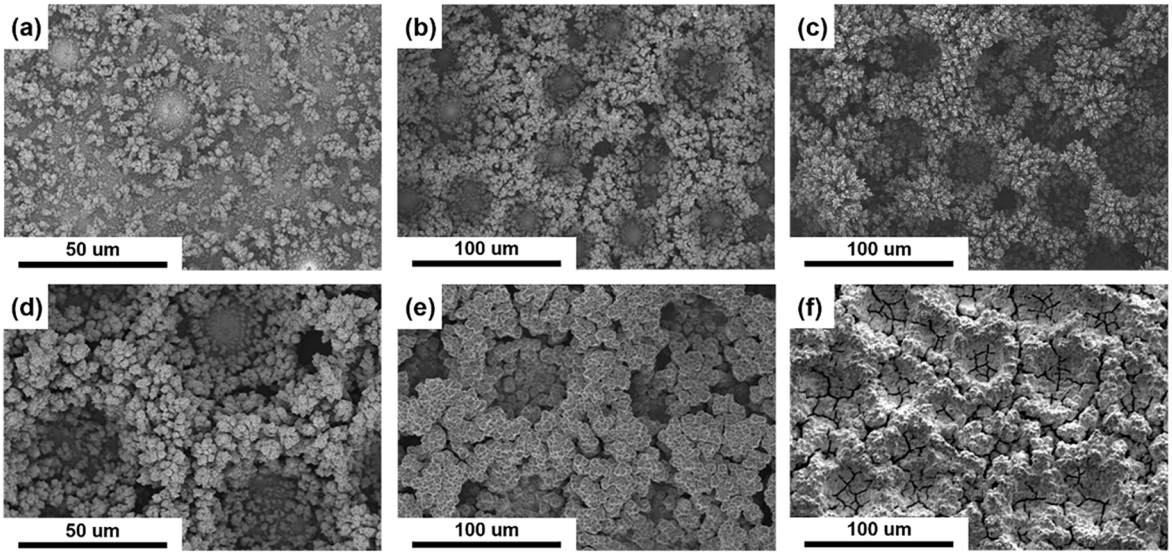

Figure 2. 2. SEM images of the 3D-porous copper structure(3D-Cu) on the Ni film created by electrochemical deposition process, for different periods of time (a) 5 s, (b) 15 s, (c) 30 s, (d) 45 s, (e) 60 s, and (f) 90 s. The optimized deposition time was 30 s.

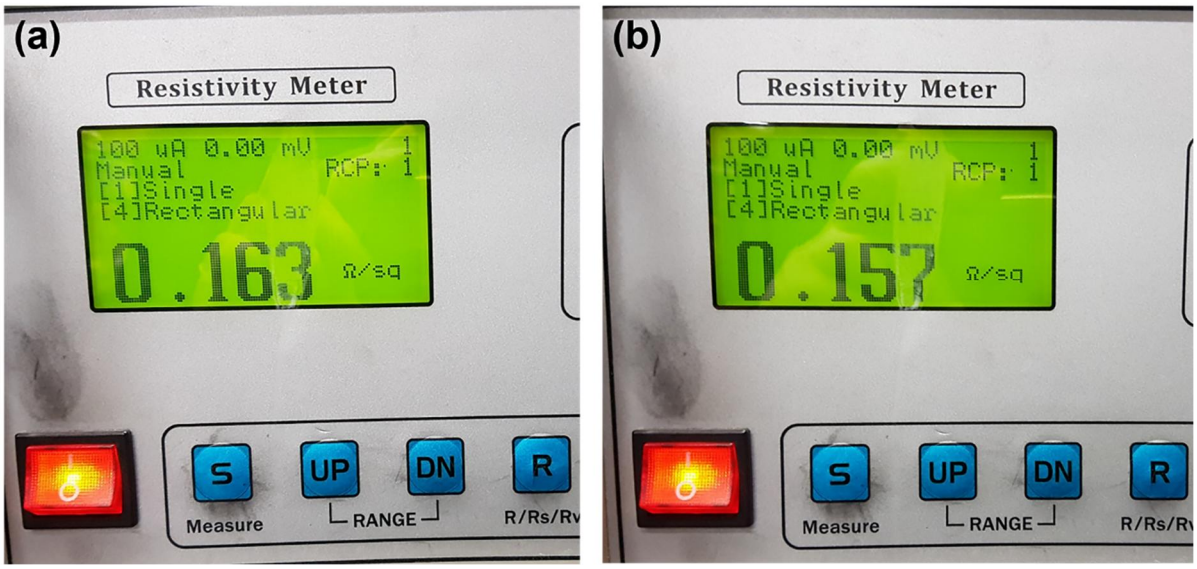

Figure 2. 3. Conductivity measurement data by four-point probe resistivity meter (FPP-RS8, DASOL ENG) of 3D-Cu (left) and 3D-C/Cu (Right)

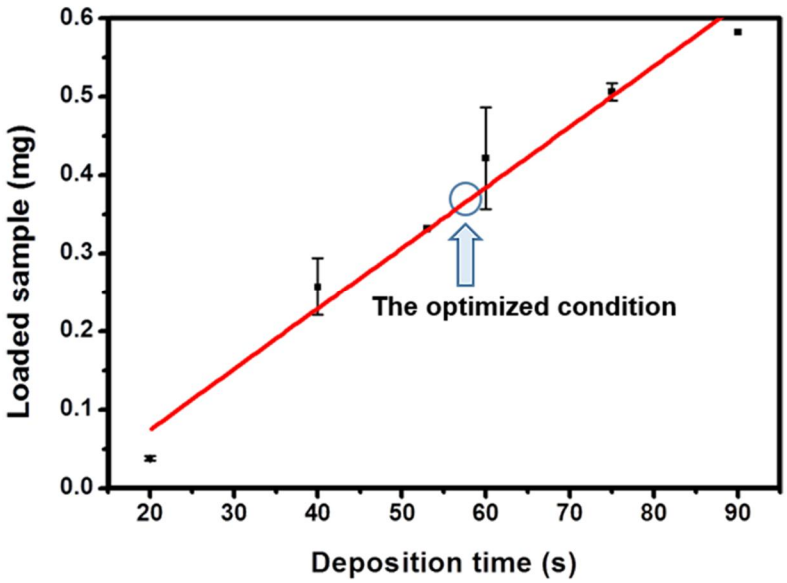

Figure 2. 4. Loading amount of $Ni(OH)_2$ on 3D-Cu as a function of deposition time.

Figure 2.5 shows scanning electron microscopy (SEM) and transmission electron microscopy (TEM) images of the 3D-$Ni(OH)_2$/C/Cu. As can be seen in **Figures 2. 5a-b**, the 3D-Cu frame prepared by the electrodeposition of Cu on the dynamic hydrogen bubble templates is a 3D-network with a few tens of micrometer-scale large pores finely decorated with sharp-edged, few hundred nanometer-scale branches.

The 3D-Cu structure was first constructed on a Ni-film current collector via facile electrochemical deposition accompanied by a hydrogen evolution reaction. Hydrogen bubbles supplied the pore-type template for the deposition of Cu, and due to dynamic evolution of the bubbles, the pore size increased with the distance away from the bottom of the substrate. This configuration is ideal for fast electrochemical reactions, because the bigger pores near the top surface can facilitate the transport of ions to the sublayers having smaller pores, leading to high utilization of the whole surface area without mass transfer limitations. Then a thin layer of carbon was coated on the surface of the 3D-Cu by the pyrolysis of glucose. The purpose of the carbon coating on the 3D-Cu was to prevent oxidation and the dissolution of copper in the electrolyte solution. SEM images of the 3D-Cu and 3D-C/Cu electrode in various magnifications are shown in **Figure 2. 6**. No obvious structural deformation or electrochemical performance degradation occurred.[24] Then, the $Ni(OH)_2$ active materials were densely deposited onto the 3D-C/Cu to form an ultrathin layer. The cross-sectional SEM image of the 3D- $Ni(OH)_2$/C/Cu in **Figure 2. 7** shows that entire 3D structures have been vertically grown with heights of 65~70 um, in the form of a highly porous structure. As shown in the BET data (**Figure 2. 8**), the surface area of the 3D-$Ni(OH)_2$/C/Cu is higher than that of the 3D-C/Cu, implying further decoration of the 3D-C/Cu during the deposition process of 3D-$Ni(OH)_2$. The 5-6 nm ultra-thin layer of $Ni(OH)_2$ on the porous 3D-C/Cu shortens the pathways between the $Ni(OH)_2$ active materials and 3D-C/Cu current collectors, provides high electrochemically active areas, and facilitate electrolyte penetration into the electrode.

TEM images of each layer in the 3D-$Ni(OH)_2$/C/Cu are shown in **Figures 2. 5c-d**. **Figure 2. 5d** clearly shows the configuration, consisting of copper in the inner layer, $Ni(OH)_2$ in the outer layer, and carbon in between the two layers. Layer-to-layer distances of 0.24 nm and 0.21 nm, corresponding to the (110) and (003) planes of crystalline $Ni(OH)_2$ and 0.21nm of the (111) plane of Cu, are confirmed.

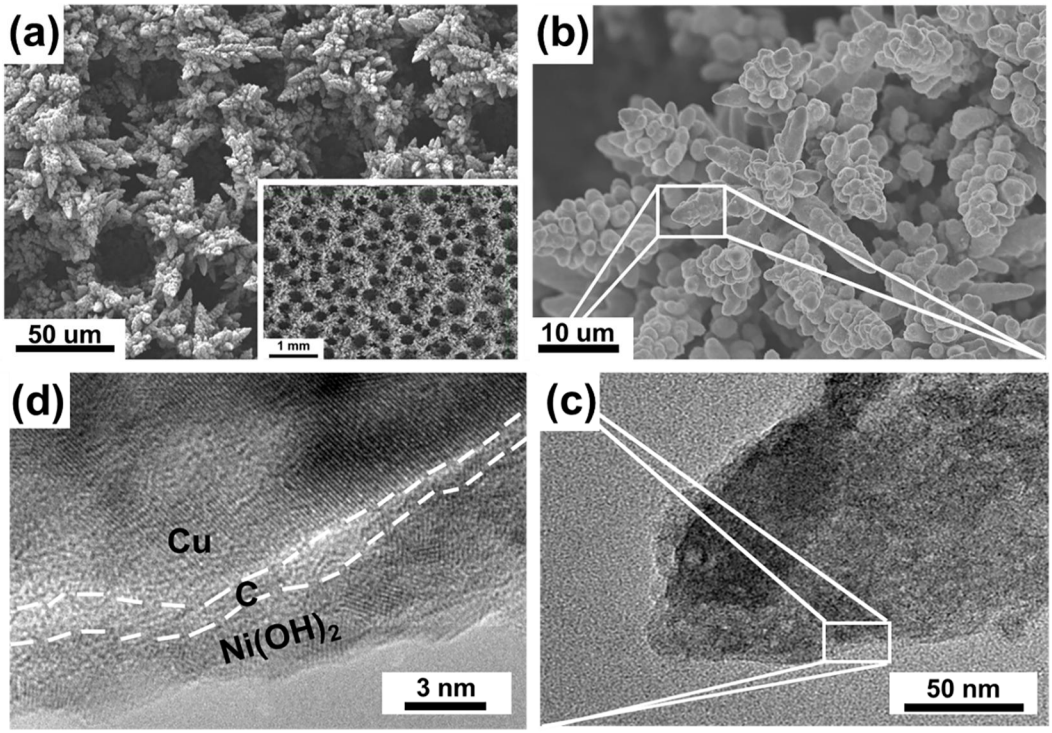

Figure 2. 5. Morphology of the as-synthesized 3D-$Ni(OH)_2$/C/Cu electrode: (a) Low-magnification and (b) high magnification SEM images of the 3D-$Ni(OH)_2$/C/Cu electrode. The inset in (a) shows the large-area uniform porous morphology of the 3D-$Ni(OH)_2$/C/Cu. (c) A TEM image of a single rod of 3D-$Ni(OH)_2$/C/Cu. (d) High resolution TEM image of the 3D-$Ni(OH)_2$/C/Cu with lattice fringes of $Ni(OH)_2$ and Cu, and an amorphous region of the carbon layer. The image shows the configuration of the Cu, C, and $Ni(OH)_2$ layer from inward to outward.

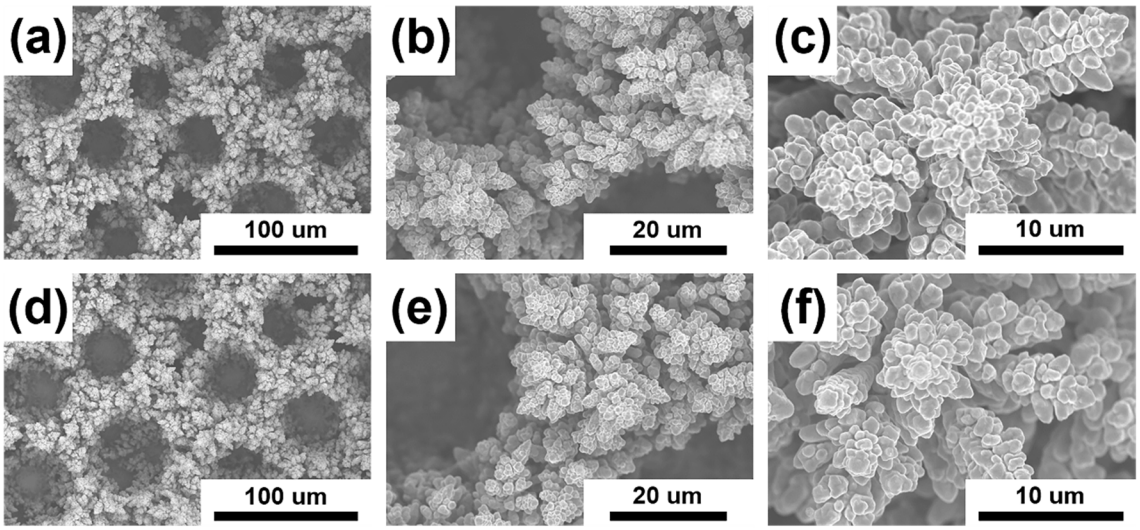

Figure 2. 6. Comparison of SEM images of the 3D-Cu electrode (a-c) and 3D-C/Cu electrode (d-f) at various magnifications.

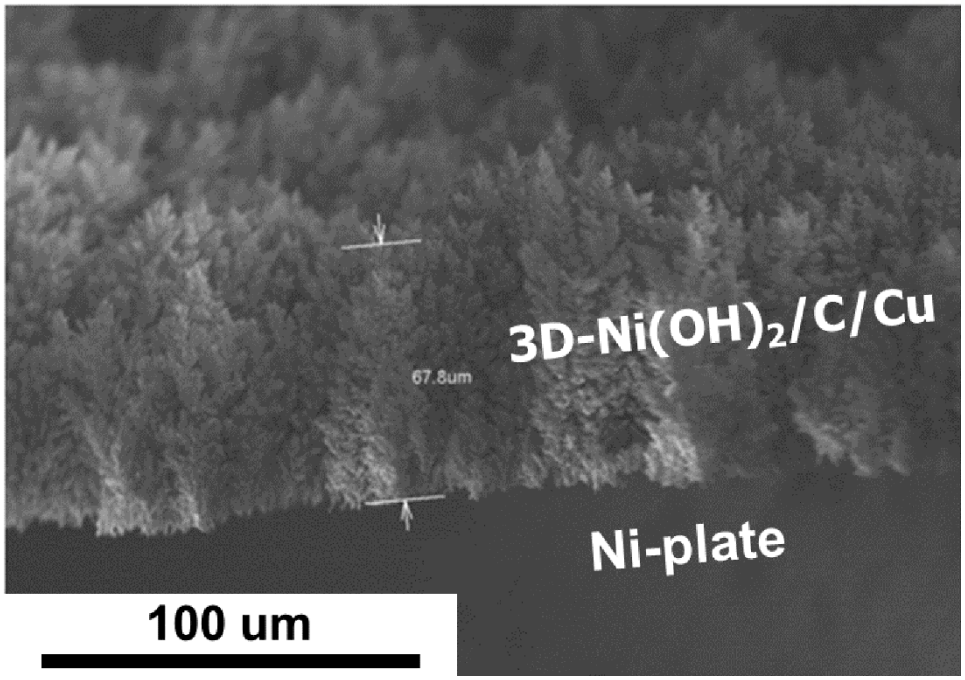

Figure 2. 7. SEM cross section image of the as-synthesized 3D-Ni(OH)$_2$/C/Cu.

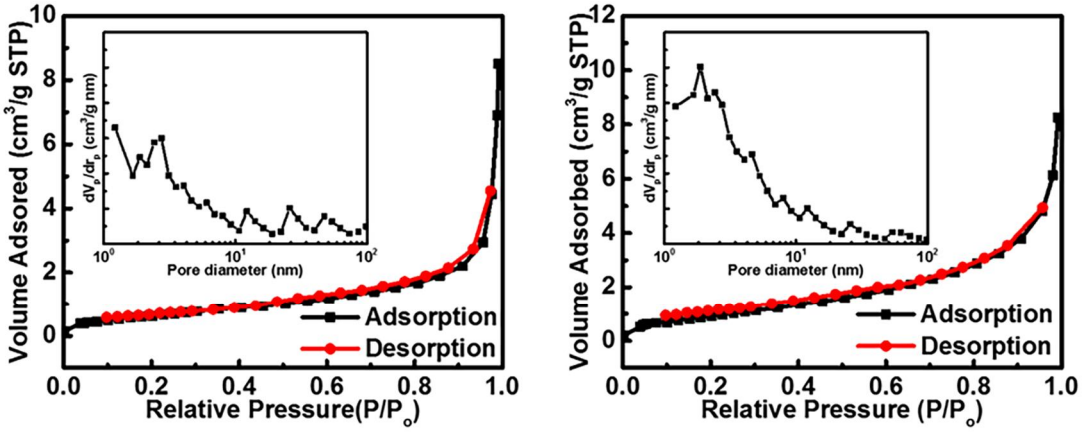

	Surface area (m^2/g)	Pore volume (cm^3/g)	Mean pore size (nm)
3D-C/Cu	2.47	0.012	19.54
3D-Ni(OH)$_2$/C/Cu	4.87	0.009	7.08

Figure 2. 8. The BET data of the 3D-C/Cu and 3D-Ni(OH)$_2$/C/Cu electrode. In the table, comparisons of specific surface area, pore volume and mean pore size are shown in detail.

XRD and energy dispersive X-Ray spectrometer (EDX) mapping data of the 3D-Ni(OH)$_2$/C/Cu on

the Ni film are shown in **Figures 2. 9-10**. As can be seen in the XRD pattern of the 3D-Cu, as compared with the 3D-C/Cu, Cu and CuO co-exist because the Cu is oxidized easily in air. The peaks at 43°, 51 °, and 74 ° correspond to the (111), (200), and (220) crystalline faces of Cu, respectively, whereas the peaks at 37 °, 62 ° correspond to the (002), (113) planes of CuO. However, with the carbon coating, the XRD patterns of the 3D-C/Cu do not show any peak related to CuO, suggesting the ability of the carbon layer to prevent the oxidation of Cu. The peaks at 12.1°, 33.4°, 59.8°, corresponding to the (003), (101), (110) planes of $Ni(OH)_2$ in the 3D-$Ni(OH)_2$/C/Cu XRD patterns (bottom) are very weak because the intensity of Cu is much stronger than the thin layer of carbon and $Ni(OH)_2$.

The elemental maps in **Figure 2. 10** show a uniform and continuous dispersion of Cu, Ni, O and C throughout the sample, indicating $Ni(OH)_2$ and carbon coating are well formed on the 3D-Cu substrate. The X-ray photoelectron spectroscopy (XPS) data in **Figure 2. 11** further confirms the successful deposition of $Ni(OH)_2$ on the3D-C/Cu.[25-26]

In order to further confirm the chemical composition of 3D-$Ni(OH)_2$/C/Cu, XPS (X-ray Photoelectron Spectroscopy) was examined to investigate the electronic state of the elements in the near surface region. **Figure 2. 11a** shows the C 1s peak, which can be deconvoluted into three peaks corresponding to C-C, C-O and O-C=O moieties. The binding energy at 284.5eV is originated from the carbon coating layer on 3D-Cu created by annealing the glucose layer. The XPS spectrum of the Cu 2p region of the electrode is shown in **Figure 2. 11b**. The peaks centered at 934.1eV and 954.2eV correspond to $Cu2p^{3/2}$ and $Cu2p^{1/2}$, respectively. The existence of satellite peak in the spectrum suggests the presence of copper in the electrode as Cu(II). The Ni 2p peak at the binding energy at 943eV as shown in **Figure 2. 11c** was best fitted with two spin orbit doublets, which are characteristic of Ni^{2+} and Ni^{3+}, and two shakeup satellites (indicated as "Sat."). Two major peaks with binding energies at 855.2 and 872.6 eV correspond to Ni $2p^{3/2}$ and Ni $2p^{1/2}$, respectively, yielding a spin-energy separation of 17.4 eV, characteristic of the Ni(OH)2 phase. O 1s spectrum in **Figure 2. 11d** is deconvoluted into two major peaks. One of the major peaks correspond to OH- originated from $Ni(OH)_2$ and other peaks which is related with C-O and O-C=O bonding inherited from carbon source are at 531.5, and 532.5eV, respectively. The peak at 531.7eV that is assigned to O 1s photoelectrons, consisting of two oxygen bonds (531.5eV and 523.5eV), which can be associated with chemi-absorbed Ni(OH)2 and the abrupt augmentation of single or double bonding between C and O.

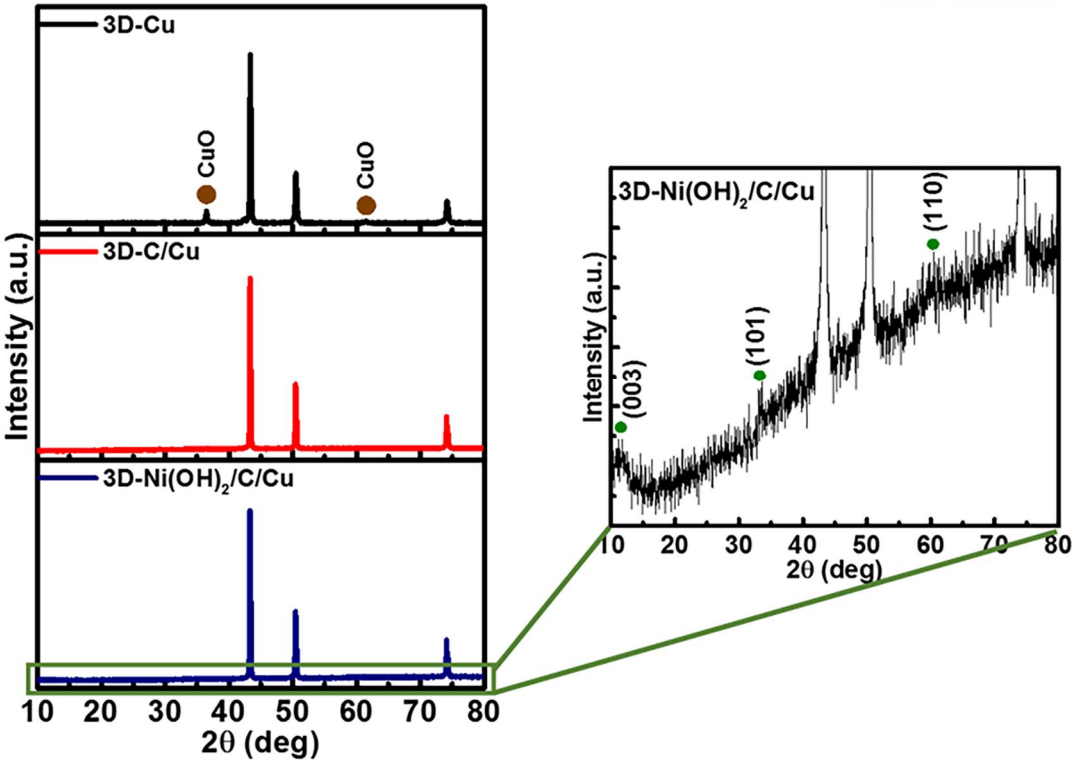

Figure 2. 9. Comparison of XRD patterns of 3D-Cu, 3D-C/Cu, and 3D-Ni(OH)$_2$/C/Cu to determine whether the 3D-Cu structure is oxidized or not (left). Enlarged XRD patterns of the 3D-Ni(OH)$_2$/C/Cu to confirm Ni(OH)2 exactly.

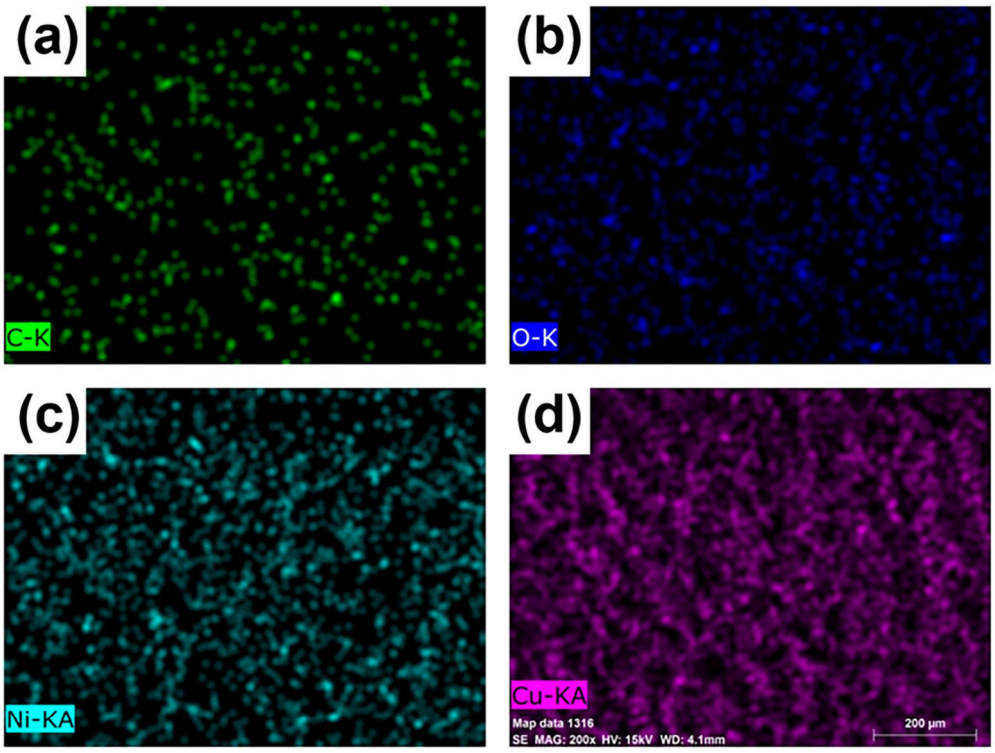

El	AN	Series	Unn.C [wt,%]	Norm.C [wt,%]	Atom.C [at,%]	Error(1 sigma) [wt,%]
C	6	K-series	3.72	2.56	11.48	0.98
O	8	K-series	2.97	2.04	6.87	0.62
Ni	28	K-series	16.36	11.26	10.33	0.61
Cu	29	K-series	122.29	84.14	71.32	4.01
		Total:	145.34	100.00	100.00	

Figure 2. 10. Total EDS elemental mapping images of the as-prepared 3D-Ni$(OH)_2$/C/Cu electrode. And the detail peaks for (a) C, (b) O, (c) Ni and (d) Cu. The table of ratios of all elements, respectively.

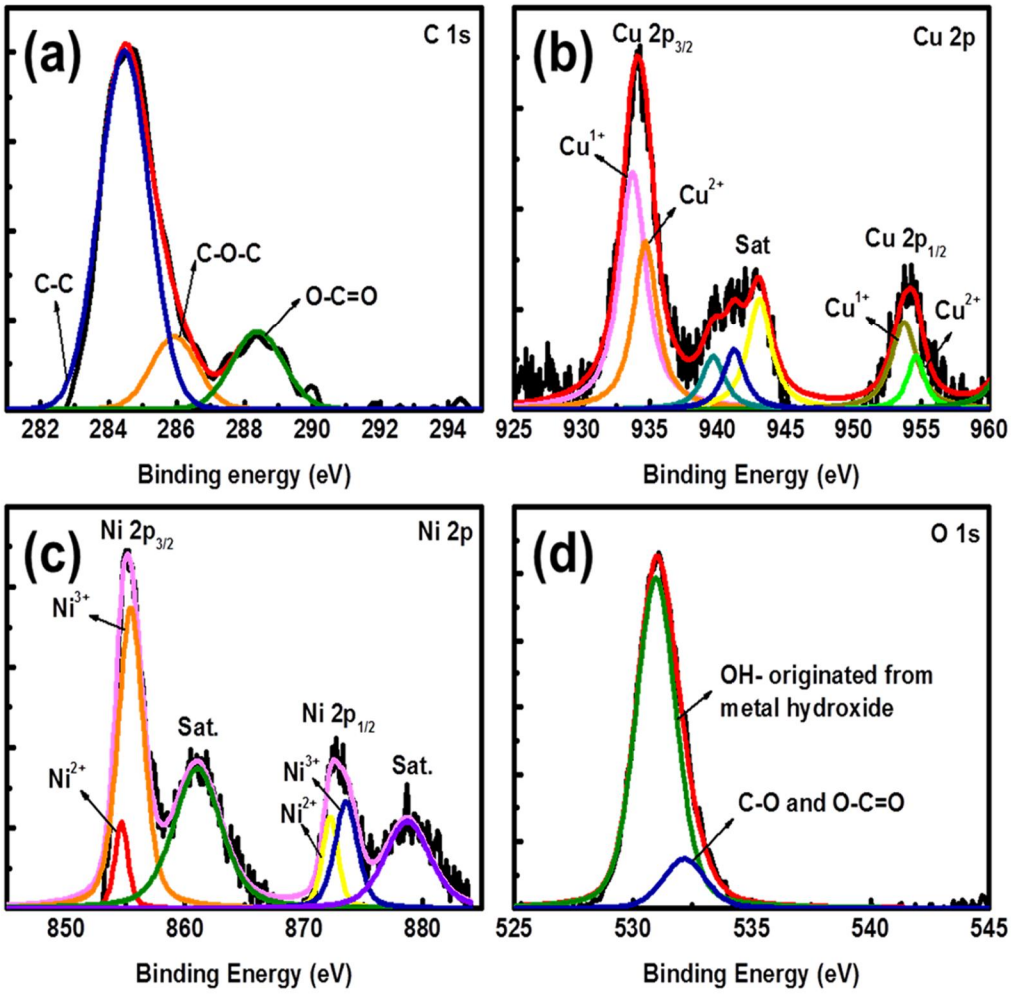

Figure 2. 11. XPS spectra of (a)C 1s, (b) Cu 2p, (c) Ni 2p, and (d) O 1s for the 3D-$Ni(OH)_2$/C/Cu electrode.

As illustrated in **Figure 2. 12**, the 3D-$Ni(OH)_2$/C/Cu can be considered an excellent electrode for a supercapacitor as compared with the typical Ni-film structure. The advantages of the 3D-$Ni(OH)_2$/C/Cu/Ni-film (b) over a conventional $Ni(OH)_2$/Ni-film (a) are as follows. i) Compared to the flat surface electrode, a thinner layer of active material is formed on the 3D-Cu electrode due to the larger surface area of the 3D-C/Cu, when the same amount of active material is deposited. This allows a greater portion of the $Ni(OH)_2$ active materials to be directly in contact with the current collector, and thus shortens the pathways between the surface of the active materials and the highly conductive current collector. This facilitates fast electron transport. ii) Numerous, various sized pores (from micro to macroscale) in the 3D-$Ni(OH)_2$ networks facilitate the migration of electrolyte ions with minimum diffusive resistance to mass transport, and thus reduces the portion of dead volume (the large number of active sites) at high current density. iii) This electrode does not need any binder, which not only eliminates the additional contact resistance between the current collector and the active material (by reducing IR loss) but also reduces the total mass of the electrode.

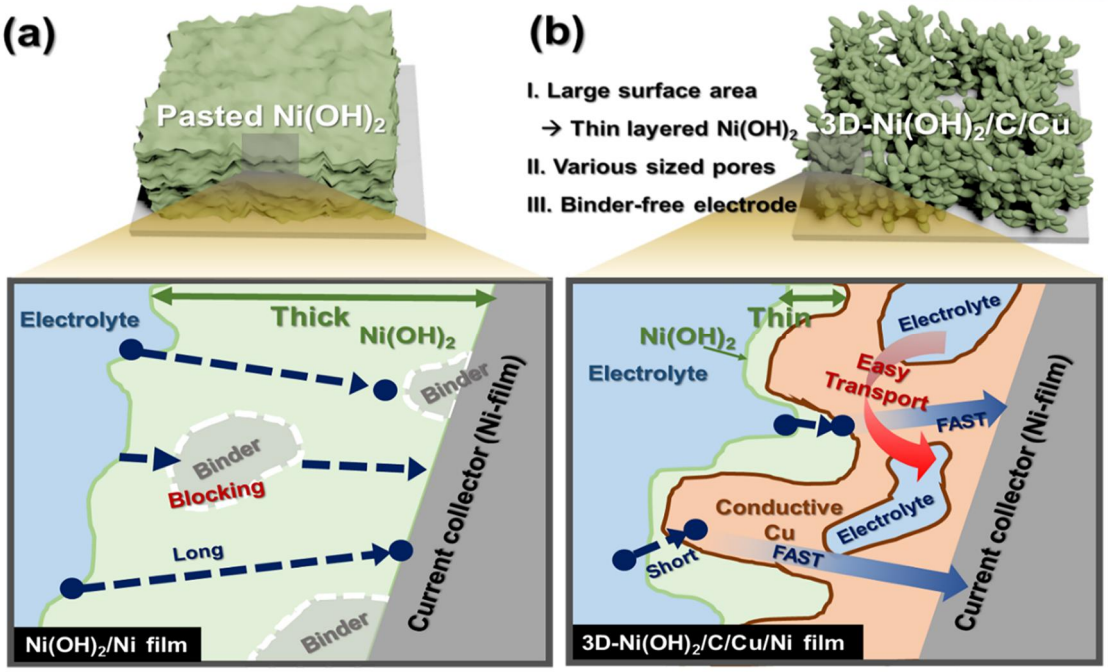

Figure 2. 12. A schematic of the electron transfer mechanism of the $Ni(OH)_2$ active materials deposited (a) on a typical Ni plate current collector and (b) on the 3D-C/Cu/Ni plate.

The electrochemical properties of the 3D-$Ni(OH)_2$/C/Cu electrode were evaluated in a supercapacitor using a three-electrode system in a 1 M KOH aqueous solution.

Figure 2. 13a presents the cyclic voltammetry (CV) curves of the $Ni(OH)_2$/C/Cu at various scan rates. A pair of oxidation/reduction peaks can be seen, implying the presence of the reversible Faradic reaction of:

$$\alpha - Ni(OH)_2 \; + \; OH^- \; \leftrightarrows \; \gamma - NiOOH \; + \; H_2O \; + \; e^-$$

As the scan rate increased, the oxidation peaks shifted to a more positive position, and the reduction peaks moved to a more negative position, due to an increase in the internal diffusion resistance within the active materials. However the symmetric characteristic of the oxidation and reduction peaks indicates the excellent reversibility of the 3D-$Ni(OH)_2$/C/Cu electrode.

In addition, the shapes of the CV curves show almost no significant change as the scan rates increase from 5 to 50 mV/s, implying improved mass transport, and excellent electron conduction through the electrode. The electrochemical performance of the 3D-$Ni(OH)_2$/C/Cu electrode was found to be better than previously reported ones with similar structured electrodes.[20-22] The as-prepared electrode not only showed high specific capacitance, but also maintained its excellent electrochemical performance at high charge/discharge rates. As can be seen in the CVs of 3D-C/Cu and 3D-$Ni(OH)_2$/C/Cu measured at a scan rate 20 mV/s in **Figure 2. 15**, the current response of 3D-C/Cu (current collector only) is negligible compared to that of 3D-$Ni(OH)_2$/C/Cu. Therefore, we obtained the capacitance value of 3D-$Ni(OH)_2$/C/Cu by considering only the mass of $Ni(OH)_2$. Therefore, we obtained the specific capacitance value based on the pure mass of $Ni(OH)_2$ when we obtained the capacitance value of 3D-$Ni(OH)_2$/C/Cu.

In **Figure 2. 13b**, the 3D-$Ni(OH)_2$/C/Cu electrode exhibits very good galvanostatic charge/discharge (GCD) performance as a function of current density. From the GCD measurements at different current densities, the IR drops at the current charge-discharge currents (I_D) of 1, 2, 5, 10, 20 and 50 A/g were 0.55, 0.95, 3.44, 6.32, 13.46, and 34.46 mV, respectively. The ESR (equivalent series resistance) ($IR/2I_D$), which is the main contributor to power loss during charging and discharging of the capacitor, was calculated for all I_D ranges from 0.28 Ω to 0.35 Ω, and found to be an average of 0.31 Ω. The ESR was considerably lower than the other reported values for electrodes with a similar mass loading of $Ni(OH)_2$.[27]

The 3D-$Ni(OH)_2$/C/Cu electrode showed specific capacitances of 1860, 1839, 1819, 1769, 1716, and 1606 F/g at different densities of 1, 2, 5, 10, 20, and 50 A/g, respectively (**Figure 2. 13c**). These values are substantially higher than those for a similar electrode. Almost 86.3 % capacitance was retained at

the high current density of 50 A/g, which confirms the excellent rate capability. These results highlight the advantages of the 3D-$Ni(OH)_2$/C/Cu, which demonstrated good ion diffusion and electron transport ability at high current densities, features which are critical for practical supercapacitor applications.

The long-term cycling stability of the electrode materials is another critical requirement for practical applications. **Figure 2. 13d** depicts the specific capacitance retention as a function of the cycle number, up to 10,000 cycles, at a current density of 200 A/g. The loss in specific capacitance at 10,000 cycles was only 14 %, which is highly superior to other $Ni(OH)_2$-based electrodes as compared in **Table 2. 1.**[27-31]

When galvanostatic charge/discharge performance and cycle stability of 3D-$Ni(OH)_2$/Cu electrode were explored, only 52.1 % and 43.3 % of the original capacitance were retained at the high current density of 50 A/g and after 10,000 cycles, respectively (dotted black line in **Figures 2. 13c-d**, the detailed CV and charge/discharge curves are in **Figure 2. 16**), which proves the positive role of the carbon layer in 3D-$Ni(OH)_2$/C/Cu.

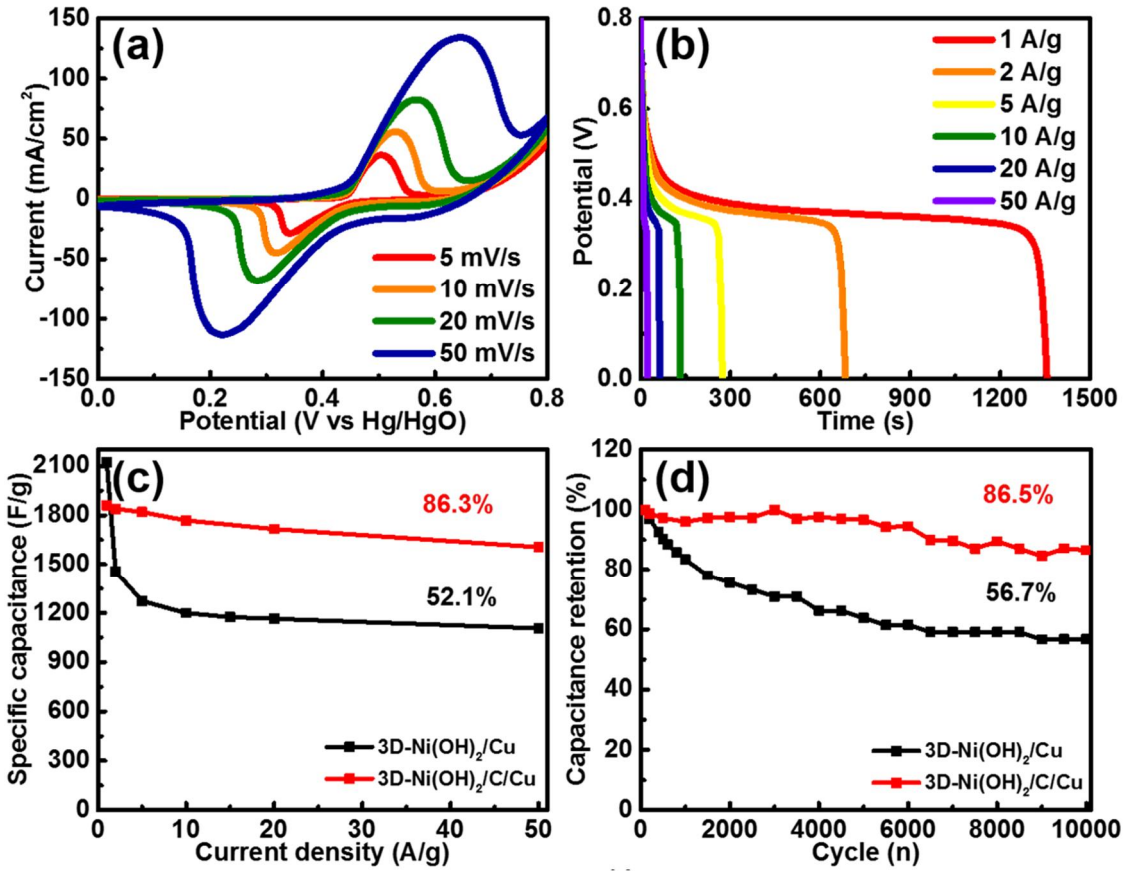

Figure 2. 13. Electrochemical characterization of the 3D-Ni(OH)$_2$/C/Cu electrode in a three-electrode system. (a) CV curves at various scan rates in 1 M KOH. (b) Discharge curves during galvanostatic charge/discharge measurement. (c) Specific capacitance of 3D-Ni(OH)$_2$/C and 3D-Ni(OH)$_2$/C/Cu as a function of the current density based on the galvanostatic charge/discharge measurement (d) Cycle performance of the 3D-Ni(OH)2/Cu and 3D-Ni(OH)$_2$/C/Cu electrode at a current density (specific capacitance) of 200 A/g.

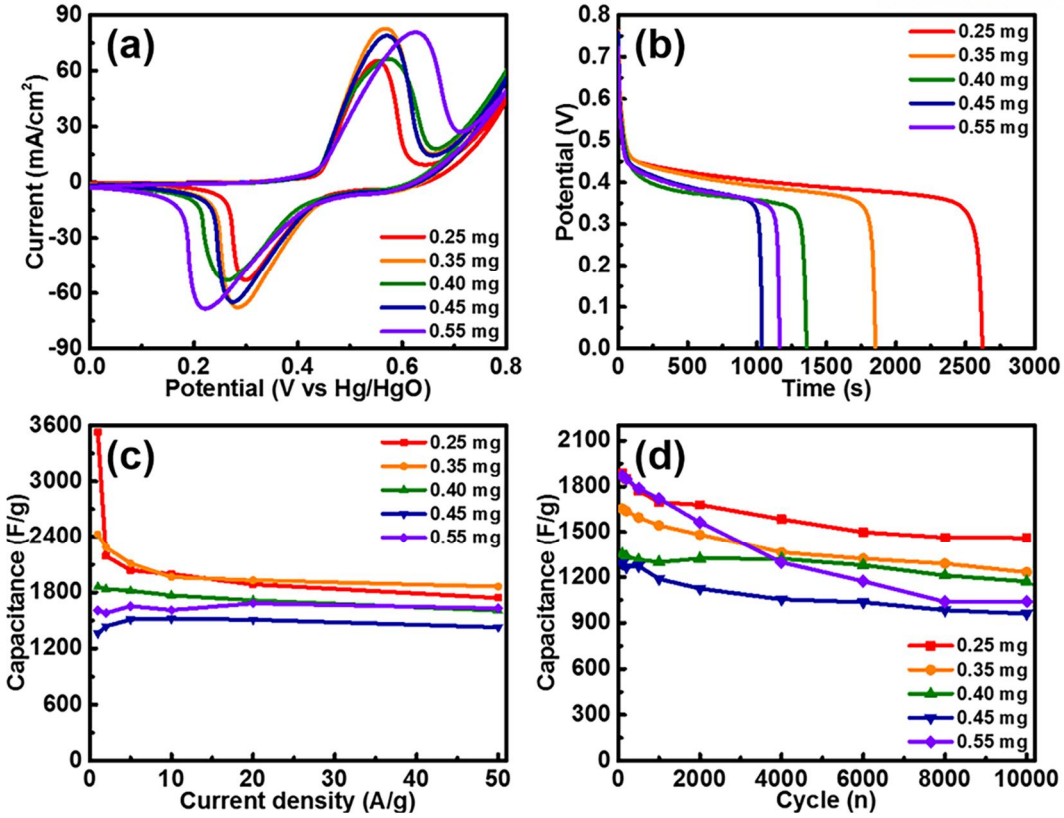

Figure 2. 14. Three-electrode electrochemical measurements of the 3D-Ni(OH)$_2$/C/Cu composite in a 1M KOH aqueous solution with various amounts of Ni(OH)$_2$. (a) CV curves for different amounts of Ni(OH)$_2$ deposited at 20mV/s. (b) Galvanostatic charge/discharge curves at 1A/g, (c) Specific capacitance as a function of the current density. (d) Cycling performance at 200A/g.

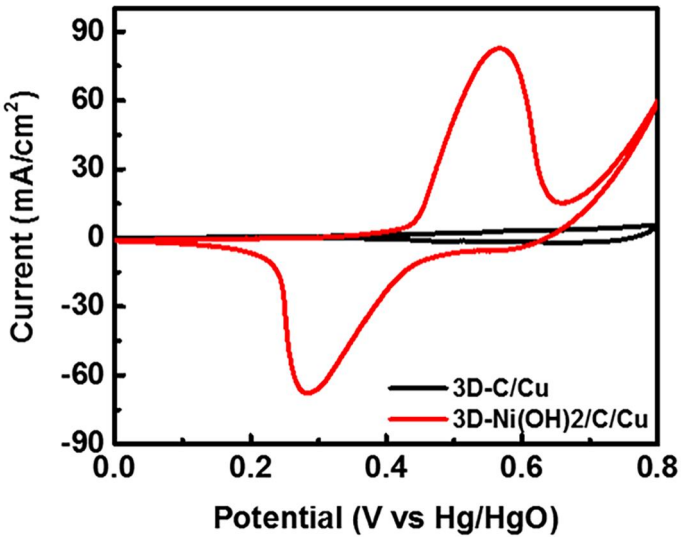

Figure 2. 15. Comparison of CV curves between 3D-C/Cu (Current collector) and 3D-Ni(OH)$_2$/C/Cu electrode.

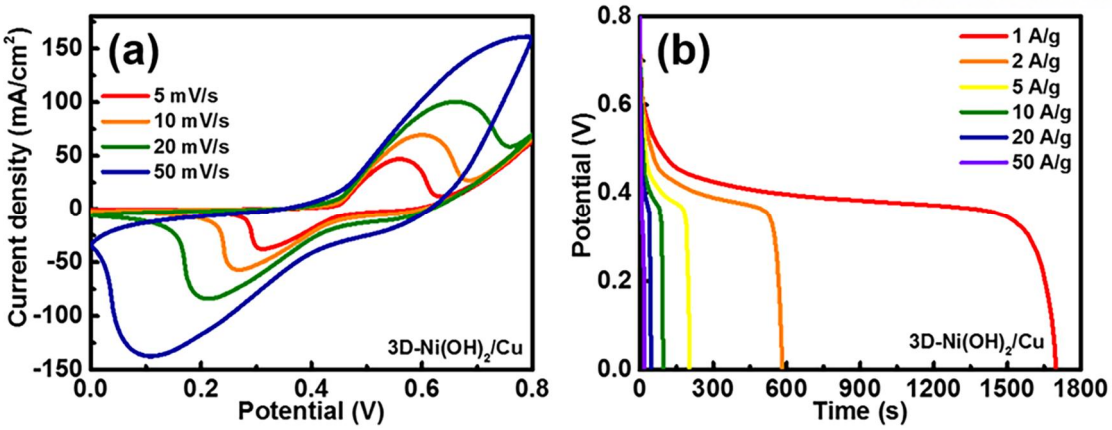

Figure 2. 16. Three-electrode electrochemical measurements of the 3D-$Ni(OH)_2$/Cu composite in a 1 M KOH aqueous solution. (a) CV curves at various scan rates, (b) discharge curves during galvanostatic charge/discharge measurement.

Electrode	Cs (F/g)	Rate capability	Cycle stability	DOI
Amorphous Ni(OH)2 nanospheres on nickel film	2188 (at 1 mV/s)	43% (1 mV/s to 20 mV/s)	72% 10000 cycles	10.1038/ncomms2932 [27]
Ni(OH)2 nanoplates grown on graphene	1335 (at 2.8 A/g)	70% (2.8 A/g to 45.7 A/g)	Almost 100% (20000 cycles)	10.1021/ja102267j [28]
α-Ni(OH)2 on nickel foam	3152 (at 4 A/g)	8.9% (4 A/g to 16 A/g)	48% (3000 cycles at 4 A/g)	10.1039/B815647F [29]
Ultrathin Ni(OH)2 nanosheet on nickel foam	2384.3 (at 1 A/g)	54% (1 A/g to 4 A/g)	75% (3000 cycles at 5 A/g)	10.1016/ j.nanoen.2014.10.029 [30]
Nanoporous Ni(OH)2 thin film on 3D ultrathin graphene foam	1560 (at 0.5 A/g)	70% (0.5 A/g to 10 A/g)	65% (1000 cycles at 10 A/g)	10.1021/nn4021955 [26]

3D-Ni(OH)2/C/Cu on Ni film_0.35 mg	2430 (at 1 A/g)	76.7% (1 A/g to 50 A/g)	74.5% (10000 cycles at 200 A/g)	This work
3D-Ni(OH)2/C/Cu on Ni film_0.40 mg	1860 (at 1 A/g)	86.3% (1 A/g to 50 A/g)	86.5% (10000 cycles at 200 A/g)	This work

Table 2. 1. Comparison of electrochemical performance of 3D-Ni(OH)2/C/Cu in a three-electrode system with electrodes in other previous paper.

Conventionally, when the $Ni(OH)_2$ electrode is charged/discharged, the electrode is under an equilibrium of the reaction between $\alpha - Ni(OH)_2$ and $\gamma - NiOOH$ accompanied by the structural change. The repeated volume expansion/shrinkage due to the interlayer spacing difference between $\alpha - Ni(OH)_2$ and $\gamma - NiOOH$ causes $Ni(OH)_2$ to be detached from the current collector at a high scan rate or during the long cycling process.[32-34] However, we overcame these problems by applying the protective carbon layer, as shown in **Figure 2. 19.** Therefore, our $Ni(OH)_2$ material is maintained well after 10,000 cycles. In our study, the tightly deposited amorphous carbon layer between the $Ni(OH)_2$ and Cu can buffer the volume change during the transformation, and protect the active material and 3D structure. Consequently, the 3D-$Ni(OH)_2$/C/Cu electrode readily retained the original specific capacitance value compared with other electrodes with similar $Ni(OH)_2$ active materials. To confirm this, SEM images of the 3D-$Ni(OH)_2$/C/Cu electrode before and after 10,000 cycles are presented in **Figures 2. 17a** and **2. 18.** The overall morphology of the dendritic 3D-porous structure remains the same without noticeable cracks or damage, which leads to excellent long-cycle stability. (The excellent electrochemical performances as a function of area are shown in **Figure 2. 19**) The XRD and XPS data of 3D-$Ni(OH)_2$/C/Cu before and after 10,000 cycles are shown in **Figures 2. 20-21**, respectively.

The electrochemical impedance spectroscopy (EIS) shows the variations in the interior electrode resistance, or the interfacial resistance between the electrode and the electrolyte at specific operating frequency ranges in the devices. A semicircle at high frequencies, which corresponds to the charge transfer resistance (R_{ct}) at the electrode-electrolyte interface, is followed by a linear slope in the medium or low frequency regions between 0.1 Hz and 1 MHz, as shown in **Figures 2. 17b** and **2. 22-23.** The diameter of the semicircle (R_{ct}) is less than 1 Ω, suggesting a very high charge-transfer rate between the electrolyte and the $Ni(OH)_2$ active material. The straight line in the medium frequency region can be ascribed to Warburg impedance, which is related to the diffusion of the electrolyte within the electrode. The onset point on the real axis (R_s) in the high-frequency region reflects intrinsic resistance, and the electrical contact resistance, of the electrode materials. The very small contact resistance value of 0.65 Ω proves there was no interruption in the conductivity of the 3D-$Ni(OH)_2$/C/Cu, or caused by the presence of the carbon layer.

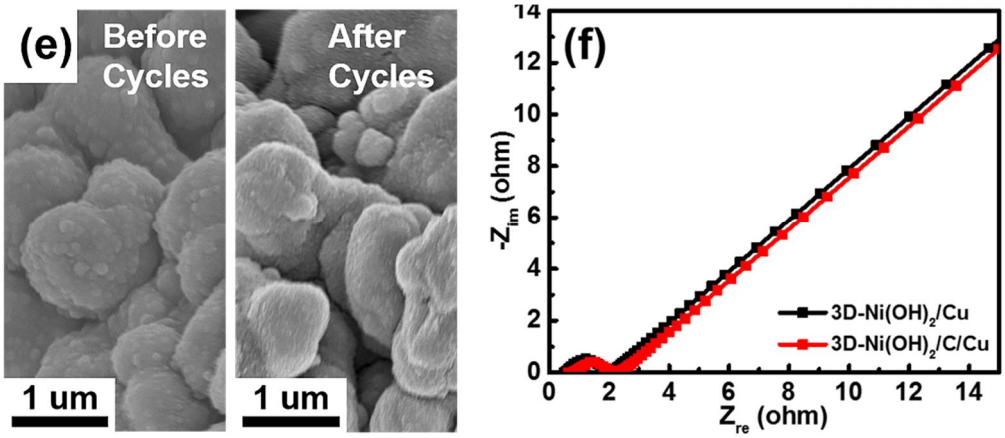

Figure 2. 17. Electrochemical characterization of the 3D-Ni(OH)$_2$/C/Cu electrode in a three-electrode system. (e) SEM image of the 3D-Ni(OH)$_2$/C/Cu before and after 10,000 cycles. (f) Electrochemical Impedance Spectroscopy (EIS) of the 3D-Ni(OH)$_2$/Cu and 3D-Ni(OH)$_2$/C/Cu electrodes.

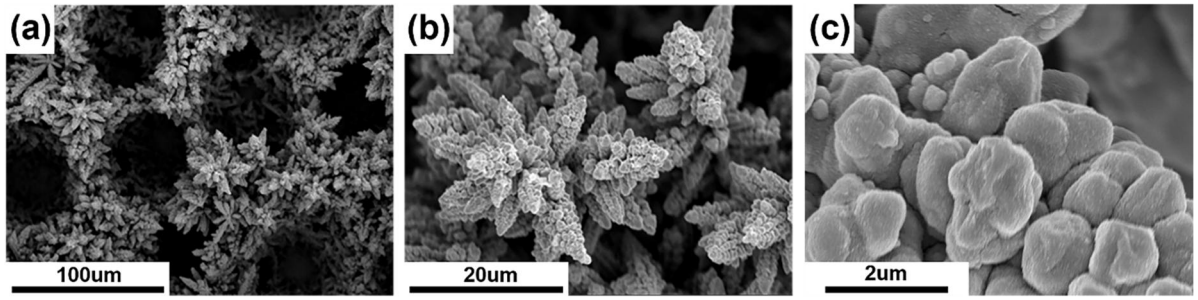

Figure 2. 18. SEM images of (a-c) show the 3D-Ni(OH)$_2$/C/Cu structure after 10000 cycles.

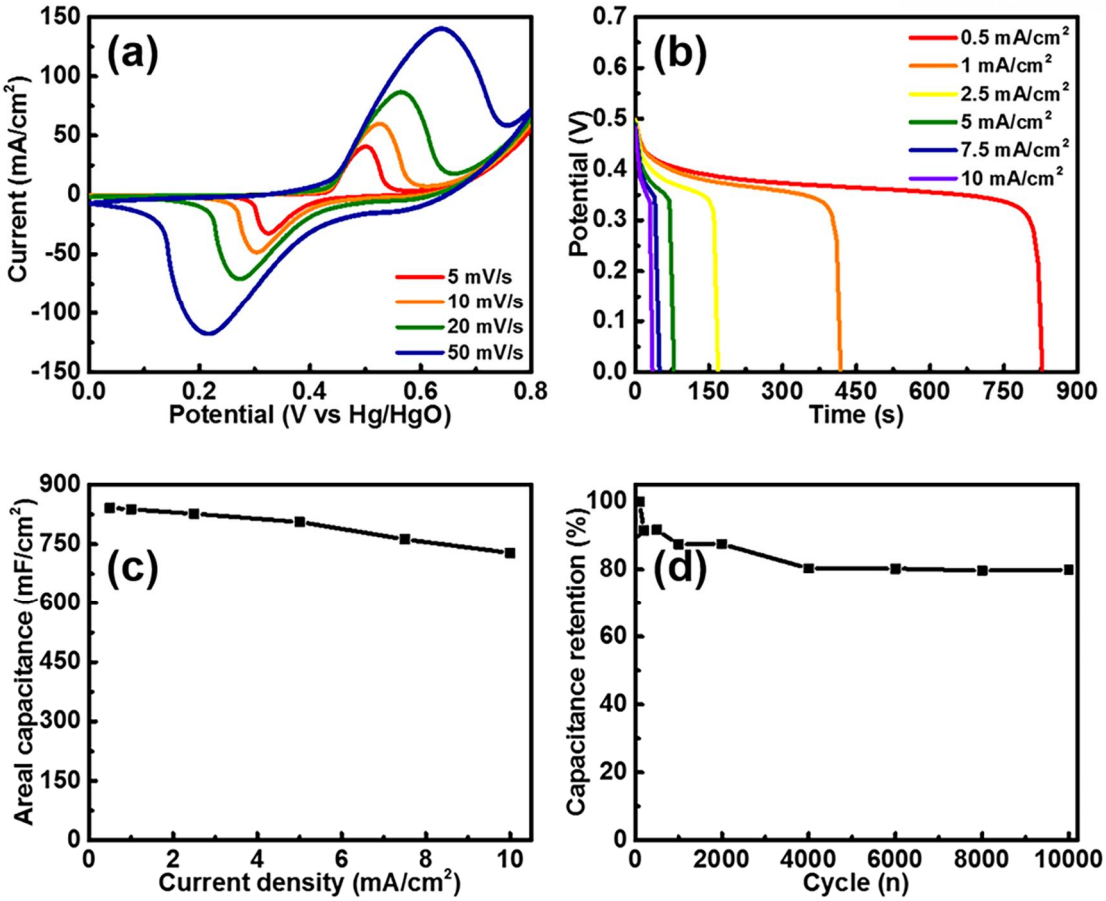

Figure 2. 19. Three-electrode electrochemical performance of the 3D-Ni(OH)$_2$/C/Cu composite in 1M KOH aqueous solution, for measuring areal capacitance. (a) CV curves of the electrode at different scan rates. (b) Discharge curves of the electrode at different current densities per area. (c) Gravimetric areal capacitance as a function of the current densities, and (d) cycling performance at 20A/g for 10000cycles.

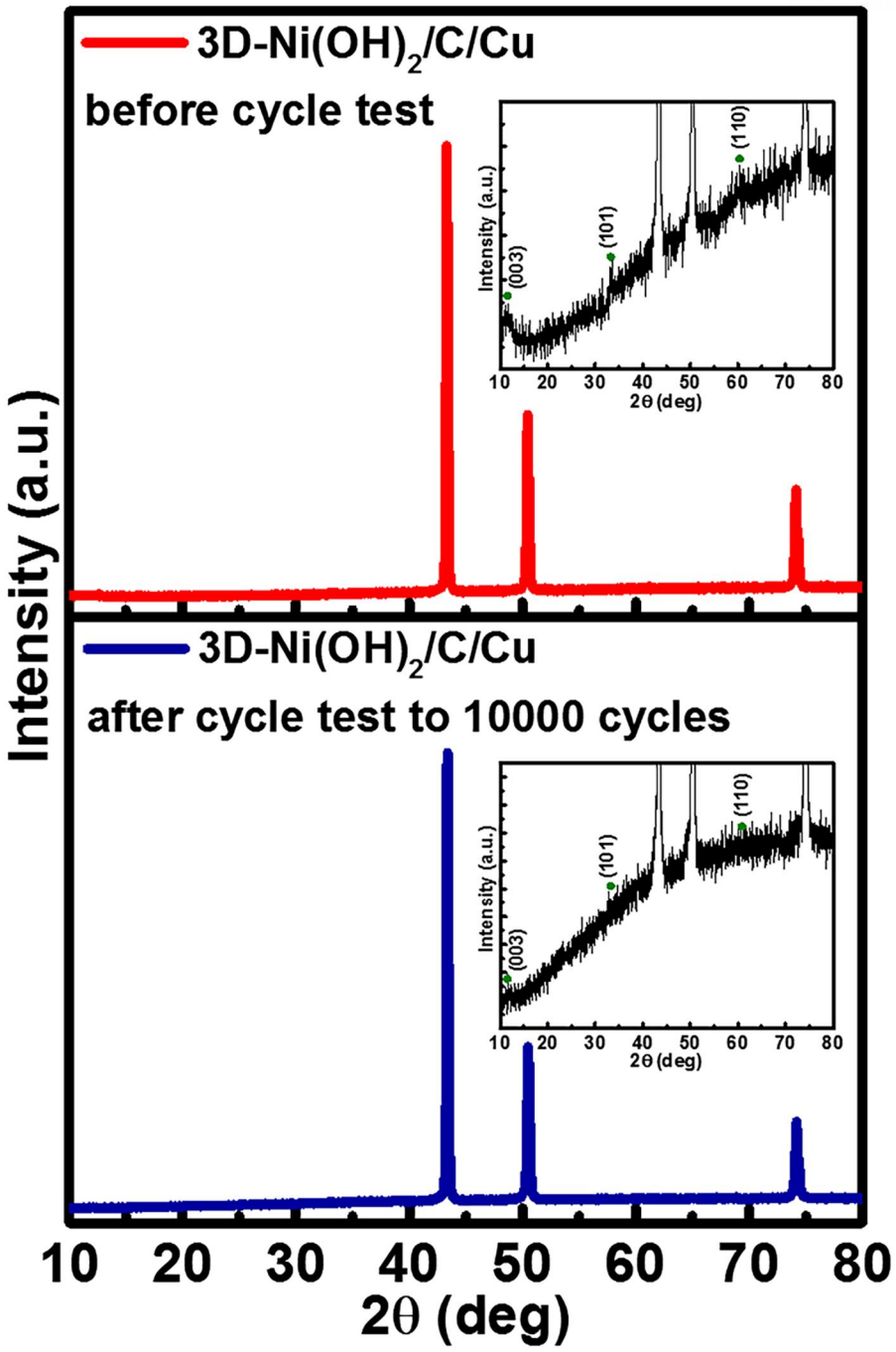

Figure 2. 20. Comparison of XRD patterns of the 3D-Ni(OH)$_2$/C/Cu before and after 10,000 cycles.

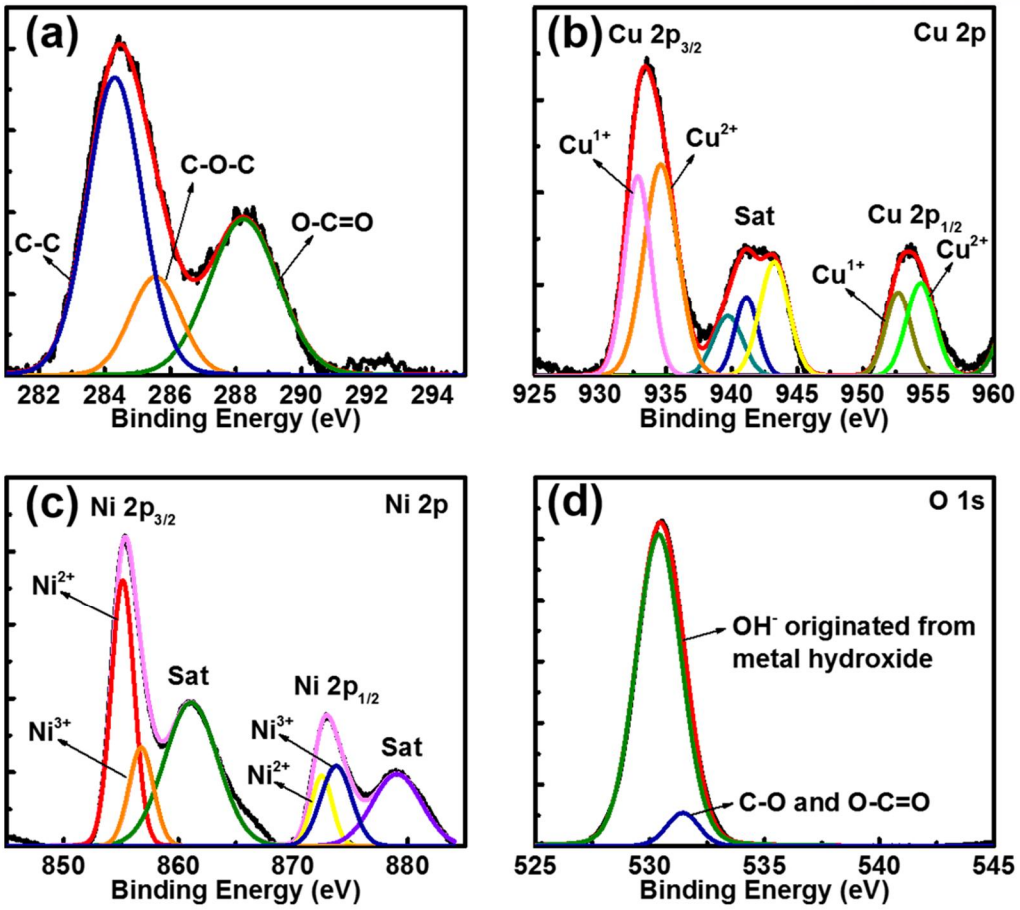

Figure. 2. 21. XPS spectra of (a)C 1s, (b) Cu 2p, (c) Ni 2p, and (d) O 1s for the 3D-$Ni(OH)_2$/C/Cu electrode after 10,000 cycles.

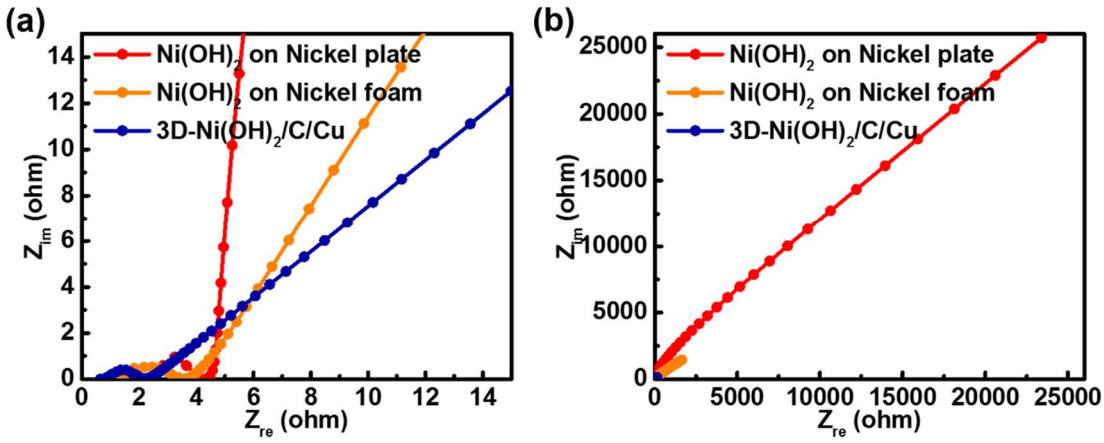

Figure 2. 22. Zoom-up range (a) and gauge span (b) of EIS of the as-prepared electrode (blue) and other references : $Ni(OH)_2$ on nickel film, and $Ni(OH)_2$ on nickel foam.

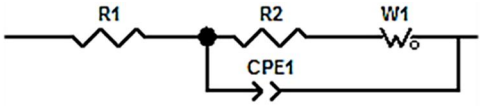

R1 (R_s) : Cell internal resistance
R2 (R_{ct}) : Charge transfer resistance
CPE 1 : Double layer capacitance
W1 : Warburg element

	3D-Ni(OH)$_2$/C/Cu	3D-Ni(OH)$_2$/Cu
R1 (R_s)	0.65Ω	0.48Ω
R2 (R_{ct})	0.65Ω	0.74Ω

Figure 2. 23. Model and values of Electrochemical Impedance Spectroscopy (EIS) of the 3D-Ni(OH)$_2$/Cu and 3D-Ni(OH)$_2$/C/Cu electrodes.

We further evaluated the electrochemical performance of the 3D-$Ni(OH)_2$/C/Cu electrode in an asymmetric two-electrode configuration in **Figure 2. 24**. Here, the asymmetric supercapacitor was assembled using 3D-Mn_3O_4/C/Cu, which is confirmed by XRD patterns as shown in **Figure 2. 25**, 3D-$Ni(OH)_2$/C/Cu, and a filter paper as the negative electrode, positive electrode, and separator, respectively, as shown in **Figure 2. 26**.[35] (The electrochemical performance of 3D-$Ni(OH)_2$/C/Cu//Activated carbon was measured first, as shown in **Figure 2. 27**). The comparative CV curves of the 3D-Mn_3O_4/C/Cu and 3D-Ni(OH)2/C/Cu at 50 mV/s scan rate are shown in **Figure 2. 24a**. The CV curves of the Mn_3O_4 within a voltage window of -0.8 V to 0 V exhibit a pair of redox peaks, which corresponds to the reversible reaction of Mn.[36]

As for the 3D-$Ni(OH)_2$/C/Cu electrode in the voltage window from 0 to 0.8 V, a pair of redox peaks are observed. Therefore, it is possible to conclude that the entire voltage window of the asymmetric supercapacitor can be extended up to 1.6 V due to the combination of the $Ni(OH)_2$ and Mn_3O_4 electrochemical performances.

A series of CV curves with different potential windows were measured to estimate the best operating potential of the asymmetric supercapacitor, as shown in **Figure 2. 24b**. When the operating potential was increased to 1.6 V, more faradic reactions occurred. When the operating potential was extended to 1.7 V, no obvious current increase was observed compared to the one with a potential window of 1.6 V. Since both the energy density and power density are highly dependent on the cell operating voltage, according to $E=CV^2/2$, 1.6 V was used as the cell potential to further investigate the electrochemical performance of the asymmetric supercapacitor.

Figure 2. 24c shows the CVs between 0 and 1.6 V at various scan rates from 10 to 100 mV/s in a 1 M KOH aqueous electrolyte. The galvanostatic charge/discharge plots needed to charge fully at different current densities with the potential window of 1.5 V are shown in **Figure 2. 24d**. The specific capacitance calculated based on the 3D-Mn_3O_4/C/Cu//3D-$Ni(OH)_2$/C/Cu electrodes reached 474.3 F/g per electrode at a current density of 1 A/g.

We also compared the energy density and maximum power density of the as-fabricated asymmetric device to those of other outstanding supercapacitors, as shown in the Ragone plot (**Figure 2. 24e**). The specific energy density of the 3D-$Ni(OH)_2$/C/Cu//3D-Mn_3O_4/C/Cu asymmetric supercapacitor reached 147.9 Wh/kg at 749.9 W/kg, and remained at 51.4 Wh/kg with the high power density of 37.0 kW/kg. The maximum energy density obtained for a 3D-$Ni(OH)_2$/C/Cu//3D-Mn_3O_4/C/Cu asymmetric supercapacitor with a cell voltage of 1.6 V was much higher than those of $Ni(OH)_2$/CNT-AC(50.6 Wh/kg),[37] $Ni(OH)_2$/porous graphene (77.8 Wh/kg),[38] ultrathin $Ni(OH)_2$ (68.75 Wh/kg),[39] $Ni(OH)_2$/CNT/PEDOT:PSS (58.5 Wh/kg),[40] and $Ni(OH)_2$/RGO (75 Wh/kg)[41] MnO_2/Ni (28.4 Wh/kg)[42],

amorphous $Ni(OH)_2$/3D-Ni (21.8 Wh/kg)[26], $Ni(OH)_2$/hollow 3D-Ni (23 Wh/kg)[43], and $Ni(OH)_2$/3D-Ni (78 Wh/kg)[44]. The capacitance retention of the asymmetric cell after 10,000 cycles of charge/discharge at a current density of 5 A/g was 64.9 %, which implies the asymmetric pseudocapacitor has relatively good stability (**Figure 2. 24f**). This indicates that the 3D-$Ni(OH)_2$/C/Cu electrode has low electrode resistance and a high charge-transfer rate between the electrolyte and the active materials.

The large capacitance, excellent rate capability, and remarkable long-term cycling stability of the 3D-$Ni(OH)_2$/C/Cu can be attributed to the following unique structural features. First, the ultrathin $Ni(OH)_2$ layer deposited on the carbon coated 3D-Cu, which has an abundant number of active sites, allows for a shorter electron transport path for the less conductive $Ni(OH)_2$ active materials. Second, the dendritic morphology of the 3D-Cu with its macroscale/microscale holes enhances the transport of ions in the liquid electrolyte between the electrodes, and shortens the transport length of ions in the electrolytes. Third, the carbon coating protects the copper structure without increasing contact resistance between the $Ni(OH)_2$ and 3D-Cu, and thus improves long-term stability and rate capability. Fourth, the direct contact and strong binding between the active materials and the 3D-C/Cu reduces the interfacial resistance that often occurs in the active material/binder based electrode.

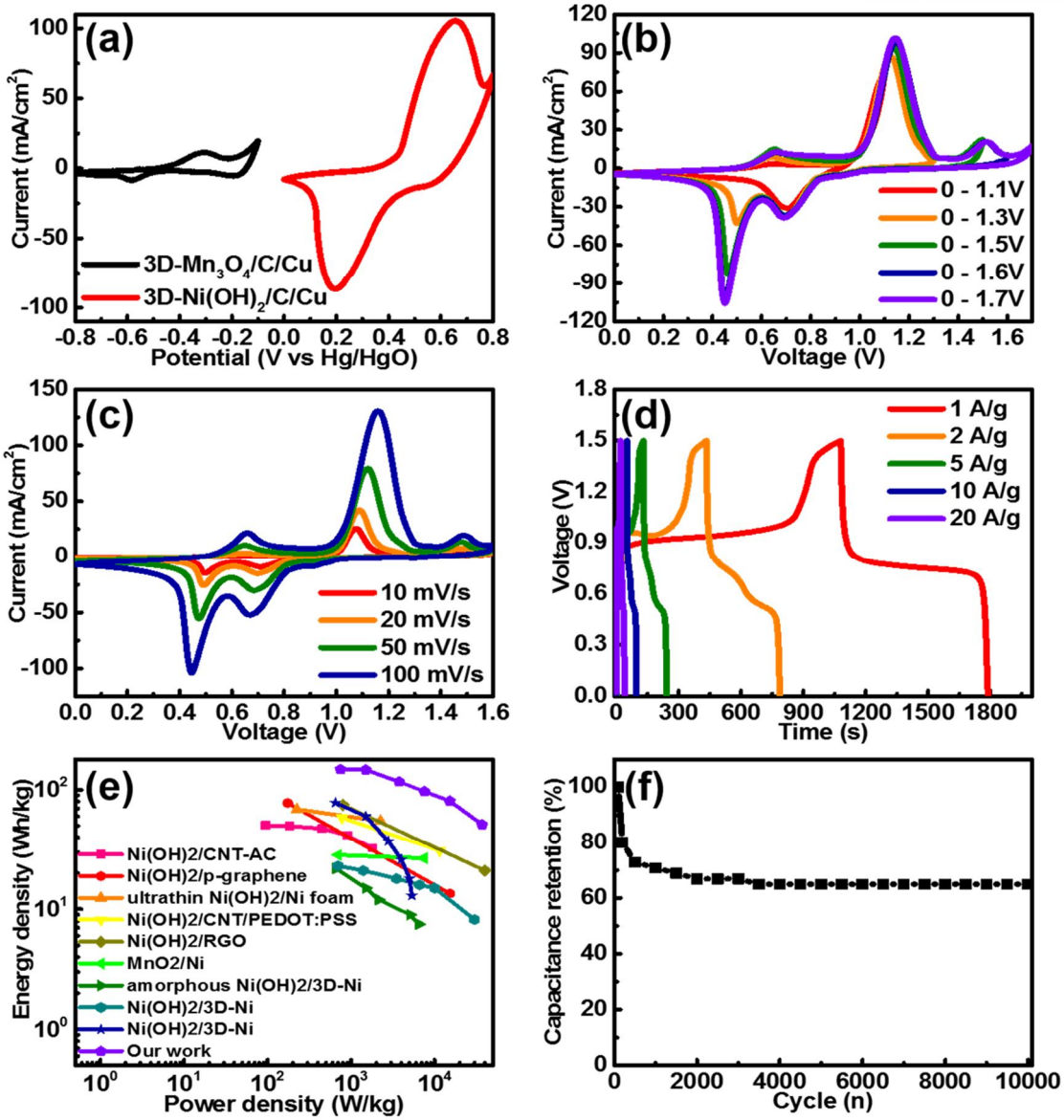

Figure 2. 24. (a) Comparative CV curves of the 3D-Mn_3O_4/C/Cu and 3D-$Ni(OH)_2$/C/Cu at 50 mV/s. (b) CV curves of the 3D-$Ni(OH)_2$/C/Cu//3D-Mn_3O_4/C/Cu asymmetric supercapacitor measured at different potential windows, at 100 mV/s. (c) CV curves of the 3D-$Ni(OH)_2$/C/Cu//3D-Mn_3O_4/C/Cu asymmetric supercapacitor measured at different scan rates of 10, 20, 50, 100 mV/s between 0 and 1.6V in 1 M KOH aqueous electrolyte. (d) Galvanostatic charge/discharge curves of the 3D-$Ni(OH)_2$/C/Cu//3D-Mn_3O_4/C/Cu asymmetric supercapacitor as a function of different current densities. (e) Ragone plot of 3D-$Ni(OH)_2$/C/Cu with other references and (f) Specific capacitance retention of 3D-$Ni(OH)_2$/C/Cu//3D-Mn_3O_4/C/Cu asymmetric supercapacitor as a function of cycle.

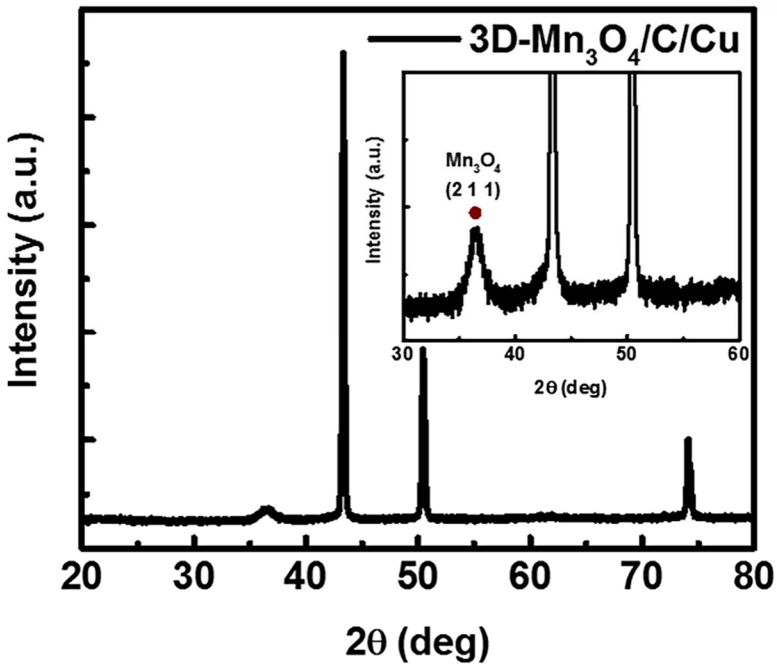

Figure 2. 25. XRD patterns of 3D-Mn_3O_4/C/Cu. The inset shows enlarged XRD patterns of 3D-Mn_3O_4/C/Cu.

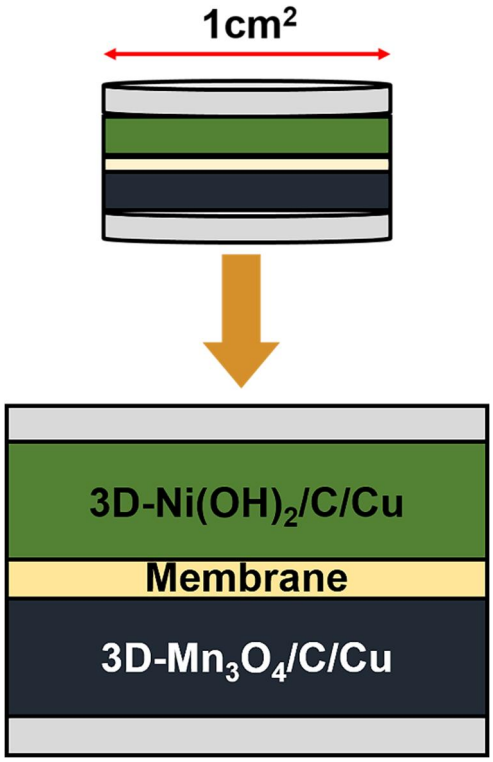

Figure 2. 26. Schematic illustration of the assembled 3D-$Ni(OH)_2$/C/Cu//3D-Mn_3O_4/C/Cu devices.

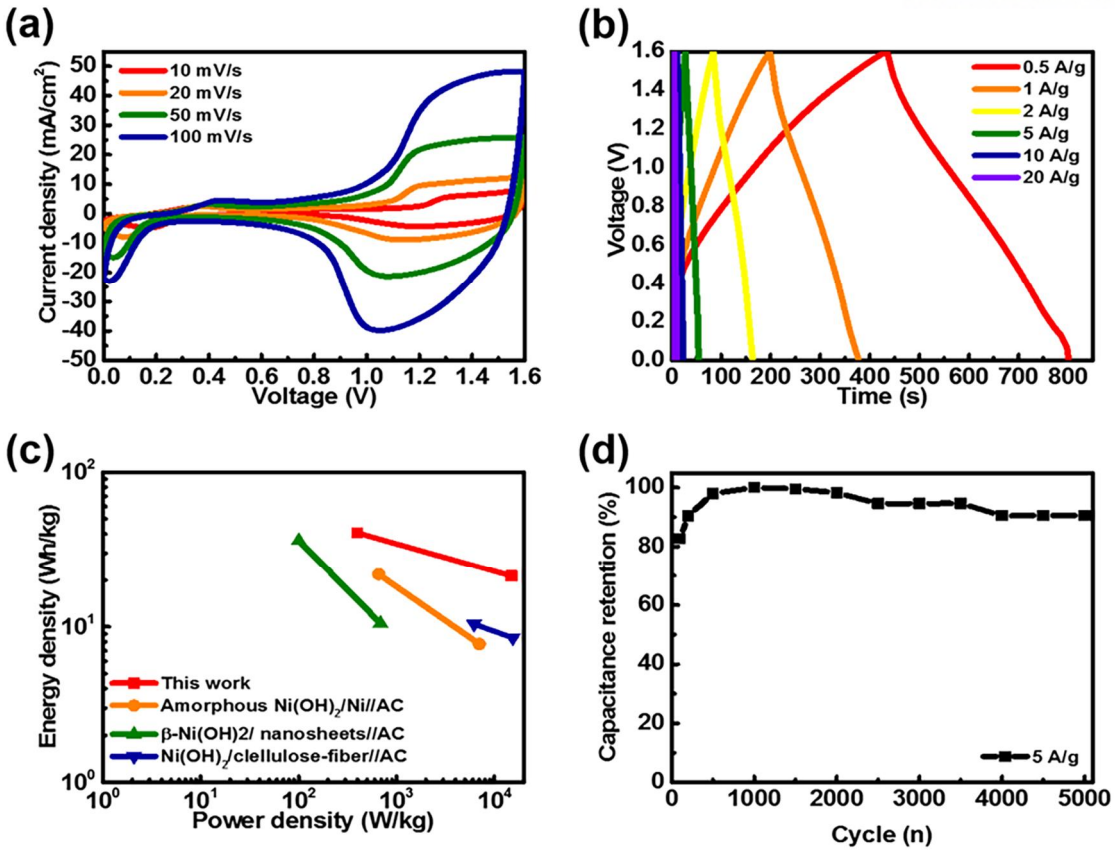

Figure 2. 27. (a) CV curves of the 3D-$Ni(OH)_2$/C/Cu//Activated carbon asymmetric supercapacitor measured at different scan rates of 10, 20, 30, 40, and 50 mV/s between 0 and 1.6V in 1M KOH aqueous electrolyte, (b) Galvanostatic charge/discharge curves of the 3D-$Ni(OH)_2$/C/Cu //Activated carbon asymmetric supercapacitor as a function of different current densities, (c) Ragone plot of the 3D-$Ni(OH)_2$/C/Cu with other references and (d) specific capacitance retention of the 3D-$Ni(OH)_2$/C/Cu //Activated carbon asymmetric supercapacitor as a function of cycle.

2. 4. Conclusion

In summary, an ultrathin $Ni(OH)_2$ layer was applied as an active material by utilizing dendritic porous 3D-Cu structures as ideal current collectors for a high performance supercapacitor. The 3D-C/Cu structure provides high conductivity, facilitating electron transport from the $Ni(OH)_2$ to the current collector, and the ultrathin $Ni(OH)_2$ layer also shortens the transport length of electrons. With meso-/micropores on their surface, the 3D-$Ni(OH)_2$/C/Cu materials provide favorable accessibility for ions. These characteristics have favorable synergetic effects which are beneficial for high-performance supercapacitor applications. The optimized 3D-$Ni(OH)_2$/C/Cu electrode realized an 1860 F/g specific capacitance at 1 A/g in a 1.0 M KOH aqueous solution. Furthermore, 86.3 % and 86.5 % of the original capacitance value were maintained at 50 A/g and after 10,000 cycles, respectively. Moreover, the electrode exhibited a maximum energy density of 147.9 Wh/kg and power density of 37.0 kW/kg. Our results suggest that 3D-C/Cu has great potential as a supporting current collector in various energy storage devices.

2. 5. References

1. J. Yan, Q. Wang, T. Wei and Z. Fan, Recent Advances in Design and Fabrication of Electrochemical Supercapacitors with High Energy Densities, Adv. Energy Mater., 2014, **4**(4), 1300816.

2. G. Wang, L. Zhang and J. Zhang, A review of electrode materials for electrochemical supercapacitors, Chem. Soc. Rev., 2012, **41**(2), 797-828.

3. Y. G. Patrice Simon and B. Dunn, Where Do Batteries End and Supercapacitors Begin?, Science, 2014, **343**, 1210-1211.

4. S. Mao, G. Lu and J. Chen, Three-dimensional graphene-based composites for energy applications, Nanoscale, 2015, **7**(16), 6924-6943.

5. Z. Wu, L. Li, J.–M. Yan and X.-B. Zhang, Materials Design and System Construction for Conventional and New-Concept Supercapacitors, Adv. Sci., 2017, 1600382.

6. Q. Qunting, Z. Peng, W. Bin, C. Yuhui, T. Shu, W. Yuping and H. Rudolf, Electorchemical Performance of MnO2 Nanorods in Neutral Aqueous Electrolytes as a Cathode for Asymmetric Supercapacitors, J. Phys. Chem. C, 2009, **113**, 14020-14027.

7. X. Xie, C. Zhang, M. B. Wu, Y. Tao, W. Lv and Q. H. Yang, Porous MnO2 for use in a high performance supercapacitor: replication of a 3D graphene network as a reactive template, Chem. Commun., 2013, **49**(94), 11092-11094.

8. S. K. Meher and G. R. Rao, Ultralayered Co3O4 for High-Performance Supercapacitor Applications, J. Phys. Chem. C, 2011, **115**(31), 15646-15654.

9. S. I. Kim, J. S. Lee, H. J. Ahn, H. K. Song and J. H. Jang, Facile route to an efficient NiO supercapacitor with a three-dimensional nanonetwork morphology, ACS Appl. Mater. Interfaces, 2013, **5**(5), 1596-1603.

10. S. I. Kim, P. Thiyagarajan and J. H. Jang, Great improvement in pseudocapacitor properties of nickel hydroxide via simple gold deposition, Nanoscale, 2014, **6**(20), 11646-11652.

11. S.-I. Kim, K.-N. Kang, S.-W. Kim and J.-H. Jang, A one-step practical strategy to enhance overall supercapacitor performance, RSC Adv., 2014 **4**(103), 59310-59314.

12. C.-C. Hu, K.-H. Chang, M.-C. Lin and Y.-T. Wu, Design and Tailoring of the Nanotubular Arrayed Architecture of Hydrous RuO2 for Next Generation Supercapacitors, Nano Lett., 2006, **6**(12), 2690-2695.

13. A. Ramadoss, K.-N. Kang, H.-J. Ahn, S.-I. Kim, S.-T. Ryu and J.-H. Jang, Realization of high performance flexible wire supercapacitors based on 3-dimensional NiCo2O4/Ni fibers, J. Mater. Chem. A, 2016, **4**(13), 4718-4727.

14. Z. Yu, L. Tetard, L. Zhai and J. Thomas, Supercapacitor electrode materials: nanostructures from 0 to 3 dimensions, Energy Environ. Sci., 2015, **8**(3), 702-730.

15. A. Pramanik, S. Maiti and S. Mahanty, Reduced graphene oxide anchored Cu(OH)2 as a high performance electrochemical supercapacitor, Dalton Trans, 2015, **44**(33), 14604-14612.

16. M. R. Lukatskaya, B. Dunn and Y. Gogotsi, Multidimensional materials and device architectures for future hybrid energy storage, Nat. Commun., 2016, **7**, 12647.

17. Q. Ke and J. Wang, Graphene-based materials for supercapacitor electrodes – A review, Journal of Materiomics, 2016, **2**(1), 37-54.

18. M. F. El-kady, M. Ihns, M. Li, J. Hwang, M. F. Mousavi, L. Chaney, A. T. Lech and R. B. Kaner, Engineering three-dimensional hybrid supercapacitors and microsupercapacitors for high-performance integrated energy storage, Proc. Natl. Acad. Sci. U. S. A., 2015, **112**(14), 4233-4238.

19. S.-I. Kim, S.-W. Kim, K. Jung, J.-B. Kim and J.-H. Jang, Ideal nanoporous gold based supercapacitors with theoretical capacitance and high energy/power density, Nano Energy, 2016, **24**, 17-24.

20. X. H. Xia, J. P. Tu, Y. Q. Zhang, y. J. Mai, X. L. Wang, C. D. Gu and X. B. Zhao, Three-dimensional Porous Nano-Ni/Co(OH)2 nanoflake Composite Film: A Pseudocapacitive Material with Superior Performance, J. Phys. Chem. C, 2011, **115**(45), 22662-22668.

21. W. Wang, W. Wang, M. Wang and X. Guo, Facile in situ synthesis of hierarchical porous Ni/Ni(OH)2 hybrid sponges with excellent electrochemical energy-storage performances for supercapacitors, Chem. –Asian J., 2014, **9**(9), 2590-2596.

22. H. Jiang, Y. Guo, T. Wang, P.-L. Zhu, S. Yu, Y. Yu, X.-Z. Fu, R. Sun and C.-P. Wong, Electrochemical fabrication of Ni(OH)2/Ni 3D porous composite films as integrated capacitive electrodes, RSC Adv., 2015, **5**(17), 12931-12936.

23. I. C. Chang, T.-T. Chen, M.-H. Yang, H.-T. Chiu and C.-Y. Lee, Self-powered electrochemical deposition of Cu@Ni(OH)2 nanobelts for high performance pseudocapacitors, J. Mater. Chem. A, 2014, **2**(27), 10370.

24. Y. Liu, A. Wiek, V. Dzhagan and R. Holze, Improved Electrochemical Behavior of Amorphous

Carbon-Coated Copper/CNT composites as Negative Electrode Material and Their Energy Storage Mechanism, J. Electorchem. Soc., 2016, **163**(7), A1247-A1253.

25. J. Liu, M. Chen, L. Zhang, J. Jiang, J. Yan, Y. Huang, J. Lin, H. J. Fan and Z. X. Shen, A flexible alkaline rechargeable Ni/Fe battery based on graphene foam/carbon nanotubes hybrid film, Nano Lett., 2014, **14**(12), 7180-7187.

26. Y.-Z. Su, K. Xiao, N. Li, Z.-Q. Liu and S.-Z. Qiao, Amorphous Ni(OH)2@ three-dimensional Ni core-shell nanostructures for high capacitance pseudocapacitors and asymmetric supercapacitors, J. Mater. Chem. A, 2014, **2**(34), 13845.

27. J. Ji, L. L. Zhang, H. Ji, Y. Li, X. Zhao, X. Bai, X. Fan, F. Zhang and R. S. Ruoff, Nanoporous Ni(OH)2 Thin Film on 3D Ultrathin-Graphite Foam for Asymmetric Supercapacitor, ACS Nano, 2013, **7**(7), 6237-6243.

28. H. B. Li, M. H. Yu, F. X. Wang, P. Liu, Y. Liang, J. Xiao, C. X. Wang, Y. X. Tong and G. W. Yang, Amorphous nickel hydroxide nanospheres with ultrahigh capacitance and energy density as electrochemical pseudocapacitor materials, Nat. Commun., 2013, **4**, 1894.

29. H. Wang, H. S. Casalongue, Y. Liang and H. Dai, Ni(OH)2 Nanoplates Grown on Graphene as Advanced Electrochemical Pseudocapacitor Materials, J. Am. Chem. Soc., 2010, **132**, 7472-7477.

30. G. W. Yang, C. L. Xu and H. L. Li, Electrodeposited nickel hydroxide on nickel foam with ultrahigh capacitance, Chem. Commun., 2008, 6537-6539.

31. X. Xiong, D. Ding, D. Chen, G. Waller, Y. Bu, Z. Wang and M. Liu, Three-dimensional ultrathin Ni(OH)2 nanosheets grown on nickel foam for high-performance supercapacitors, Nano Energy, 2015, **11**, 154-161.

32. K.-H. Young, L. Wang, S. Yan, X. Liao, T. Meng, H. Shen and W. C. Mays, Fabrications of High-capacity Alpha-Ni(OH)2, Batteries, 2017, **3**, 6.

33. X. Wan, g. P. J. S., A.-C. Millan, P. V. Parkhutik and S. A. Gamboa, Electrochemical study of nanostructured multiphase nickel hydroxide, J. New Mater. Electrochem. Syst., 2005, **8**, 101-108.

34. S. Ede, S. Anantharaj, K. T. Kumaran, Soumyaranjan Mishra and Subrata Kundu, One step synthesis of Ni/Ni(OH)2 nanosheets (NSs) and their application in asymmetric supercapacitors, RSC Adv., 2017.

35. M. Mandal, D. Ghosh, K. Chattopadhyay, C. K. Das and A. Novel Asymmetric, Supercapacitor Designed with Mn3O4@Multi-wall Carbon Nanotube Nanocomposite and Reduced Graphene Oxide Electrodes, J. Electron. Mater., 2016, **45**(7), 3491-3500.

36. J. X. Feng, S. H. Ye, X. F. Lu, Y. X. Tong and G. R. Li, Asymmetric Paper Supercapacitor Based on Amorphous Porous Mn3O4 Negative Electrode and Ni(OH)2 Positive Electrode: A Novel and High-Performance Flexible Electrochemical Energy Storage Device, ACS Appl. Mater. Interfaces, 2015, **7**(21), 11444-11451.

37. Z. Tang, C.-h. Tang and H. Gong, A High, Energy Density Asymmetric Supercapacitor from Nano-architectured Ni(OH)2/Carbon Nanotube Electrodes, Adv. Funct. Mater., 2012, **22**(6), 1272-1278.

38. J. Yan, Z. Fan, W. Sun, Ning, T. Wei, Q. Zhang, R. Zhang, L. Zhi and F. Wei, Advanced Asymmetric Supercapacitors Based on Ni(OH)2/Graphene and Porous Graphene Electrodes with High Energy Density, Adv. Funct. Mater., 2012, **22**(12), 2632-2641.

39. X. Hu, S. Liu, C. Li, J. Huang, J. Luv, P. Xu, J. Liu and X. Z. You, Facile and environmentally friendly synthesis of ultrathin nickel hydroxide nanosheets with excellent supercapacitor performances, Nanoscale, 2016, 8(23), 11797-11802.

40. W. Jiang, D. Yu, Q. Zhang, K. Goh, L. Wei, Y. Yong, R. Jiang, J. Wei and Y. Chen, Ternary Hybrids of Amorphous Nickel Hydroxide-Carbon Nanotube-Conducting Polymer for Supercapacitors with High Energy Density, Excellent Rate Capability, and Long Cycle Life, Adv. Funct. Mater., 2015, **25**(7), 1063-1073.

41. Y. Liu, R. Wang and X. Yan, Synergistic Effect between ultra-small Nickel Hydroxide Nanoparticles and Reduced Graphene Oxide sheets for the Application in High-Performance Asymmetric Supercapacitor, Sci. Rep., 2015, **5**, 11095.

42. D. Liu, Q. Wang, L. Qiao, F. Li, D. Wang, Z. Yang and D. He, Preparation of nano-networks of MnO2 shell/Ni current collector core for high-performance supercapacitor electrodes, J. Mater. Chem., 2012, **22**.

43. S.-W. Kim, I.-H. Kim, S.-I. Kim and J.-H. Jang, Nickel Hydroxide Supercapacitor with a Theoretical Capacitance and High Rate Capability Based on Hollow Dendritic 3D-Nickel Current Collectors, Chem. –Asian J., 2017, **12**, 1291-1296.

44. S.-I. Kim, J.-H. K., S.-W. Kim and J.-H. Jang, A new approach to high-performance flexible supercapacitors: Mesoporous three-dimensional Ni-electrodes, Nano Energy, 2017, **39**.

Chapter 3. Flexible wire-shaped supercapacitors with ultrahigh energy density as substitutes for batteries

3. 1. Introduction

In recent years, smart wearable electronics have drawn significant attention for prospective applications in military garment devices, communications, sportswear, and wireless keys.[1-5] In line with this, there is intense demand for reliable power sources and high performance together with flexible, light-weight, thin, miniaturized, implantable, and safe energy conversion and storage systems.[6-10] Accordingly, many research groups are focusing on developing flexible/wearable energy storage systems with the aforementioned features as well as multi-functionality, versatile shape, and aesthetic design to address the energy supply problem of wearable devices. Supercapacitors are considered one of the most important energy storage devices, and they have garnered a great deal of attention for wearable electronic devices due to their features of high power delivery ability, fast charge/discharge rates, long cycle life, safety, low environment impact, and ease of manufacturing.[11-15]

In the past few years, much progress has been made toward the construction of versatile high-performance supercapacitors with high power and energy density, rate capability, flexibility and stability using various electroactive materials deposited on flexible substrates (plastics, paper, textile, metal sheets, and wires) to meet the demands of embryonic advanced wearable electronics.[16-22] However, the flexible weighty and large volume current collectors increase the total volume of the devices greatly, and further integration into wearable devices and flexible energy storage devices such as smart Google glasses, watches, and implantable devices with small volume limits their present energy storage capacity.[23-24]

To practically apply flexible energy storage components, high volumetric capacitance and excellent energy density are important factors. However, a highly compact electrode structure is generally expected to hinder ion accessibility to the electrode surface. Indeed, it has been widely reported that restricted ion transport, together with limited faradic charge transfer processes in compact electrodes, is a major contributor to the reduced capacitance and poor rate capability of pseudocapacitors. Therefore, to ensure the exposure of electrodes to electrolytes for high performance wearable supercapacitors, it is critical to synthesize nanostructured pseudocapacitive materials onto flexible substrates. Taking this into account, it is important to consider the balance between volumetric/areal capacitance, which is related to space saving, and high energy density, which is related to practical usage, when fabricating pseudocapacitive materials for supercapacitors in smart wearable electronic devices.

Among the various flexible substrates, metal wire is an ideal platform to construct wire/cable-type

supercapacitors due to its intrinsic flexibility, mechanical strength, light weight, and miniature nature. Even though wire/cable-type supercapacitors have attracted much attention, the obtained electrochemical performance of the devices is low due to the low specific surface area and limited accessibility of the electroactive materials.[25-29] In order to improve the electrochemical performance of the devices, fabricating electrodes with increased specific surface area, appropriate pore size distribution (total electrolyte-accessible surface area of the electrodes), higher electrical conductivity, and enlarged voltage window is essential.[30-31]

Herein, we demonstrate the fabrication of a flexible wire-type hybrid supercapacitor (with a smart "wire band-type" function for smart watches and smart Google glasses) using three dimensional (3D)-NiCo LDH/Ni nanostructures as the positive electrode, 3D-Mn_3O_4@Ni wire as the negative electrode, and PVA-KOH gel electrolyte as the separator. The 3D-Ni wire is free to bend, and acts as a binder and conductive additive-free current collector while also providing additional faradaic energy storage. The as-prepared 3D-Ni wire electrode holds a structure comprising abundant porous dendritic walls formed by nanoparticles for easy access of electrolyte ions and highly conductive networks for fast electron transfer, and provides numerous electroactive sites for improved charge storage. Thus, the as-fabricated hybrid supercapacitors based on 3D-NiCo-LDH@Ni//3D-Mn_3O_4@Ni wire delivered excellent electrochemical capacitive properties and maintained the inherent characteristics of flexibility with outstanding electrochemical performance reliability while bending. The maximum energy density of the asymmetric supercapacitor can be further calculated to be 153.3 Wh/kg at a power density of 2238 W/kg based on the total mass of active materials. Further, the feasibility of the as-fabricated hybrid device was tested in real time conditions by driving LED lights, LCD smart devices, a thermometer, and a wearable watch. These results demonstrate that the proposed wire band-like hybrid supercapacitor affords remarkable potential for smart wearable electronics including smart watches, Google glasses, and implantable devices having energy delivering capacity and flexibility.

3. 2. Experimental details

3. 2. 1. Materials

The 0.5 mm diameter nickel (Ni) wire was obtained from Nilaco, Japan. The nickel chloride ($NiCl_4$), ammonium chloride (NH_4Cl), nickel nitrate ($Ni(NO_3)_2.6H_2O$), cobalt nitrate ($Co(NO_3)_2.6H_2O$) and hexamethylene tetramine (HMTA) and polyvinyl alcohol (PVA) were purchased from Sigma Aldrich, Korea. Potassium hydroxide (KOH) was purchased from Samchun Pure Chemical Co. Ltd. Korea. All the chemicals used in our experiments were of analytical grade purity and used without any further purification. Ultrapure (De-ionized) water was used for all experiments.

3. 2. 2. Preparation of 3D-Ni film on Ni-wire

Nickel wire (0.5 mm, Nilaco, Japan) was used as a substrate. The three dimensional porous nickel film (3D-Ni) on Ni-wire was deposited using electrodeposition with a hydrogen bubble template method [1, 2]. The Ni-wire and platinum mesh were used as the cathode and anode, respectively, for constructing the 3D-Ni film, keeping the distance between the two electrodes at 1 cm. The 3D porous Ni film was electrodeposited at a constant current of 2.5 A using a regulated DC power supply with the electrolyte containing 0.1 M $NiCl_2$ and 2 M NH_4Cl. After the deposition, the 3D porous Ni film was rinsed several times in DI water and dried at 60 °C for 12 h in a hot air oven.

3. 2. 3. Preparation of 3D NiCo-LDH/Ni nanosheet arrays

The bimetallic double hydroxide nanostructure was prepared by a hydrothermal method onto the 3D porous Ni film/Ni wire. First, nickel nitrate ($Ni(NO_3)_2.6H_2O$), cobalt nitrate ($Co(NO_3)_2.6H_2O$), and hexamethylene tetramine (HMTA) were dissolved in 20 mL of ethanol and 20 mL of deionized water at room temperature to form a pink solution. Subsequently, the obtained solution and 3D-Ni film on Ni wire were transferred into a 100 ml bottle with a blue cap and heated to 80 °C in an oil bath for 8 h to obtain 3D NiCo-LDH/Ni nanosheets. After being cooled to room temperature, the obtained samples were washed using deionized water and ethanol several times to remove by-products on the surface and dried at 60°C for 12 hr. The mass loadings of 3D NiCo-DH/Ni were calculated to be 0.2 mg.

3. 2. 4. Preparation of 3D-Mn_3O_4/Ni nanosheet arrays

A Mn3O4 nanosheet array was prepared by the electrodeposition method onto the 3D porous Ni film/Ni wire. First, 100 mM manganese acetate tetrahydrate ($Mn(CH_3COO)_2{\cdot}4H_2O$) and 100 mM sodium sulfate anhydrate (Na_2SO_4) were dissolved in 100 mL of deionized water at room temperature. Continuously, the 3D-Ni film was electrodeposited on the Ni wire at 5 mA for 5 mins at 25 ^oC. The deposited electrodes were carefully washed using deionized water and heat treatment was performed at

200 ^{o}C for 3hr. The mass loading of 3D-Mn3O4/Ni was calculated to be 0.6mg.

3. 2. 5. Fabrication of flexible all-solid-state asymmetric wire supercapacitors

For a flexible solid-state asymmetric supercapacitor, a PVA/KOH gel electrolyte was first prepared by the following method. First, 10 g of PVA was dissolved in 100 ml of deionized water (DI) at 95 °C under stirring until the solution became clear. Then, 5.6 g of KOH was added to the above solution, which was vigorously stirred at 95 °C until a clear gel was formed. Prior to assembling the asymmetric wire device, the fabricated 3D-NiCo-LDH/Ni and 3D-Mn_3O_4/Ni electrodes were immersed in a PVA/KOH gel electrolyte for 5 min and then the gel electrolyte was allowed to solidify at room temperature. The two electrodes were then closely and parallel assembled onto a PET substrate with a separation distance of ~1mm to form an all-solid state flexible asymmetric wire supercapacitor and again dried at room temperature overnight to remove excess water in the electrolyte. After the PVA/KOH gel electrolyte solidified, the solid state asymmetric wire supercapacitor was sealed with tape to prevent absorption of moisture.

3. 2. 6. Materials characterization:

The morphologies and elemental composition of the as-prepared samples were characterized using a Field Emission scanning electron microscopy (FE-SEM, Hitachi, S-4800) equipped with energy dispersive X-ray spectroscopy (EDS). The X-ray diffraction (XRD) patterns of the samples were examined with the 2θ-angle from 5-80° on a Rigaku D/max 2550 diffractometer, using Cu (Kα) radiation (λ = 1.5406 Å). Raman spectra were recorded with a Raman spectroscopy (WITec). The compositional analysis of the samples were analyzed by X-ray photoelectron spectroscopy (XPS, K-alpha; Escalab 250Xi model, Thermo Fisher, UK).

3. 2. 7. Electrochemical characterization

All electrochemical tests including cyclic voltammetry, galvanostatic charge/discharge, and electrochemical impedance spectroscopy (EIS) were performed using a three-electrode system in 2 M KOH with electrochemical workstations (VMP3 biologic electrochemical workstation and VersaSTAT3 (Princeton Applied Research)). The as-prepared samples, platinum mesh, and Hg/HgO were used as working, counter, and reference electrodes, respectively. Further, an asymmetric solid state wire supercapacitor using the 3D NiCo-DH/Ni electrode (positive) and Mn_3O_4 (negative electrode) were tested in a two-electrode configuration using PVA-KOH gel electrolyte. The optimum mass ratio of positive electrode to negative electrode was calculated by the following equation:

$$m_+/m_- = V_- C_-/V_+ C_+ \quad (1)$$

where m is the mass of electroactive materials, V is the potential window and C represents the specific capacitance, respectively.

The gravimetric, volumetric, areal and length capacitance of 3D-NiCo LDH/Ni nanostructures electrode materials were estimated from the cyclic voltammetry and galvanostatic charge/discharge profiles using the following equations:

Cyclic Voltammetry:

Capacitance: $$C = \frac{\int idV}{2S\Delta V} \quad \text{..... (2)}$$

Galvanostatic charge/discharge:

Capacitance: $$C = \frac{I \times \Delta t}{\Delta V} \quad \text{..... (3)}$$

Gravimetric capacitance: $$C_g = \frac{C}{m} \quad \text{..... (4)}$$

Volumetric capacitance: $$C_v = \frac{C}{v} \quad \text{..... (5)}$$

Areal capacitance: $$C_a = \frac{C}{a} \quad \text{..... (6)}$$

Length capacitance: $$C_l = \frac{C}{l} \quad \text{..... (7)}$$

Where C is the capacitance (F), C_g is the gravimetric capacitance (F g^{-1}), C_v is the volumetric capacitance (F cm^{-3}), C_a is the areal capacitance (F cm^{-2}), C_l is the length capacitance (F cm^{-1}), S is the sweep rate (mV s^{-1}), $\triangle V$ is the potential window (V), I is the discharge current (A), $\triangle t$ is the discharge time (s), v is the volume of the electrode material (cm^3), m is the mass of the active material (g), A is the area of the electroactive material (cm^2), l is the length of the electrode material and $\int idV$ is the integral area of the CV curve (A).

3. 3. Results and discussion

The fabrication procedure of the 3D-NiCo LDH/Ni nanostructure is schematically presented in **Figure 3. 1**. First, 3D-Ni porous films were deposited onto Ni wire substrates via electrodeposition using a hydrogen bubble template method. The highly porous, conductive, and large surface area 3D-Ni metal is beneficial for the growth of various nanostructures in small areas and therefore efficiently serves as a cost-effective and flexible electrode for pseudocapacitors. NiCo LDH nanostructures were then grown onto the as-obtained 3D-Ni/Ni porous wire through a hydrothermal method from which 3D-NiCo LDH/Ni was formed. The as-prepared 3D-NiCo LDH/Ni is highly rough and porous, which is more favorable for abundant electrochemical reactions with electrolyte ions. The morphological evolution of the 3D-NiCo LDH/Ni on Ni wire was investigated by FE-SEM (**Figures 3. 1b-g**). It can be seen that the 3D-Ni metal wire was homogeneously covered by NiCo LDH nanosheets/flakes with a thickness of 20-30 nm, forming a 3D highly porous dendritic flower-like structure with microspheres (~2 μm), after the hydrothermal process. The interconnected arrangement of the NiCo LDH nanosheets grown on the 3D-Ni/Ni wire provides excellent accessibility for electrolyte ions over the entire surface of the electrode materials and also lower interfacial resistance, which is expected to enhance electrochemical performance. A cross sectional view of the 3D-NiCo LDH/Ni nanostructure electrode with a thickness of ~35 μm at different magnifications is shown in **Figures 3. 2a-d**. It is observed that nanoparticles were interconnected and arranged normal to the substrate to form a porous dendritic nanowall structure, leaving numerous open spaces and electroactive surface sites for the enhanced charge storage properties. The EDS spectrum and elemental mapping images of NiCo LDH/3D-Ni nanostructures are shown in Figures S1e-h. The EDS spectrum with an inset FE-SEM image (**Figure 3. 2e**) exhibits Ni, Co, and O elemental peaks, which confirms the successful formation of NiCo LDH/3D-Ni nanostructures. From the elemental EDS mapping images in **Figures 3. 2f-h**, it was confirmed that both Ni and Co elements were uniformly distributed throughout the surface, indicating the homogenous deposition of NiCo LDHs over the entire surface of the 3D-Ni metal wire current collector.

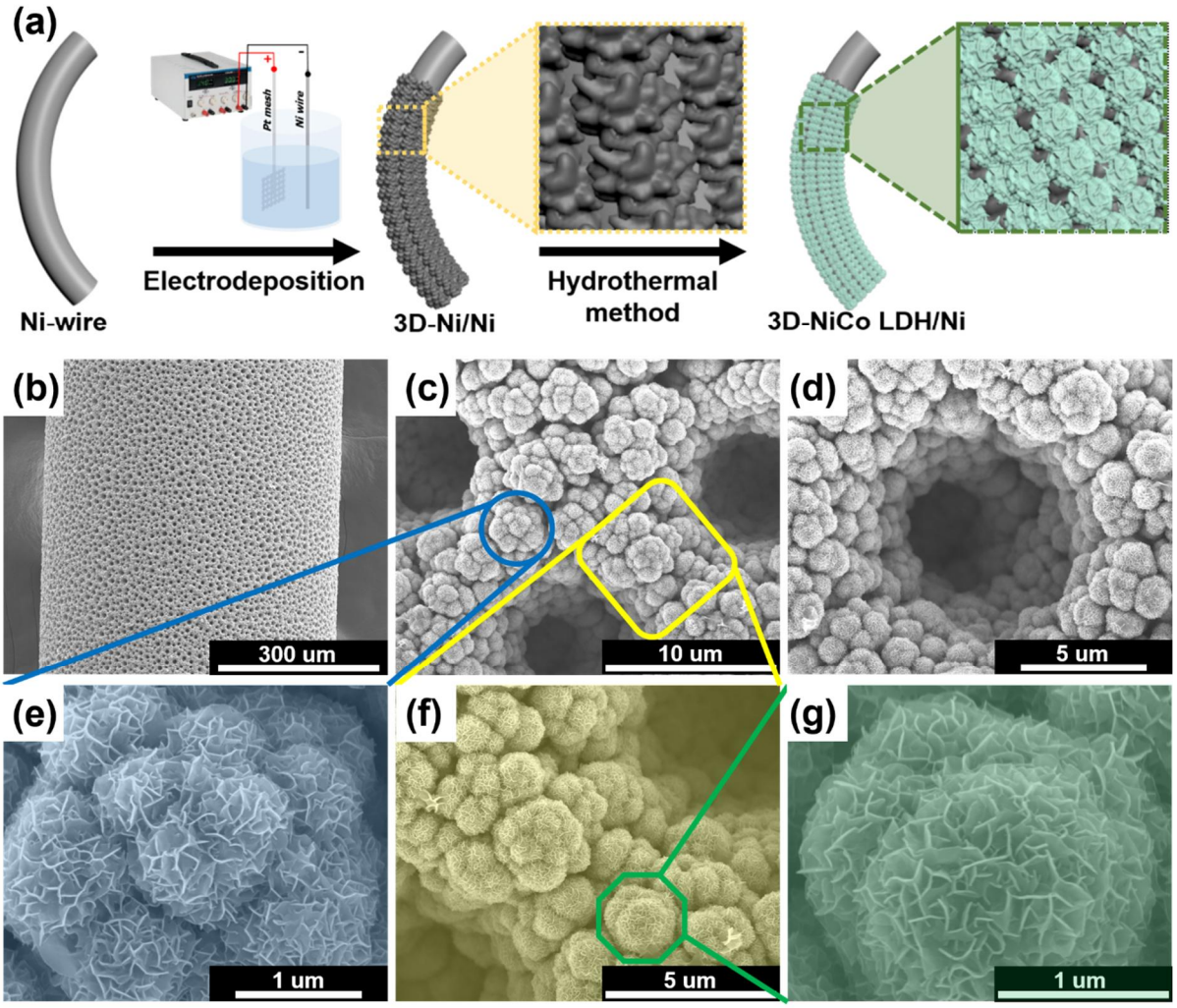

Figure 3. 1. (a) Schematic representation of the fabrication of the 3D-NiCo LDH/Ni electrode and (b-g) FE-SEM images of 3D-NiCo LDH/Ni nanostructures at different magnifications.

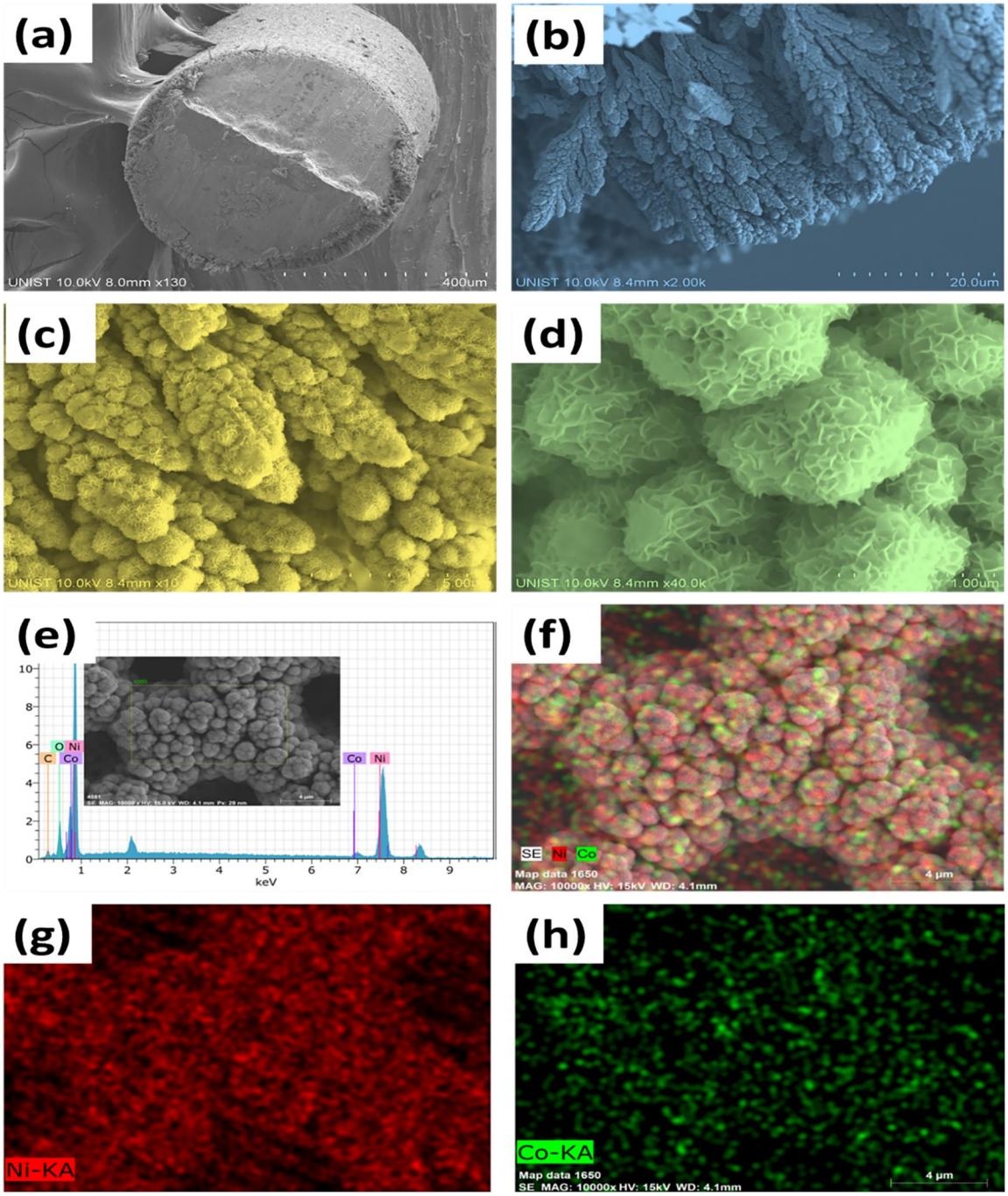

Figure 3. 2. (a-d) Cross-sectional images of 3D-NiCo LDH/Ni nanostructures. EDS spectrum (e) and elemental mappings (f-h) of 3D-NiCo LDH/Ni nanostructures.

The XRD pattern of NiCo LDH/3D-Ni is shown in **Figure 3. 3a**. The three major peaks observed at 44.7°, 52.0°, and 76.5° corresponds to the Ni wire current collector. Except for the peaks related with the Ni current collector, no peak was present in the XRD pattern of NiCo LDH/3D-Ni, which confirms the amorphous nature of the sample. The typical Raman spectrum of NiCo LDH/3D-Ni is shown in **Figure 3. 3b**. The characteristic peaks observed at 305 and 528 cm^{-1} correspond to the Co-O vibrational mode and the peak at 467 cm^{-1} is attributed to the Ni-O vibrational mode, which further confirms the formation of NiCo LDH. The elemental composition and the oxidation state of NiCo LDH/3D-Ni were evaluated by XPS, as shown in Figures 2c-f. A typical XPS survey spectrum of NiCo LDH/3D-Ni is displayed in **Figure 3. 3c**, where nickel (Ni 2p), cobalt (Co 2p), oxygen (O 1s), and carbon (C 1s) elements were presented. The high resolution Ni 2p spectrum in **Figure 3. 3d** exhibited two major peaks with the binding energy at 873.3 eV (Ni 2p 1/2) and 855.7 eV (Ni 2p 3/2) accompanied with two shakeup satellite peaks, which indicated the existence of the Ni^{2+} state. As shown in **Figure 3. 3e**, the high resolution Co 2p spectrum displayed two main peaks located at 797.2 eV (Co 2p1/2) and 781.3 eV (Co 2p 3/2) accompanied by two shakeup satellites, which confirmed the cobalt is in an ionic state (Co^{2+}). Finally, the high resolution O1 peak in **Figure 3. 3f** shows a major peak at 530.1 eV, attributed to hydroxyl ions revealing the formation of metallic hydroxides.

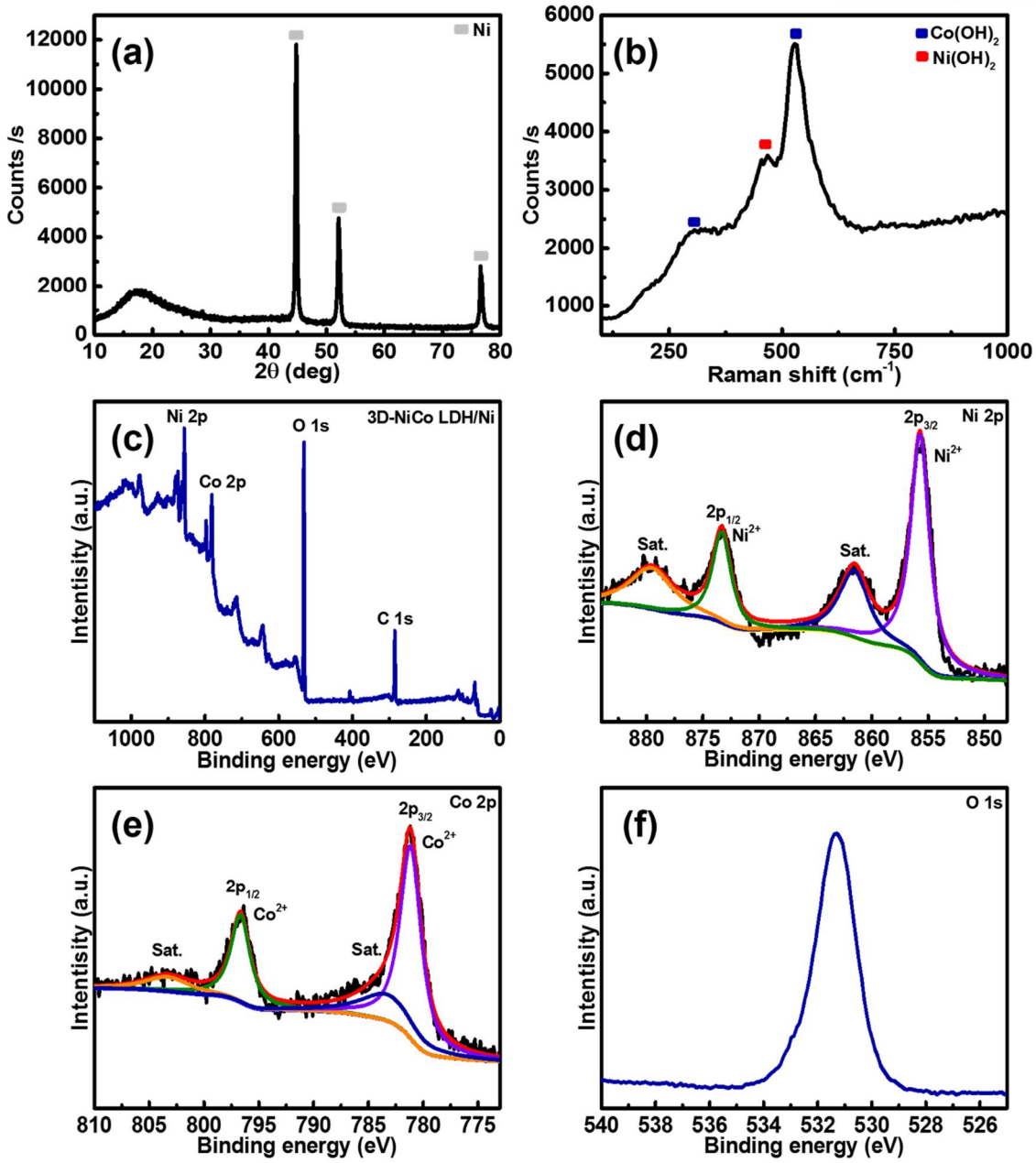

Figure 3. 3. (a) XRD patterns and (b) Raman spectra of 3D-NiCo LDH/Ni nanostructures. XPS spectra of 3D-NiCo LDH/Ni nanostructures (c) survey, (d) Ni 2p, (e) Co 2p and (f) O 1s.

The electrochemical properties of the as-prepared 3D-NiCo LDH/Ni nanostructures were investigated as electrode materials for asymmetric supercapacitors. Initially, the electrochemical tests such as cyclic voltammetry, galvanostatic charge/discharge, and electrochemical impedance spectroscopy measurements were carried out in a three electrode system with a 2 M KOH aqueous solution as the electrolyte. **Figure 3. 4a** shows CV curves of Ni, 3D-Ni, and 3D-NiCo LDH/Ni at a scan rate of 5 mV s^{-1}. The Ni-wire and 3D-Ni/Ni-wire exhibited one pair of cathodic and anodic peaks, indicating the existence of faradic redox reactions (Ni^{2+}/Ni^{3+}) and the 3D-NiCo LDH/Ni electrode exhibit three pairs of cathodic and anodic peaks, indicating the reversible faradaic redox process of Ni^{2+}/Ni^{3+} Co^{2+}/Co^{3+} and Co^{3+}/Co^{4+} transitions during the CV tests. Further, it can be observed that the closed area of the CV profile of 3D-NiCo LDH/Ni is larger than that of Ni and 3D-Ni, signifying that 3D-NiCo LDH/Ni affords much higher electrochemical performance. To further examine the electrochemical performance of the as-prepared electrodes, galvanostatic charge–discharge measurements were conducted. The typical galvanostatic charge/discharge curves of the Ni, 3D-Ni, and 3D-NiCo LDH/Ni electrodes at the current of 1 mA are shown in **Figure 3. 4b**. All of the curves showed the existence of potential plateaus in the charge/discharge profiles, suggesting faradaic characteristics arising from the redox process of the electrodes, which is in good agreement with the CV curves. The 3D-NiCo LDH/Ni electrode exhibited higher charge/discharge times compared to other current collectors, indicating the high capacitive behavior of 3D-NiCo LDH.

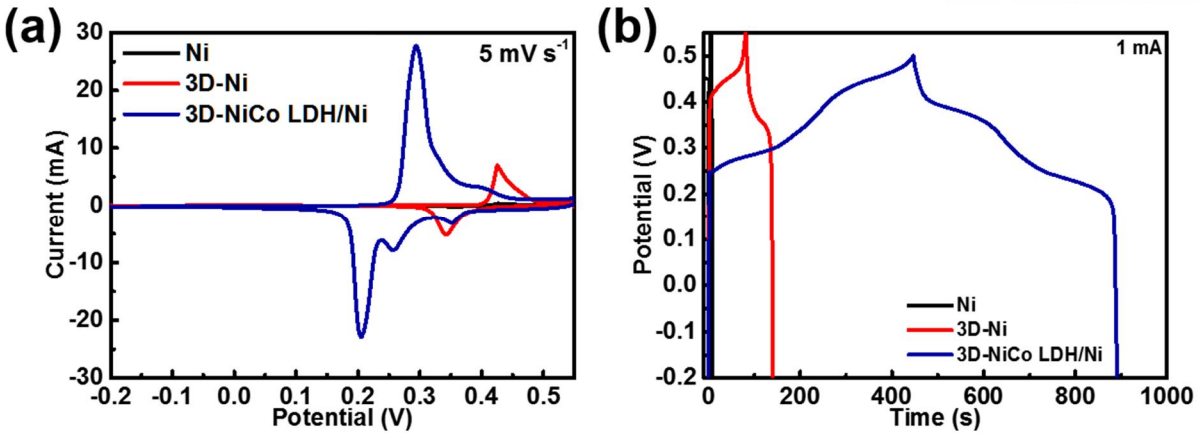

Figure 3. 4. (a and b) Cyclic voltammetry and charge/discharge profiles of Ni, 3D-Ni, and 3D-NiCo LDH/Ni nanostructures.

Further, the CV of 3D-NiCo LDH/Ni at different scan rates, ranging from 5 to 80 mV s^{-1} was measured as shown in **Figure 3. 5a**. All of the CV curves exhibited clear redox peaks, indicating a battery-type electrode. With increasing scan rate, the anodic and cathodic peaks are shifted towards positive and negative potentials, accompanying increasing current. Based on the CV profiles, the gravimetric, volumetric, areal, and length capacitance of the as-prepared electrode can be calculated by formulas (1), (3), (4), (5), and (6). The calculated gravimetric, volumetric, areal, and length capacitance of the 3D-NiCo LDH/Ni electrode at a scan rate of 5 mV s^{-1} is 2446 F g^{-1}, 73 F cm^{-3}, 1.04 F cm^{-2}, and 0.18 F cm^{-1}, respectively. **Figures 3. 5b-c** shows the specific capacitance as a function of the scan rate. When the scan rate increases, 88% of the specific capacitance was retained even at a high scan rate of 80 mV s^{-1}, indicating the higher rate capability of the as-prepared electrode. The higher rate capability of the as-prepared electrode is mainly due to the three dimensional architectures, which provides large open spaces for easy and fast access of electrolyte ions (low diffusion resistance) to the inner and outer surface of the electroactive materials and rapid charge transportation (lower contact resistance) for efficient redox reactions during the faradaic charge storage process. The galvanostatic charge/discharge test was also performed for the 3D-NiCo LDH/Ni electrode at various currents, as shown in **Figure 3. 5d**. The calculated gravimetric, volumetric, areal, and length capacitance of 3D-NiCo LDH/Ni from charge/discharge curves at a current of 0.5 mA using eqs. 2-6 are 2337 F g^{-1}, 70 F cm^{-3}, 0.99 F cm^{-2}, and 0.18 F cm^{-1}, respectively, with a decrease in discharge time and an increase of the current from 0.5 to 20 mA. The specific capacitance values versus current for 3D-NiCo LDH/Ni are displayed in **Figures 3. 5e-f**. The specific capacitance of the as-fabricated electrodes retained 76% of the initial capacitance, when the current was increased to a high rate of 20 mA, demonstrating good rate capability of the 3D-NiCo LDH/Ni. The obtained specific capacitance (Cg, Cv, Ca, and Cl) of the as-prepared 3D-NiCo LDH/Ni was significantly higher than that of previously reported battery-type wire electrodes including three-dimensional flower-like $NiCo_2O_4$/Ni nanostructures on Ni-wire.

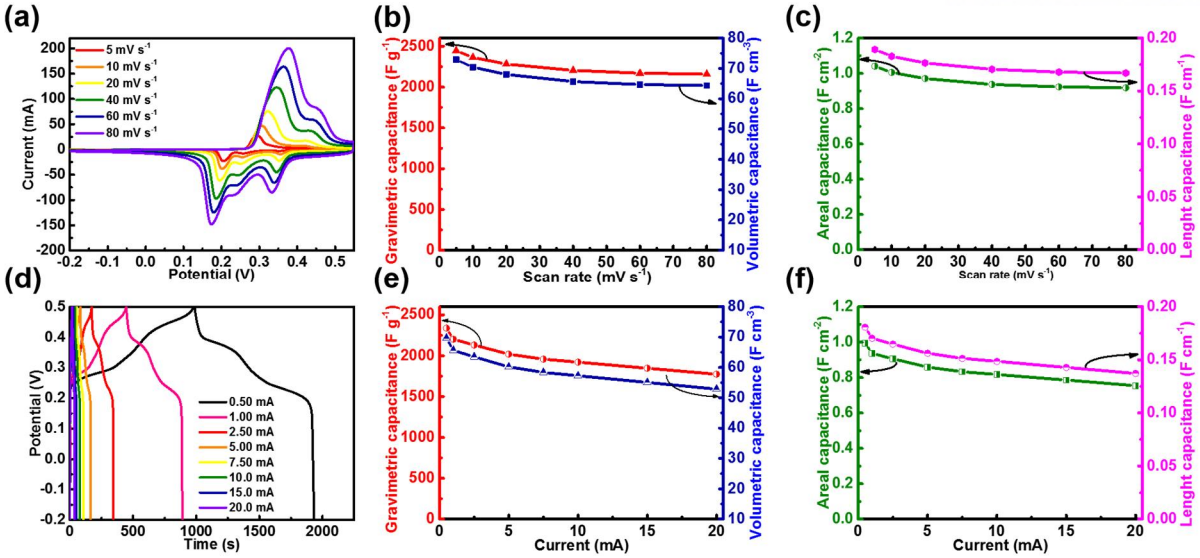

Figure 3. 5. (a) Cyclic voltammetry profiles and (b and c) specific capacitance of 3D-NiCo LDH/Ni nanostructures at various scan rates. (d) Galvanostatic charge/discharge profiles and (e and f) specific capacitance of 3D-NiCo LDH/Ni nanostructures at different currents.

The electrochemical stability of as-prepared 3D-NiCo LDH/Ni was evaluated by a repeated galvanostatic charge/discharge test at a constant current of 15 mA for 10,000 cycles. **Figure 3. 6** shows the capacitance retention as a function of the cycle number and the inset displays the charge/discharge curves of the initial and final 50 cycles. It was observed that the specific capacitance shows a gradual increase at the first 1000 cycles, and then decreases slowly until 89% of the initial capacitance remains even after 10,000 cycles, indicating good cycling stability of the 3D-NiCo LDH/Ni. The initial increase of the first 1000 cycles is attributed to the electro-activation process of the electroactive materials. Initially, the electroactive materials are not fully exposed to the electrolyte, because the 3D-NiCo LDH/Ni porous nanostructure is formed by numerous interconnected nanosheets over the interconnected nanoparticle surface, and a certain period of time is thus required for the diffusion of the electrolyte into the entire surface. By continuous charge/discharge cycles and more efficient soaking time of the active materials in the electrolyte, the bulk and the interior part of the electroactive materials are activated, which leads to the increase in specific capacitance.

The resistance characteristics of 3D-NiCo LDH/Ni before and after the cycle test were investigated by EIS measurements. **Figure 3. 7** shows Nyquist plots of the 3D-NiCo LDH/Ni before and after the 10,000 cycles test. The negligible semicircle arc at a high frequency region before the cycle test indicates good electrical conductivity of the electrode. The Nyquist plot of 3D-NiCo LDH/Ni after 10,000 cycles exhibited a semi-circle arc at the high frequency region followed by a straight line at the low frequency region, which validates stable capacitive behavior. The increase of charge transfer resistance after 10,000 cycles might be due to the loss of adhesion of some active materials from the current collector due to the continuous adsorption and desorption of OH^- ions. To confirm the structural stability of the active materials after the cycling test, a FE-SEM analysis was performed. **Figures 3. 8a-b** present FE-SEM images of the 3D-NiCo LDH/Ni nanostructure after a long-term cycling test. As shown in **Figures 3. 8a-b**, the flower-like morphology is well maintained and no obvious structural deformations are observed even after 10,000 cycles, indicating the robust nature of the 3D-NiCo LDH/Ni nanostructure.

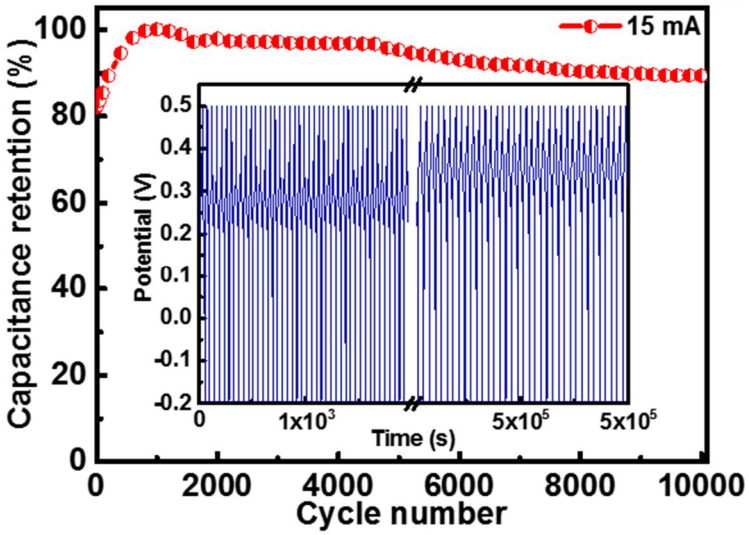

Figure 3. 6. Cyclic stability of 3D-NiCo LDH/Ni nanostructures obtained at a current of 15mA; the inset shows the charge/discharge curves.

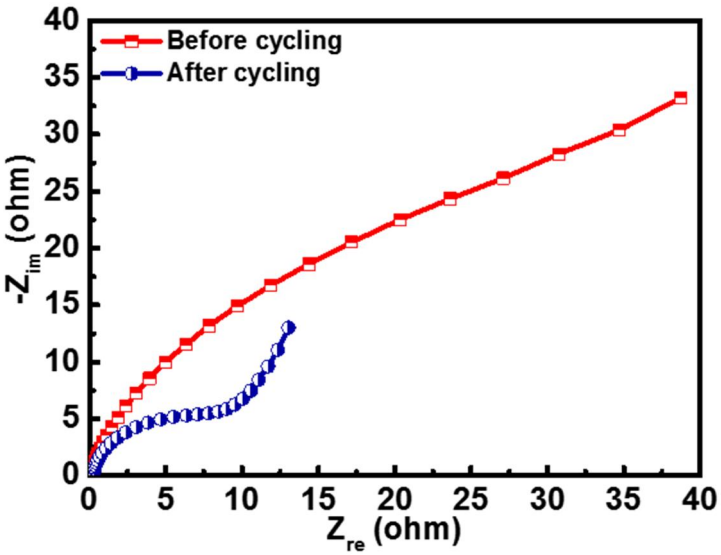

Figure 3. 7. Nyquist plots of 3D-NiCo LDH/Ni nanostructures electrode before and after the 10,000 cycle test.

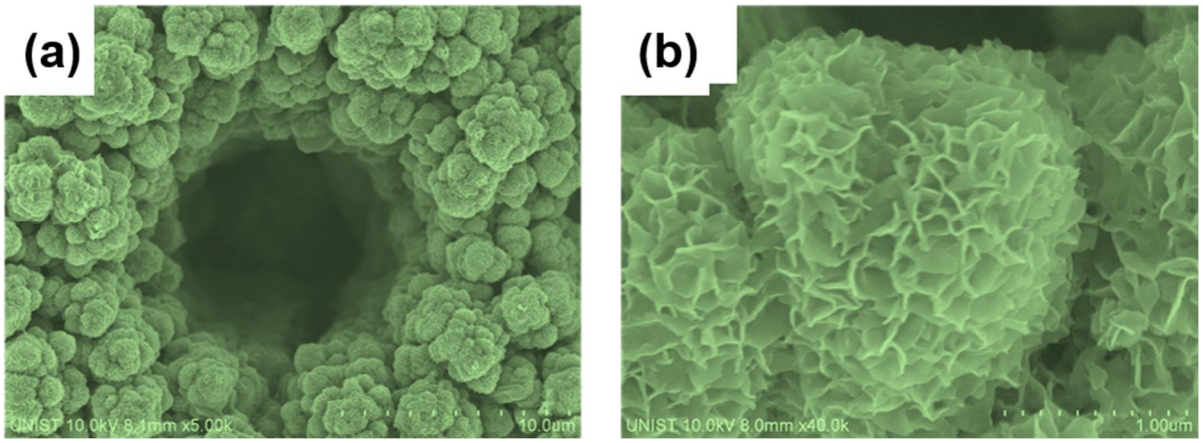

Figure 3. 8. (a-b) FE-SEM images of 3D-NiCo LDH/Ni electrode after the 10,000 cycles test.

To evaluate the possibility of employing the as-obtained 3D-NiCo-LDH@Ni wire in practical applications, an asymmetric supercapacitor was further fabricated by utilizing the 3D-NiCo-LDH@Ni wire as the anode and the 3D-Mn3O4@Ni wire as the cathode, and a schematic representation of the asymmetric hybrid supercapacitor is shown in **Figure 3. 9**. The characterization of Mn3O4 is shown in **Figure 3. 10**. The 3D-Mn3O4@Ni wire electrode displayed excellent electric double-layer capacitance and pseudocapacitance property at -1.0 V to -0.2 V, as shown in **Figure 3. 11**. The specific capacitance of the 3D-Mn3O4@Ni wire was calculated from its galvanostatic charge-discharge curves and reached up to 848.8F/g at 2A/g, which is superior to any other previously reported AC-based supercapacitors.[32] The as-fabricated asymmetric supercapacitor exhibited capacitive behavior at 0-1.8 V with the double contribution of the electric double-layer capacitance and pseudocapacitance, as shown in **Figure 3. 12a**. **Figure 3. 12b** shows charge–discharge curves of the 3D-NiCo LDH/Ni//3D-Mn3O4/Ni asymmetric supercapacitor at various currents from 0.5 to 10 A/g. The specific capacitances were calculated to be 331, 342.5, 344.25, 307.25, 248, and 215 F/g based on the total mass of the active materials at current densities of 0.5, 1, 2.5, 5, 7.5, and 10 A/g, respectively, as seen in **Figure 3. 12c**, from the galvanostatic charge-discharge curves in **Figure 3. 12b**. Furthermore, the calculated volumetric capacitance of the 3D-NiCo LDH/Ni//3D-Mn3O4/Ni asymmetric supercapacitor at a current density of 0.015 A/cm3 was 9.86 F/cm3. When the current density increases, 92.8 % of the volumetric capacitance was retained even at a high current density of 0.075 A/cm3, indicating the higher rate capability of the as-prepared asymmetric supercapacitor.

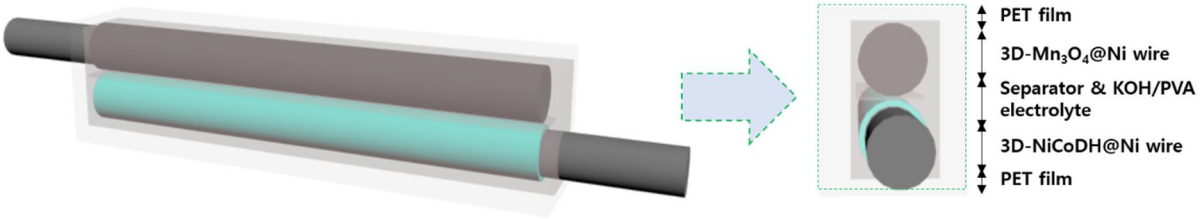

Figure 3. 9. Schematic representation of the fabrication of 3D-NiCo LDH/Ni//3D-Mn_3O_4/Ni asymmetric supercapacitor.

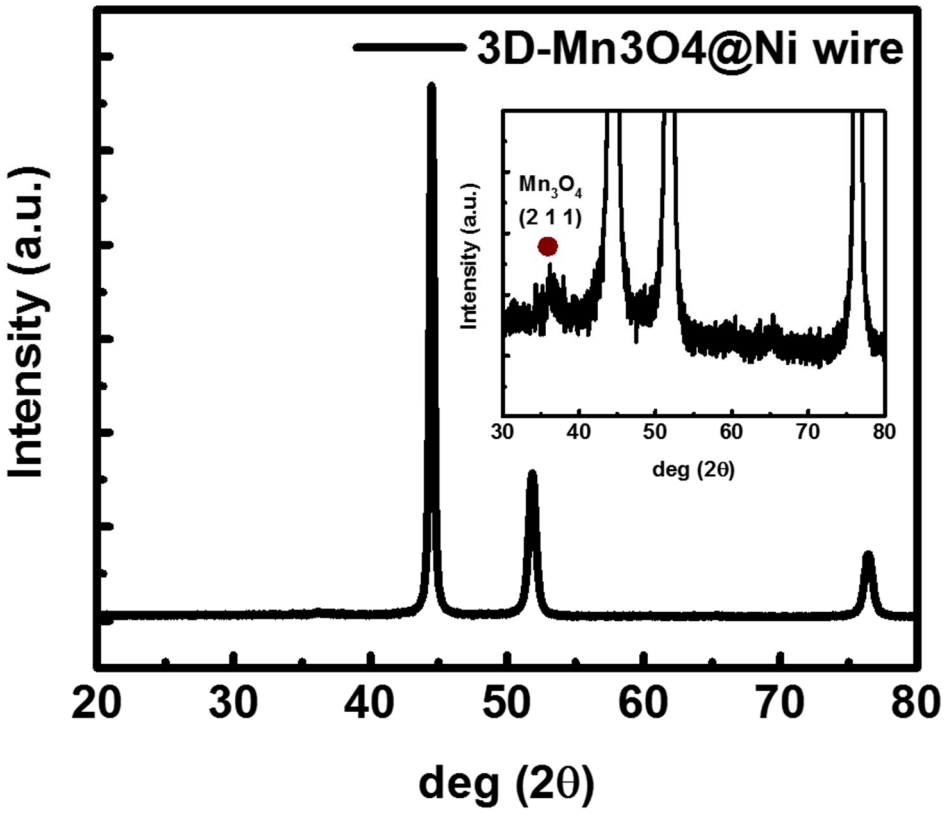

Figure 3. 10. XRD patterns of 3D-Mn_3O_4/Ni. The inset shows enlarged XRD patterns of 3D-Mn_3O_4/Ni.

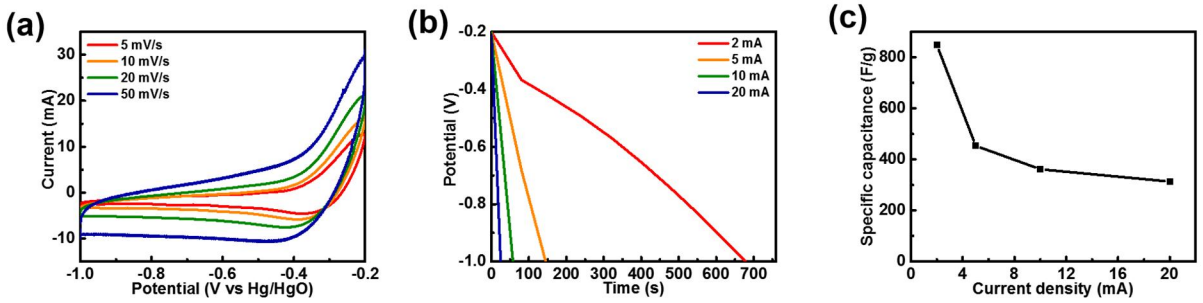

Figure 3. 11. Cyclic voltammetry profiles, galvanostatic charge/discharge profiles and specific

capacitance of 3D-Mn_3O_4/Ni nanostructures.

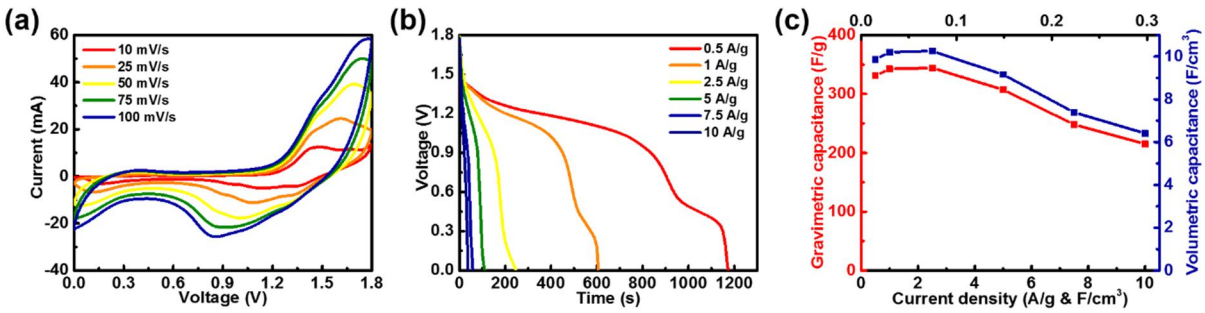

Figure 3. 12. (a) CV curves of the asymmetric supercapacitor at different scan rates. (b) Galvanostatic charge-discharge curves and (c) specific capacitance of the asymmetric supercapacitor at different current densities.

The Ragone plot, related to power densities (P) and energy densities (E), was further used to evaluate the performance of the 3D-NiCo LDH/Ni//3D-Mn3O4/Ni device. The P and E values of the asymmetric supercapacitor were calculated using the following equations:

$$E = \frac{1}{2} \times C_m \times (\Delta V)^2$$

$$P = \frac{E}{\Delta t}$$

where C_m is calculated based on the GCD curves of the asymmetric supercapacitor device, $\triangle V$ is the operating voltage of the cell, and $\triangle t$ is the discharge time.

The maximum energy density of our asymmetric supercapacitor was calculated to be 153.3 Wh/kg (4.59 mWh/cm^3) at a power density of 2238 W/kg (67.05 mW/cm^3) based on the total mass of active materials, as shown in **Figure 3. 13** and **Figure 3. 14**. At a high discharge current of 10 A/g, the energy density still remained at 92.8 Wh/kg (2.78 mWh/cm^3) at a power density of 8810 W/kg (263.91 mW/cm^3). Moreover, the highest energy density obtained considerably exceeded the values of almost all asymmetric supercapacitors either based on nickel cobalt hydroxides and their composites or wire-/fiber-shape supercapacitors reported to date: ultrathin MnO_2/carbon fiber (CF) (27.2 Wh/kg)[33], TiN@graphene nanosheet (GNS)/CF (15.4 Wh/kg)[34], CuHCF@CF (10.6 Wh/kg)[35], Ni_2CoS_4@$NiCo_2O_4$/CFP (32.2 Wh/kg)[36], and $Ni(OH)_2$-RGO/Ni wire (24.5 Wh/kg)[37], NiCo DH/Ni foam (48 Wh/kg)[38], NiCo DH/graphene/CNT composites (41 Wh/kg)[39], NiCo LDH/Ni (91.76 Wh/kg)[40], and NiCo DH/rGO (56.1 Wh/kg)[41]. In specific, wire-shaped/fiber supercapacitors show much lower energy densities due to lower exposed surface areas and poor mechanical performance compared to traditional planar supercapacitors. However, our wire-shaped asymmetric supercapacitor based on 3D-NiCo LDH/Ni and 3D-Mn3O4/Ni delivered high energy density and power density, demonstrated the ability to store a lot of energy in a small volume, and to output large amounts of energy based on its volume, and therefore is suitable for practical applications. The superior electrochemical performance of the asymmetric supercapacitor can be reasonably attributed to the high energy contribution of the 3D-NiCo-LDH@Ni wire, as discussed above.

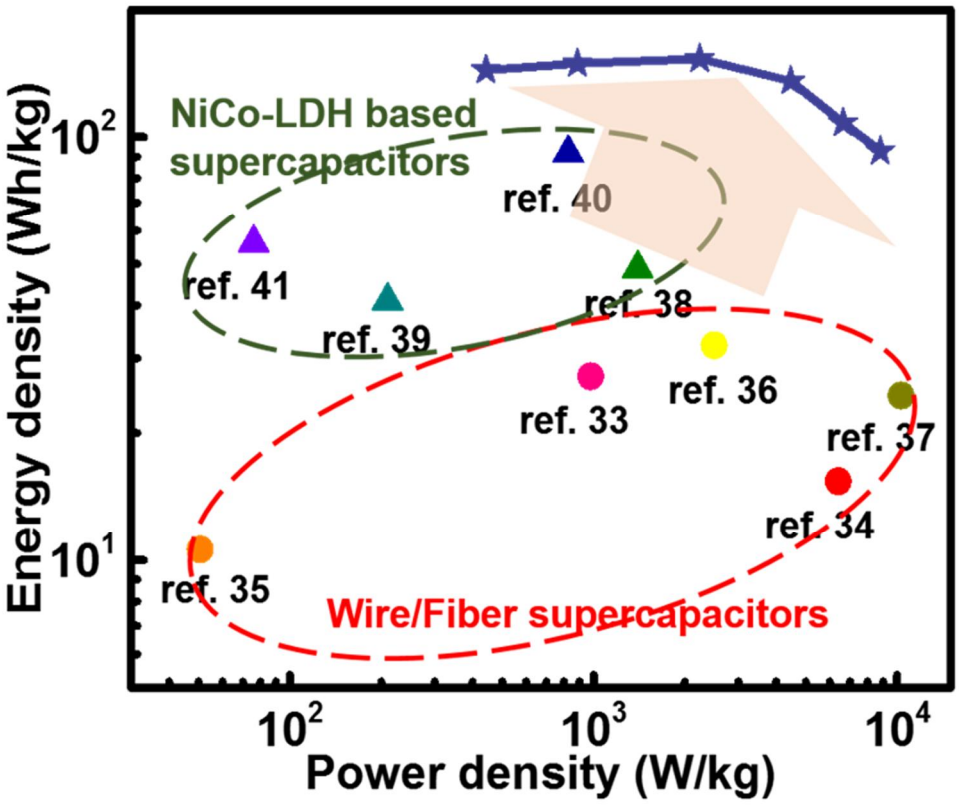

Figure 3. 13. Ragone plots of our supercapacitor based on a full cell, compared with other electrodes using NiCo-LDH.

Current Density (A/g)	Energy Density (Wh/kg)	Power Density (W/kg)
0.5	144.2	442.7
1	149.3	885.9
2.5	153.3	2238.5
5	135.8	4459.6
7.5	108.2	6645.8
10	92.8	8810.8

Figure 3. 14. Table of energy density and power density as a function of current density.

Galvanostatic charge-discharge measurement was used to evaluate the durability of the as-fabricated asymmetric supercapacitor at a current density of 20 A/g as shown in **Figure 3.15a**. Cycle stability is the one of the most important requirements for practical implementation in energy storage devices. The capacitance retention of the asymmetric cell after 10,000 cycles of charge/discharge at a current density of 20A/g was 80.7%, which implies that the asymmetric pseudocapacitor has relatively good stability. This indicates that the 3D-NiCo LDH/Ni//3D-Mn3O4/Ni has low electrode resistance and a high charge-transfer rate between the electrolyte and the active materials. The limited structural damage of the as-prepared supercapacitor during a long charge/discharge process, due to the gel electrolyte, helped achieve superior cycling stability, as shown in **Figure 3. 15b**. The Nyquist plots of the EIS spectra with a frequency from 10 kHz to 0.01 Hz show that there were minimal changes in the EIS of the 3D-NiCo LDH/Ni//3D-Mn3O4/Ni asymmetric supercapacitors after 10,000 cycle tests, proving its excellent electrochemical and mechanical stability.

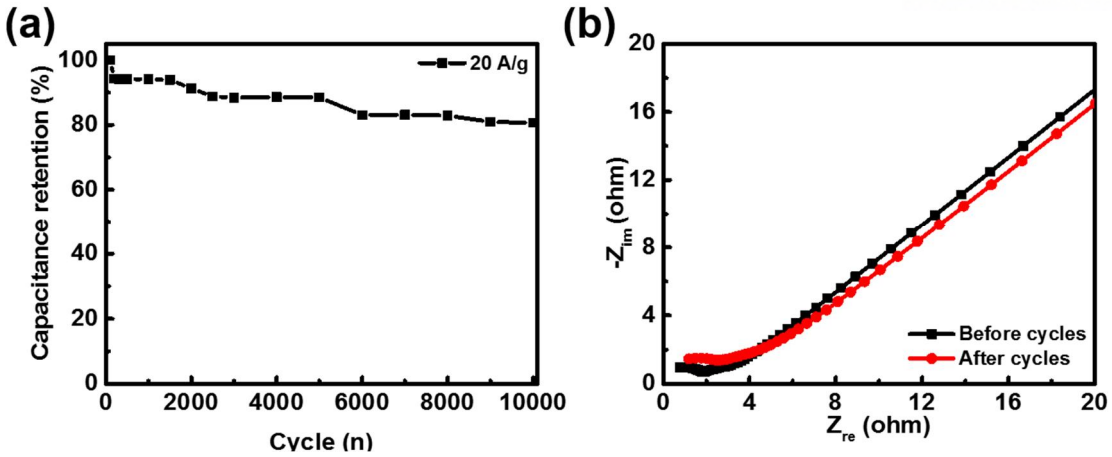

Figure 3. 15. (a) Cycling performance of the asymmetric supercapacitor for 10,000 cycles, and (b) Comparison of Nyquist plots of 3D-NiCo-LDH/Ni//3D-Mn3O4/Ni wire electrode before and after 10,000 cycles.

In order to demonstrate the flexibility of our device, we measured CV curves at 50 mV/s with a bending angle from 0 to 150°, as shown in **Figure 3. 16** and **Figure 3. 17**. The CV curves and FE-SEM images (**Figure 3. 18**) of the 3D-NiCo LDH/Ni nanostructures under several bending conditions reveals that there is no significant difference, demonstrating the highly flexible property of the 3D-NiCo LDH/Ni//3D-Mn3O4/Ni asymmetric supercapacitor. To consider the performance of the fabricated supercapacitors in real-world applications, it is necessary to connect wire supercapacitors either in series or in parallel, or in a combination of both, to boost the ability of the supercapacitor for powering various portable electronic devices. **Figures 3. 19a-b** show the CV and GCD curves of single and two wire supercapacitors connected in parallel. Compared with a single device (1.8 V), the output current and the discharge time of the two devices connected in parallel are increased by a factor of two compared with a single device at the same constant current density of 20 A/g. **Figures 3. 19c-d** show the CV and GCD curves of single and two wire supercapacitors connected in series. Compared with a single device (1.8 V), the output of the two devices connected in series exhibited a larger potential window of 3.6 V. The device efficiently powered 5mm diameter green (3.5 V, 20mA), white (3.5 V, 20mA), and red (2.3 V, 20mA) round light-emitting diode (LED) indicators after being charged for tens of seconds at 3.6V, as shown in **Figure 3. 20**. In addition, the green LED remained very bright after 30 min and was even able to operate as an indicator after 60 min.

Figure 3. 21 shows the LCD devices operating as indicators for temperature, time, alarm, and stop watch with various colors, which verify that our devices, connected to two asymmetric supercapacitors in series, are operating perfectly. Furthermore, the flexible supercapacitor successfully powered an electrical watch and a thermometer and hygrometer, as shown in **Figure 3. 22**, suggesting the strong potential of our supercapacitor in any portable and wearable device.

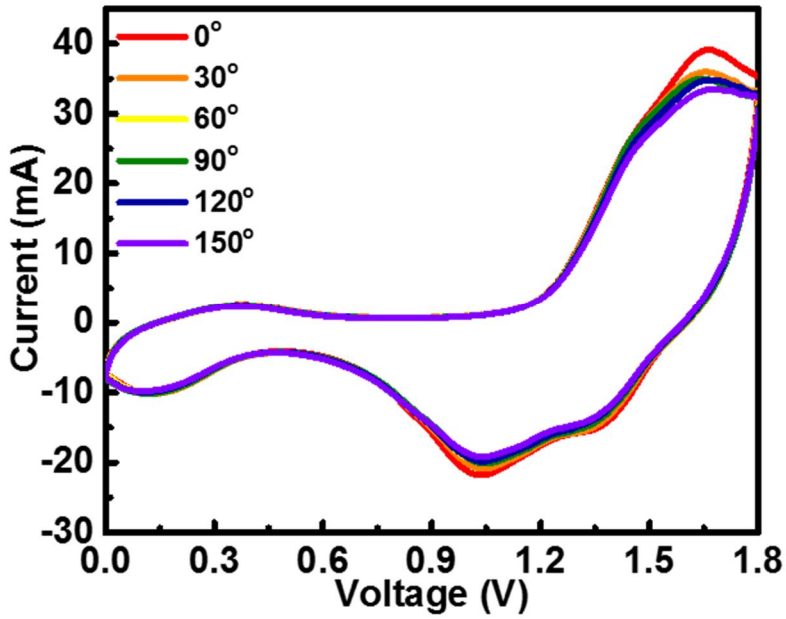

Figure 3. 16. CV curves of single wire supercapacitor by bending durability

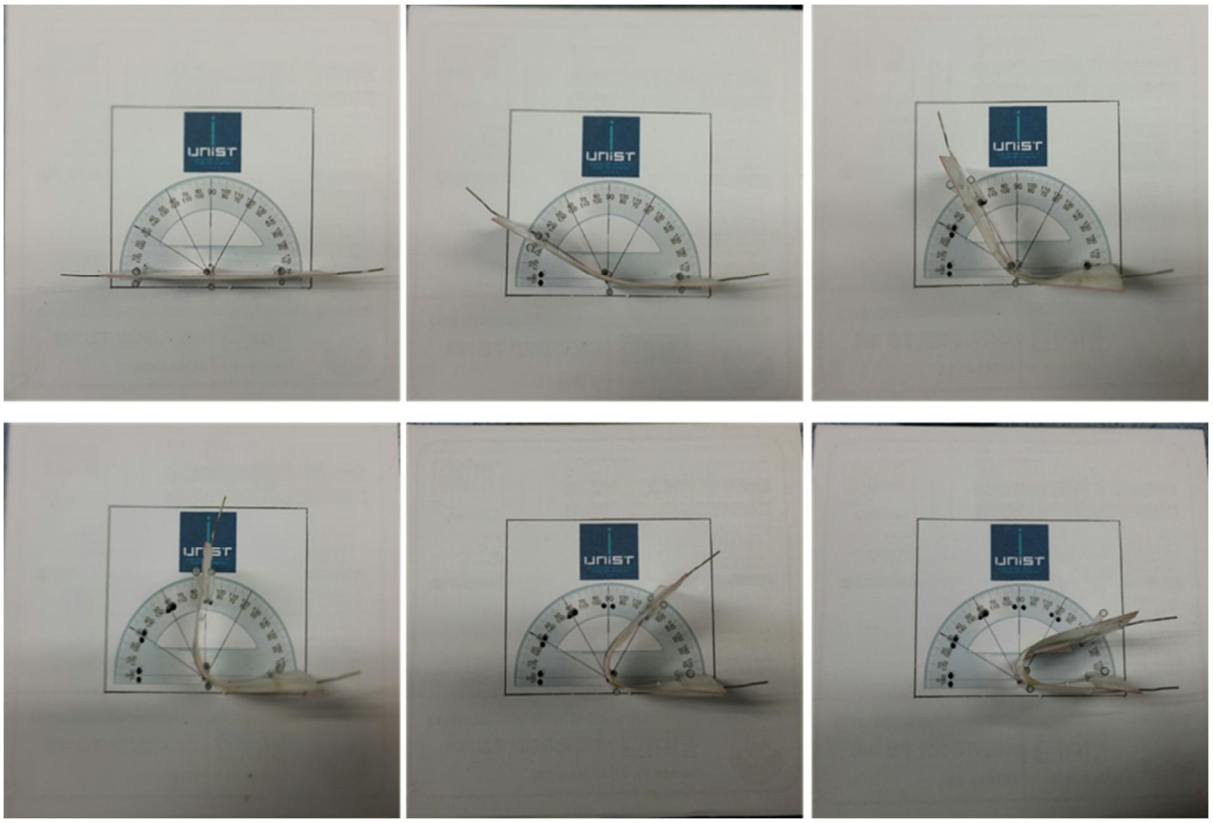

Figure 3. 17. Digital images of 3D-NiCo LDH/Ni//3D-Mn_3O_4/Ni as a function of bending degree.

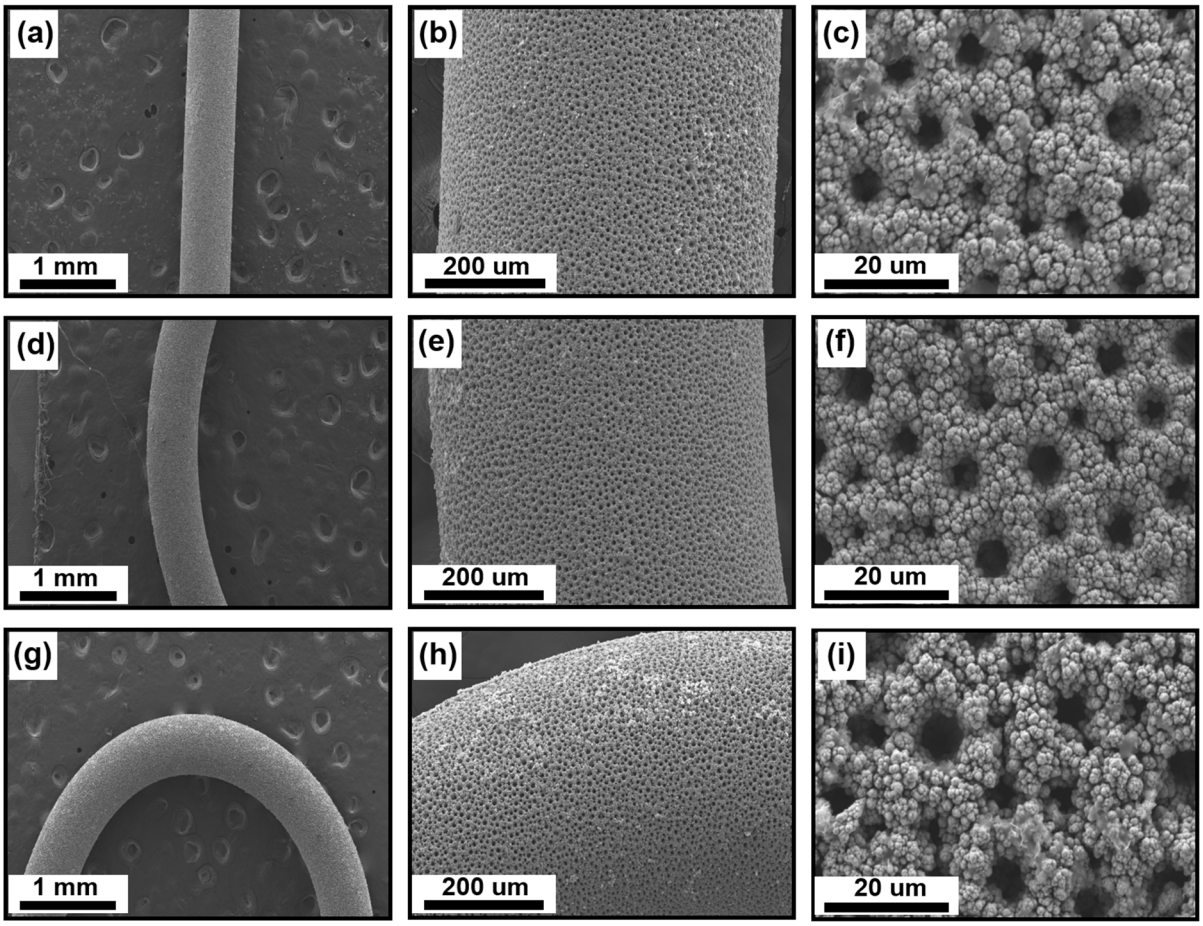

Figure 3. 18. FE-SEM images of 3D-NiCo LDH/Ni under a bending condition. (a-c) 0°C, (d-f) 90°C, and (g-i) 180°C.

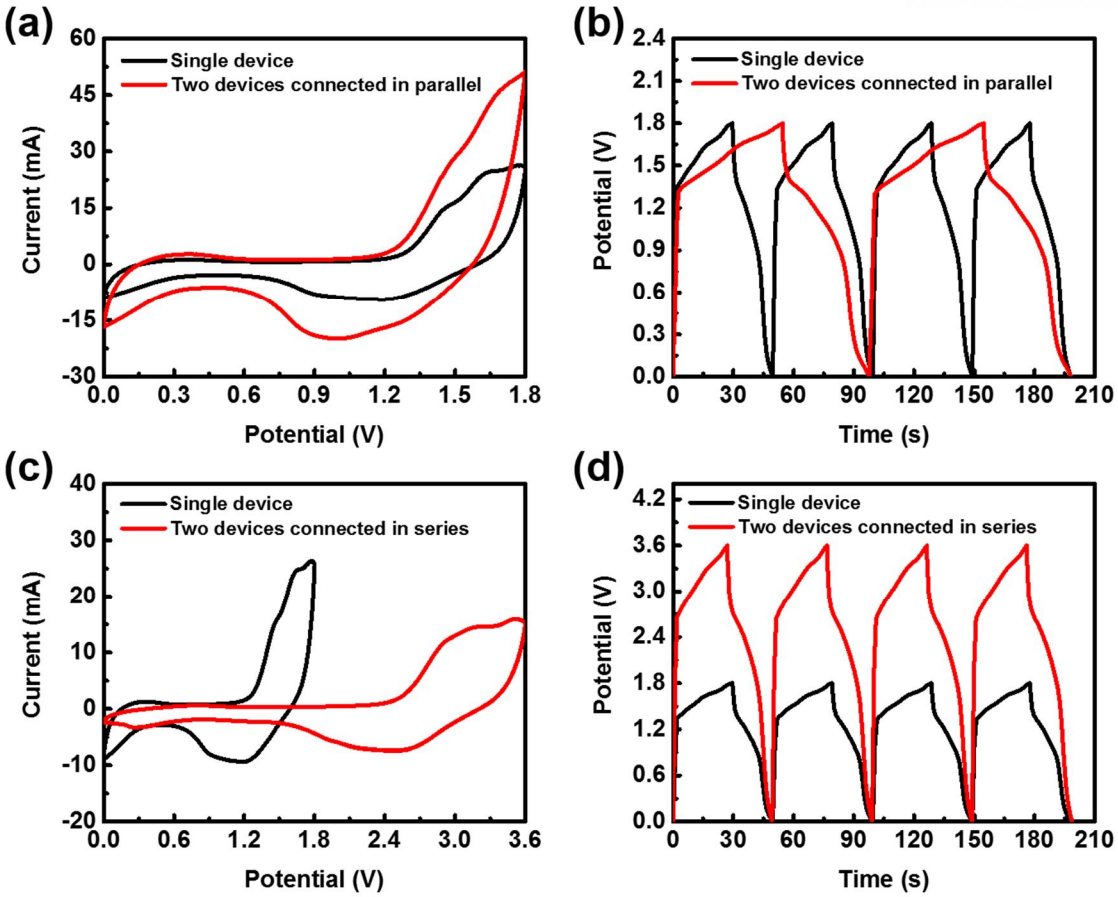

Figure 3. 19. CV curves of single and two wire supercapacitor devices connected in (a) parallel and (c) series. GCD curves of single and two wire supercapacitors connected in (b) parallel and (d) series.

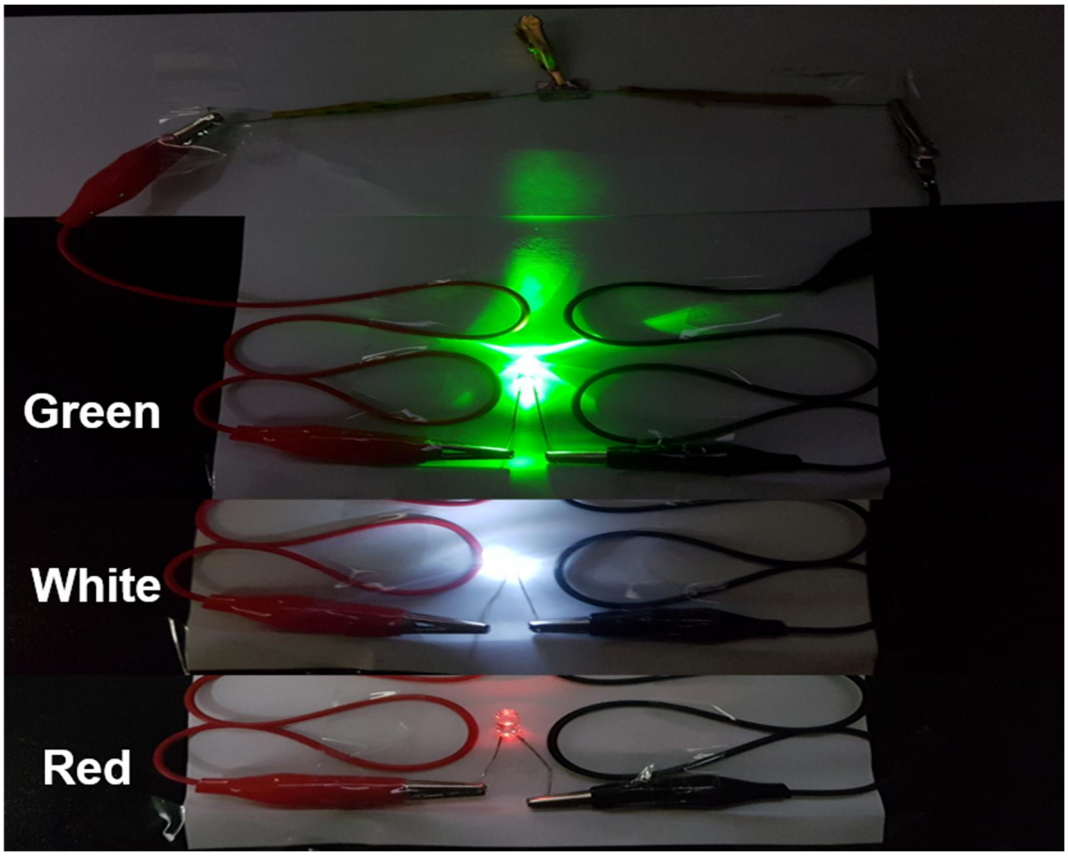

Figure 3. 20. A digital image of the green, white, and red LED indicator powered by two wire supercapacitors in series.

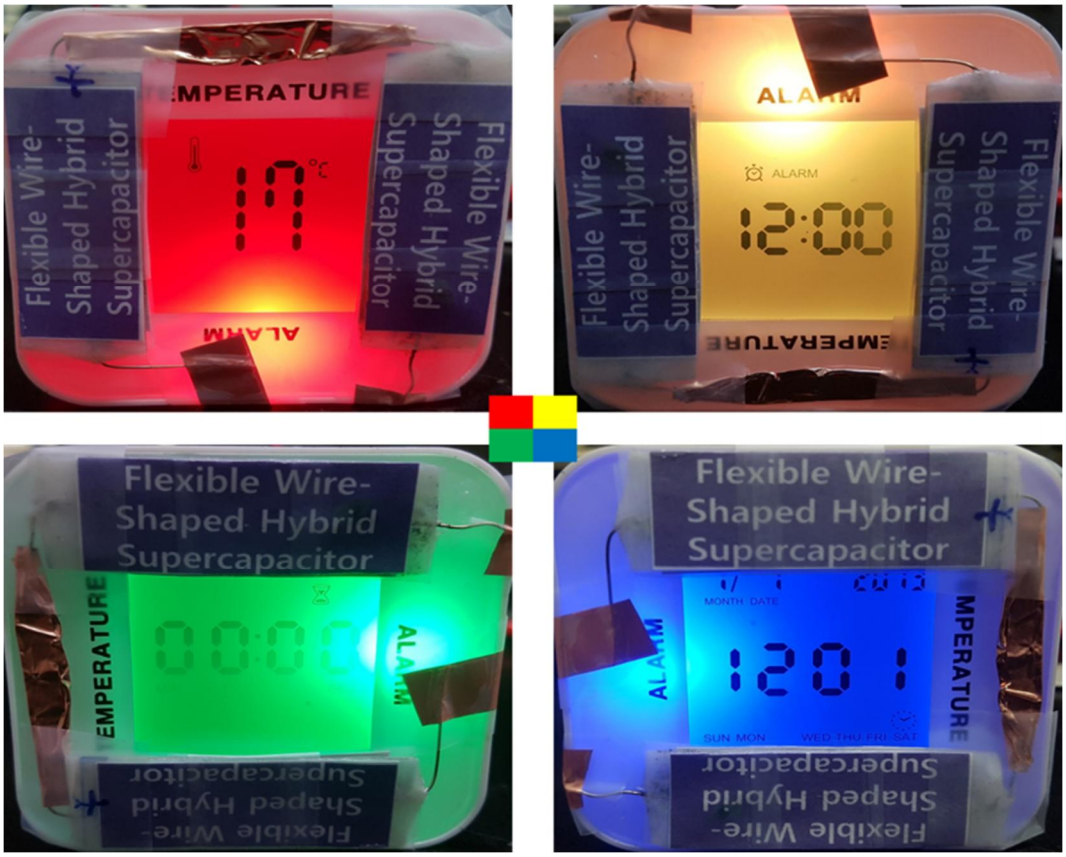

Figure 3. 21. A digital image of the LCD devices with various colors powered by two wire supercapacitors in series.

Figure 3. 22. A digital image of the thermometer, hygrometer, and wearable electrical watch powered by two wire supercapacitors in series.

3. 4. Conclusion

We have fabricated a facile flexible wire-shaped hybrid supercapacitor by the integration of 3D-NiCo LDH/3D-Ni electrodes via a simple electrodeposition and hydrothermal method. The electrodes delivered a high capacitance of 2446 F/g, excellent rate capability, and cycle stability. In particular, the hybrid supercapacitor exhibited a battery-like energy density of 153.3 Wh/kg at a power density of 8810 W/kg. Furthermore, it successfully performed as a flexible energy storage devices for a green LED light and a wearable watch under normal bending conditions. These promising results demonstrate that the flexible wire-shaped supercapacitor has remarkable potential in a wide range of applications, including flexible, wearable, and portable electronic devices.

3. 5. References

1. Service, R. F., Technology. Electronic textiles charge ahead. *Science* **2003,** *301* (5635), 909-11.

2. Yamada, T.; Hayamizu, Y.; Yamamoto, Y.; Yomogida, Y.; Izadi-Najafabadi, A.; Futaba, D. N.; Hata, K., A stretchable carbon nanotube strain sensor for human-motion detection. *Nat Nanotechnol* **2011,** *6* (5), 296-301.

3. Kim, D.-H.; Rogers, J. A., Stretchable Electronics: Materials Strategies and Devices. *Advanced Materials* **2008,** *20* (24), 4887-4892.

4. Haghi, M.; Thurow, K.; Stoll, R., Wearable Devices in Medical Internet of Things: Scientific Research and Commercially Available Devices. *Healthc Inform Res* **2017,** *23* (1), 4-15.

5. Zeng, W.; Shu, L.; Li, Q.; Chen, S.; Wang, F.; Tao, X. M., Fiber-based wearable electronics: a review of materials, fabrication, devices, and applications. *Adv Mater* **2014,** *26* (31), 5310-36.

6. Koo, M.; Park, K. I.; Lee, S. H.; Suh, M.; Jeon, D. Y.; Choi, J. W.; Kang, K.; Lee, K. J., Bendable inorganic thin-film battery for fully flexible electronic systems. *Nano Lett* **2012,** *12* (9), 4810-6.

7. Hwang, B. U.; Lee, J. H.; Trung, T. Q.; Roh, E.; Kim, D. I.; Kim, S. W.; Lee, N. E., Transparent Stretchable Self-Powered Patchable Sensor Platform with Ultrasensitive Recognition of Human Activities. *ACS Nano* **2015,** *9* (9), 8801-10.

8. Kim, S.; Kwon, H. J.; Lee, S.; Shim, H.; Chun, Y.; Choi, W.; Kwack, J.; Han, D.; Song, M.; Kim, S.; Mohammadi, S.; Kee, I.; Lee, S. Y., Low-power flexible organic light-emitting diode display device. *Adv Mater* **2011,** *23* (31), 3511-6.

9. Wen, Z.; Yeh, M. H.; Guo, H.; Wang, J.; Zi, Y.; Xu, W.; Deng, J.; Zhu, L.; Wang, X.; Hu, C.; Zhu, L.; Sun, X.; Wang, Z. L., Self-powered textile for wearable electronics by hybridizing fiber-shaped nanogenerators, solar cells, and supercapacitors. *Sci Adv* **2016,** *2* (10), e1600097.

10. Shi, S.; Xu, C.; Yang, C.; Li, J.; Du, H.; Li, B.; Kang, F., Flexible supercapacitors. *Particuology* **2013,** *11* (4), 371-377.

11. Liu, L.; Shen, B.; Jiang, D.; Guo, R.; Kong, L.; Yan, X., Watchband-Like Supercapacitors with Body Temperature Inducible Shape Memory Ability. *Advanced Energy Materials* **2016,** *6* (16).

12. Ramadoss, A.; Saravanakumar, B.; Kim, S. J., Thermally reduced graphene oxide-coated fabrics for flexible supercapacitors and self-powered systems. *Nano Energy* **2015,** *15*, 587-597.

13. Zhou, Q.; Ye, X.; Wan, Z.; Jia, C., A three-dimensional flexible supercapacitor with enhanced performance based on lightweight, conductive graphene-cotton fabric electrode. *Journal of Power Sources* **2015,** *296*, 186-196.

14. Ramadoss, A.; Yoon, K.-Y.; Kwak, M.-J.; Kim, S.-I.; Ryu, S.-T.; Jang, J.-H., Fully flexible, lightweight, high performance all-solid-state supercapacitor based on 3-Dimensional-graphene/graphite-paper. *Journal of Power Sources* **2017,** *337*, 159-165.

15. Kim, S.-I.; Kang, J.-H.; Kim, S.-W.; Jang, J.-H., A new approach to high-performance flexible supercapacitors: Mesoporous three-dimensional Ni-electrodes. *Nano Energy* **2017,** *39*, 639-646.

16. Jost, K.; Dion, G.; Gogotsi, Y., Textile energy storage in perspective. *Journal of Materials Chemistry A* **2014,** *2* (28).

17. Yu, D.; Qian, Q.; Wei, L.; Jiang, W.; Goh, K.; Wei, J.; Zhang, J.; Chen, Y., Emergence of fiber supercapacitors. *Chem Soc Rev* **2015,** *44* (3), 647-62.

18. Cai, X.; Peng, M.; Yu, X.; Fu, Y.; Zou, D., Flexible planar/fiber-architectured supercapacitors for wearable energy storage. *J. Mater. Chem. C* **2014,** *2* (7), 1184-1200.

19. Zhang, Y. Z.; Wang, Y.; Cheng, T.; Lai, W. Y.; Pang, H.; Huang, W., Flexible supercapacitors based on paper substrates: a new paradigm for low-cost energy storage. *Chem Soc Rev* **2015,** *44* (15), 5181-99.

20. Ramadoss, A.; Kang, K.-N.; Ahn, H.-J.; Kim, S.-I.; Ryu, S.-T.; Jang, J.-H., Realization of high performance flexible wire supercapacitors based on 3-dimensional NiCo2O4/Ni fibers. *Journal of Materials Chemistry A* **2016,** *4* (13), 4718-4727.

21. Dong, L.; Xu, C.; Li, Y.; Huang, Z.-H.; Kang, F.; Yang, Q.-H.; Zhao, X., Flexible electrodes and supercapacitors for wearable energy storage: a review by category. *Journal of Materials Chemistry A* **2016,** *4* (13), 4659-4685.

22. Huang, Y.; Zhi, C., Functional flexible and wearable supercapacitors. *Journal of Physics D: Applied Physics* **2017,** *50* (27).

23. Liu, W.-w.; Yan, X.-b.; Lang, J.-w.; Peng, C.; Xue, Q.-j., Flexible and conductive nanocomposite electrode based on graphene sheets and cotton cloth for supercapacitor. *Journal of Materials Chemistry* **2012,** *22* (33).

24. Jost, K.; Durkin, D. P.; Haverhals, L. M.; Brown, E. K.; Langenstein, M.; De Long, H. C.; Trulove, P. C.; Gogotsi, Y.; Dion, G., Natural Fiber Welded Electrode Yarns for Knittable Textile Supercapacitors. *Advanced Energy Materials* **2015,** *5* (4).

25. Gao, L.; Surjadi, J. U.; Cao, K.; Zhang, H.; Li, P.; Xu, S.; Jiang, C.; Song, J.; Sun, D.; Lu, Y., Flexible Fiber-Shaped Supercapacitor Based on Nickel-Cobalt Double Hydroxide and Pen Ink Electrodes on Metallized Carbon Fiber. *ACS Appl Mater Interfaces* **2017,** *9* (6), 5409-5418.

26. Vellacheri, R.; Zhao, H.; Mühlstädt, M.; Al-Haddad, A.; Jandt, K. D.; Lei, Y., Rationally Engineered Electrodes for a High-Performance Solid-State Cable-Type Supercapacitor. *Advanced Functional Materials* **2017,** *27* (18).

27. Wang, X.; Jiang, K.; Shen, G., Flexible fiber energy storage and integrated devices: recent progress and perspectives. *Materials Today* **2015,** *18* (5), 265-272.

28. Senthilkumar, S. T.; Wang, Y.; Huang, H., Advances and prospects of fiber supercapacitors. *Journal of Materials Chemistry A* **2015,** *3* (42), 20863-20879.

29. Kim, D.; Keum, K.; Lee, G.; Kim, D.; Lee, S.-S.; Ha, J. S., Flexible, water-proof, wire-type supercapacitors integrated with wire-type UV/NO 2 sensors on textiles. *Nano Energy* **2017,** *35*, 199-206.

30. Celine Largeot, C. P., John Chmiola, Pierre-Louis Taberna, Yury Gogotsi, and Patrice Simon, Relation between the Ion Size and Pore Size for an Electric Double-Layer Capacitor. *J. AM. CHEM. SOC.* **2008,** *130* (9), 2730-2731.

31. Kim, S.-I.; Kang, K.-N.; Kim, S.-W.; Jang, J.-H., A one-step practical strategy to enhance overall supercapacitor performance. *RSC Adv.* **2014,** *4* (103), 59310-59314.

32. Kang, K. N.; Kim, I. H.; Ramadoss, A.; Kim, S. I.; Yoon, J. C.; Jang, J. H., Ultrathin nickel hydroxide on carbon coated 3D-porous copper structures for high performance supercapacitors. *Phys Chem Chem Phys* **2017**.

33. Yu, N.; Yin, H.; Zhang, W.; Liu, Y.; Tang, Z.; Zhu, M.-Q., High-Performance Fiber-Shaped All-Solid-State Asymmetric Supercapacitors Based on Ultrathin MnO2

Nanosheet/Carbon Fiber Cathodes for Wearable Electronics. *Advanced Energy Materials* **2016,** *6* (2).

34. Zhu, C.; Yang, P.; Chao, D.; Wang, X.; Zhang, X.; Chen, S.; Tay, B. K.; Huang, H.; Zhang, H.; Mai, W.; Fan, H. J., All Metal Nitrides Solid-State Asymmetric Supercapacitors. *Adv Mater* **2015,** *27* (31), 4566-71.

35. Senthilkumar, S. T.; Kim, J.; Wang, Y.; Huang, H.; Kim, Y., Flexible and wearable fiber shaped high voltage supercapacitors based on copper hexacyanoferrate and porous carbon coated carbon fiber electrodes. *Journal of Materials Chemistry A* **2016,** *4* (13), 4934-4940.

36. Cao, L.; Tang, G.; Mei, J.; Liu, H., Construct hierarchical electrode with Ni x Co 3-x S 4 nanosheet coated on NiCo 2 O 4 nanowire arrays grown on carbon fiber paper for high-performance asymmetric supercapacitors. *Journal of Power Sources* **2017,** *359*, 262-269.

37. Lu, K.; Zhang, J.; Wang, Y.; Ma, J.; Song, B.; Ma, H., Interfacial Deposition of Three-Dimensional Nickel Hydroxide Nanosheet-Graphene Aerogel on Ni Wire for Flexible Fiber Asymmetric Supercapacitors. *ACS Sustainable Chemistry & Engineering* **2016,** *5* (1), 821-827.

38. Pu, J.; Tong, Y.; Wang, S.; Sheng, E.; Wang, Z., Nickel–cobalt hydroxide nanosheets arrays on Ni foam for pseudocapacitor applications. *Journal of Power Sources* **2014,** *250*, 250-256.

39. Cheng, Y.; Zhang, H.; Varanasi, C. V.; Liu, J., Improving the performance of cobalt–nickel hydroxide-based self-supporting electrodes for supercapacitors using accumulative approaches. *Energy & Environmental Science* **2013,** *6* (11).

40. Zheng, X.; Gu, Z.; Hu, Q.; Geng, B.; Zhang, X., Ultrathin porous nickel–cobalt hydroxide nanosheets for high-performance supercapacitor electrodes. *RSC Advances* **2015,** *5* (22), 17007-17013.

41. Ma, H.; He, J.; Xiong, D. B.; Wu, J.; Li, Q.; Dravid, V.; Zhao, Y., Nickel Cobalt Hydroxide @Reduced Graphene Oxide Hybrid Nanolayers for High Performance Asymmetric Supercapacitors with Remarkable Cycling Stability. *ACS Appl Mater Interfaces* **2016,** *8* (3), 1992-2000.

Publication list

1. **Kyeong-Nam Kang**, Ik-Hee Kim, Ananthakumar Ramadoss, Sun-I Kim, Jong-Chul Yoon, and Ji-Hyun Jang*, "Ultrathin Nickel Hydroxide On Carbon Coated 3D-Porous Copper Structures for High Performance Supercapacitors", Physical Chemistry Chemical Physics, 2017,

2. Yo-Han Choi, Eun-Cheol Ra, Eun-Hyup Kim, Youn-Jeong Jang, **Kyeong-Nam Kang**, Sun-Hee Choi, Ji-Hyun Jang, and Jae-Sung Lee*, "Sodium-Containing Spinel Zinc Ferrite as a Catalyst Precursor for the Selective Synthesis of Liquid Hydrocarbon Fuels", ChemSusChem 2017, 10, 1-8

3. Ananthakumar Ramadoss, **Kyeong-Nam Kang**, Hyo-Jin Ahn, Sun-I Kim, Seung-Tak Ryu*, and Ji-Hyun Jang*, "Realization of High Performance Flexible Wire Supercapacitors Based on 3-Dimensional NiCo2O4/Ni Fibers", Journal of Materials Chemistry A, 2016, 4, 4718-4727

4. Sun-I Kim, **Kyeong-Nam Kang**, Sung-Wook Kim, and Ji-Hyun Jang*, "A One-step Practical Strategy to Enhance Overall Pseudocapacitor Performance", RSC Advances, 2014, 4, 59310-59314

* Note that following chapter is reproduced with permissions.

Chapter 2 is reproduced in part with permission of “Ultrathin nickel hydroxide on carbon coated 3D-porous copper structures for high performance supercapacitors”, Copyright @ 2017 The Royal Society of Chemistry